Nonlinear Aeroelastic Behavior of Tail / Rudder Systems with Freeplay and Actuator Failure

Matthew Noble

A thesis
submitted in partial fulfillment of the
requirements for the degree of

Master of Science in Aeronautics and Astronautics

University of Washington

2013

Committee:

Eli Livne, Chair

Keith Holsapple

Program Authorized to Offer Degree:
Aeronautics & Astronautics

University of Washington

Abstract

Nonlinear Aeroelastic Behavior of Tail / Rudder Systems with Freeplay and Actuator Failure

Matthew Noble

Chair of the Supervisory Committee:
Professor Eli Livne
UW Aeronautics & Astronautics

This thesis discusses the development of numerical simulations implemented in MATLAB and of an experimental tail/rudder model for the investigation of the effects of non-linearities on control surface flutter of a three-degree of freedom typical section airfoil. Non-linearities investigated include a structural non-linearity in the form of freeplay about the control surface hingeline as well as velocity-squared damping, simulating a failed actuator. The mathematical modeling, design, and testing of a prototype velocity-squared damper is also presented for use in the numerical simulations. In both cases, the describing function method has been used to predict the amplitudes of possible Limit-Cycle Oscillations (LCOs) in the rudder DOF. Response amplitudes and frequencies in the frequency domain, are shown to agree extremely well with results obtained in the time-domain via direct numerical integration of the equations of motion. Both stable and unstable limit-cycle behavior has been predicted, resulting in a detailed set of predictions for the response of the system below the flutter boundary.

TABLE OF CONTENTS

LIST OF FIGURES

LIST OF TABLES

ACKNOWLEDGMENTS

I would like to thank several people who made this thesis a reality. First, I wish to thank my advisor, Professor Eli Livne, who has taught me everything I know about aeroelasticity and for his belief in my abilities to complete this undertaking. His mentoring and extensive knowledge of the subject matter was invaluable. I would also like to thank him for his tireless efforts to fund my efforts via Research and Teaching Assistantships, without this support, completing this work would have certainly seemed impossible.

I would like to thank Research Engineer, William Kuykendall (Mechanical Engineering), for his assistance in the design and improvement of the experimental hardware. This work would not have been possible without his efforts and ingenuity, especially as deadlines fast approached.

I would like to thank my parents, Michael and Bonnie Noble, for raising me to believe that I could accomplish anything I put my mind to. Thank you for all your love, support, and guidance.

DEDICATION

To Madelin (and Freddy): I love you so much and it would be impossible to express how much of a help you have been – this thesis is dedicated to you.

Chapter 1
INTRODUCTION

1.1 Background

Aeroelasticity studies the often complex interactions between inertial, elastic, and aerodynamic forces on a system. Due to the potential for catastrophic failure of the system under certain aeroelastic conditions, aeroelastic behavior due to all possible variation of structural characteristics must be considered in the design of modern aircraft. The underlying causes and consequences of these variations must therefore be thoroughly examined and accurate numerical modeling needs to be available throughout the development - certification - operation chain of an aircraft.

This work is part of a larger research effort seeking to develop the simulation tools and experimental capabilities for such analysis at the University of Washington. To that end, the following research pursues the capabilities for simulation of aeroelastic systems with control surface freeplay and other hinge nonlinearities as well as the development of aeroelastic wind tunnel testing capabilities.

The past couple of decades have seen a substantial amount of research into this area. In particular, a significant amount of research on hinge stiffness freeplay has been performed by the aeroelasticity research group at Duke University. A number of studies have detailed the development of numerical simulations supported by wind tunnel tests in the Duke University low speed wind tunnel and investigated limit cycle oscillations (LCO)[4][18][22][10] and active control of aeroelastic systems[24][3] in the presence of a freeplay nonlinearity. These studies, based on the typical aeroelastic section seen in Figure 1.1, illustrate the complex behavior of an aeroelastic system when nonlinearities are present. Limit-cycles were found to occur at speeds well below

the linear flutter velocity and can have significant effects on the characteristics and performance of the aircraft.

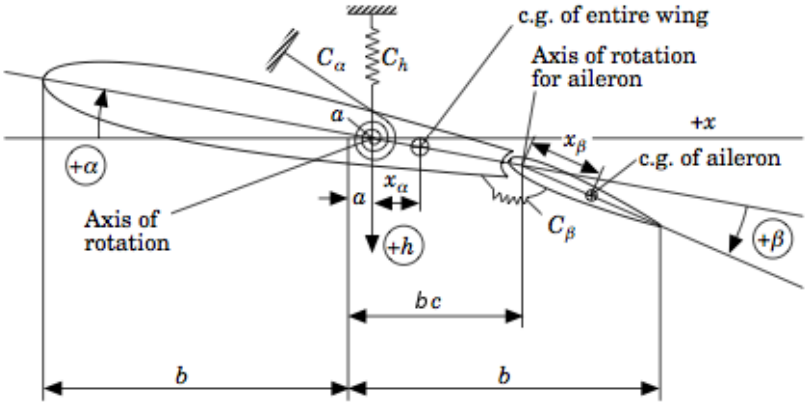

Figure 1.1: Schematic of the Aeroelastic Model[4].

More recently, work at Boeing by *Gordon et al.* has pursued the development of commercial simulation tools for aircraft with stiffness freeplay[7] and a velocity-squared damping hinge nonlinearity in the case of actuator failure[6]. The velocity-squared damping case is of considerable interest to aircraft designers. Actuator failure may cause a loss of hinge stiffness and the actuator would function as a nonlinear damper to dissipate energy and limit the oscillation amplitude about the control surface hinge line. As rotation rates increase due to loss of hinge stiffness, the effect of the dampers can result in LCO. The work done by Gordon[6] at Boeing, included just numerical simulations of the aeroelastic section subjected to a quadratic damping (no hinge stiffness) nonlinearity. Gordon was able to correlate describing function results (for both freeplay and damping nonlinearities) with direct time-integration predictions.

Work done at Duke[18] and Boeing[7][6] illustrate the advantages of analyzing the LCO behavior of nonlinear aeroelastic systems using the describing function (or harmonic balance) approach. The studies at Duke University applied both direct

time integration and describing function methods to analyze limit cycle behavior, of an aeroelastic section with control surface freeplay, and were able to verify theoretical responses with experimental data.

Compared to direct time integration, the computational time and effort is greatly reduced via the describing function technique. Another advantage is that direct numerical integration of the equations of motion cannot assess the stability of predicted limit cycles or find it difficult to determine the existence of multiple limit cycles of differing amplitudes at the same flow speed. However, direct time integration is able to predict non-LCO responses in the system (convergent, divergent, non-periodic), that the describing function is not able to capture, so aeroelastic simulation tools should include both capabilities.

1.2 Objectives

There are two structural hinge nonlinearities of interest in this research: control surface freeplay - a nonlinearity in stiffness, and quadratic (velocity-squared) damping - a nonlinearity in damping. The freeplay nonlinearity is represented via a piecewise linear restoring force about the control surface hinge line, depicted in Figure 1.2. As will be discussed later, it is important to capture the transition points between each linear region during the numerical analysis.

The hinge rotation dampers, in the case of actuator failure, provide damping forces which are proportional to the square of the control surface rotation rate.

The goals of this research are to:

- Characterize system properties of a University of Washington experimental model of the 3 D.O.F aeroelastic section.

- Complete the development and validation of experimental velocity-squared dampers for that model.

- Develop numerical simulation models for a fundamental 3 D.O.F aeroelastic section in a 2-D unsteady, incompressible flow-field capable of incorporating various hinge nonlinearities.

- Validate linear and freeplay numerical models and simulation codes with data from Duke system [4][7][18].

- Use the simulation codes to study the aeroelastic behavior of the University of Washington's tail/rudder model.

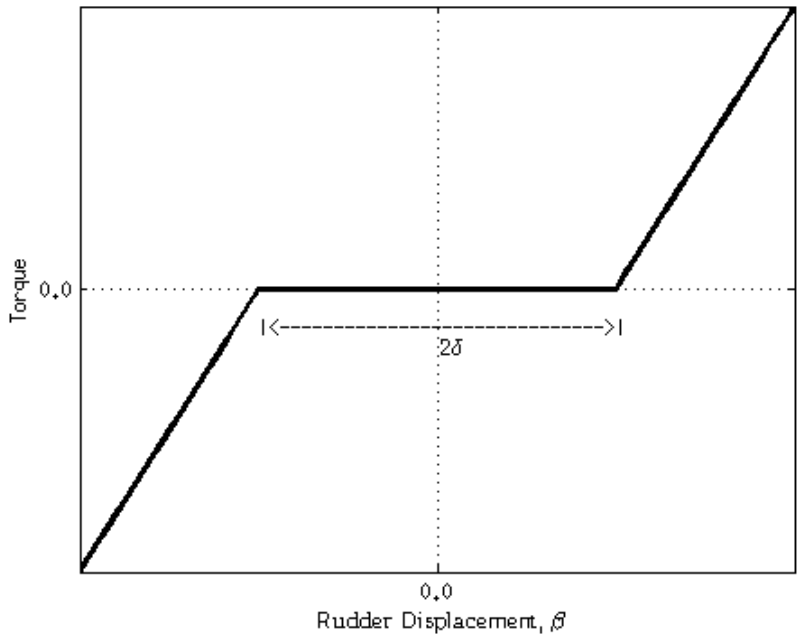

Figure 1.2: Structural restoring moment due to K_β with a symmetric freeplay region about $\beta = 0$.

1.3 Report Structure

A brief derivation of the equations of motion of the aeroelastic section, including inertial, stiffness, structural damping, and aerodynamic contributions is presented in Chapter 2.

The physical model, including its design and structural characterization is discussed in Chapter 3.

A discussion of the derivation of the mathematical model of a velocity-squared damper and the design and testing of a prototype damper that can be attached to the experimental tail/rudder model for wind tunnel tests is presented in Chapter 4.

The description of the theoretical model in the frequency domain, including the Describing Function method for analyzing nonlinearities, is presented in Chapter 5.

The state-space theoretical model in the time domain is discussed in Chapter 6. This chapter also discusses the algorithm implemented for accurate integration of the piecewise linear system of the freeplay case.

Chapter 7 compares predictions obtained using the numerical tools developed in Chapters 5 and 6 for the case of the Duke system to published results. This serves to validate the methods and computer codes developed for the present work.

Numerical simulations for linear, freeplay, and quadratic damping scenarios of the University of Washington model, in both the frequency and time domain, are presented in Chapter 8.

Conclusions based on the numerical and experimental results as well as directions for future research are presented in Chapter 9.

Appendix A is a list of symbols commonly used throughout the test and Appendix B lists the Theodorsen constants used in the development of the aerodynamic forces and moments.

Chapter 2

THE EQUATIONS OF MOTION OF THE AEROELASTIC SECTION

Before developing the numerical simulation tools for analyzing the responses of the aeroelastic section presented in Figure 1.1, it is necessary to have an understanding of the differential equations of motion of the system and the contributions to those equations. In this chapter the form of the structural contributions is derived using Lagrangian mechanics, aerodynamic forces and moments are determined from Theodorsen's method[20], and a hysteretic structural damping model is presented as an alternative to the typical viscous model.

The efficient application of Lagrange's equations can be facilitated by representing the inertial quantities in convenient coordinate systems and selecting an appropriate set of generalized coordinates. The system in Figure 1.1 is idealized as a combination of two rigid bodies: the tail and the rudder. The relevant quantities for the tail and rudder are displayed in the figure and the generalized coordinates are denoted by the symbols h, α, and β. The generalized coordinates are chosen to coincide with the three degrees of freedom (DOF) of the system: plunge displacement, pitch angle, and rudder angle relative to the main tail. The origin of the h and α coordinates are located at the shear center location of the tail/rudder system. The h coordinate is fixed to the tail and moves with it measuring pure plunging motion; the α coordinate is fixed in inertial space and oriented relative to oncoming wind, i.e. the angle of attack. The third generalized coordinate, β, is fixed to the rudder and rotated relative to the body-fixed system about the rudder hinge line; the origin is also located along the hinge line.

2.1 Structural Contributions

2.1.1 Kinetic and Potential Energy

The selection of the generalized coordinates above allows for the simple derivation of kinetic and potential energies of the system. The total kinetic energy of the system is the sum of the kinetic energy of the tail and the rudder control surface.

Using the quantities defined in Figure 1.1, the kinetic energy of the tail is found from integrating the kinetic energy at points along the tail from $x = 0$ to $x = b + bc$; the kinetic energy of the rudder is determined by integrating the kinetic energy at points along the rudder surface from $x = b + bc$ to $x = 2b$. Summing the kinetic energy contributions, the total kinetic energy of the system can be written as

$$T = \frac{1}{2}\left\{\dot{h} \quad \dot{\alpha} \quad \dot{\beta}\right\}\begin{bmatrix} M & S_\alpha & S_\beta \\ & I_\alpha & (I_\beta + b(c-a)S_\beta \\ \text{sym} & & I_\beta \end{bmatrix}\begin{Bmatrix} \dot{h} \\ \dot{\alpha} \\ \dot{\beta} \end{Bmatrix} \tag{2.1}$$

where the entries of the $3x3$ mass matrix are defined in Appendix A.

The potential energy of a system typically consists of two contributions: the strain energy and the gravitational potential energy. The numerical analyses of this system assume a vertical positioning of the tail/rudder model within the flow-field eliminating the need to consider gravitational effects. The strain energy is the work done in going from the reference position to a deformed position and is therefore represented by the energy stored in the springs represented in Figure 1.1:

$$U = \frac{1}{2}K_h h^2 + \frac{1}{2}K_\alpha \alpha^2 + \frac{1}{2}K_\beta \beta^2 \tag{2.2}$$

Note that the symbol for stiffness K is chosen instead of the C depicted in Figure 1.1; the symbol c is reserved for the hinge line location and the viscous damping symbol coefficient and should be understood from context.

Lagrange's equations can be expressed in the following form

$$\frac{d}{dt}\left(\frac{\partial T}{\partial \dot{q}_i}\right) - \frac{\partial T}{\partial q_i} + \frac{\partial U}{\partial q_i} = Q_{q_i} \tag{2.3}$$

where q_i is the i^{th} generalized coordinate and Q_{q_i} is the generalized force associated with q_i and includes external and nonconservative forces. Substituting equations 2.1 and 2.2 into 2.3, the following system of equations is obtained:

$$\begin{bmatrix} M & S_\alpha & S_\beta \\ & I_\alpha & (I_\beta + b(c-a)S_\beta \\ \text{sym} & & I_\beta \end{bmatrix} \begin{Bmatrix} \ddot{h} \\ \ddot{\alpha} \\ \ddot{\beta} \end{Bmatrix} + \begin{bmatrix} K_h & 0 & 0 \\ 0 & K_\alpha & 0 \\ 0 & 0 & K_\beta \end{bmatrix} \begin{Bmatrix} h \\ \alpha \\ \beta \end{Bmatrix} = \begin{Bmatrix} Q_h \\ Q_\alpha \\ Q_\beta \end{Bmatrix} \tag{2.4}$$

The matrices in equation 2.4 represent structural inertia terms of the system and structural stiffness terms, respectively, and can be simply identified by the symbols $\mathbf{M_s}$ and $\mathbf{K_s}$.

2.1.2 Structural Damping

In one of his later papers on the flutter problem, Theodorsen et al[21] determine the need to include some amount of structural damping in flutter calculations. The internal structural damping has been shown to cause significant changes in the flutter velocity and even a consideration of a small amount of structural damping can bring the calculated flutter speed from zero to an experimentally expected value.

Structural damping is often characterized as a viscous force proportional to the velocity. However, it is also possible to express the structural damping in terms of a hysteretic model that is a function of the amplitude of an elastic system but not of its frequency.

Hysteretic Damping

The hysteretic damping is proportional to amplitude but in phase with the velocity of motion and is based on the energy loss per cycle of oscillation due to steady-state harmonic loading. For lightly damped structures, relating viscous to structural damping coefficients results in an equivalence between the structural damping coefficient and the damping ratio ζ:

$$g_{h,\alpha,\beta} = 2\zeta_{h,\alpha,\beta} \tag{2.5}$$

leading to a hysteretic damping matrix, $\mathbf{H}$ (valid only for simple harmonic motion) of the form

$$\mathbf{H} = j\mathbf{G_{st}}\mathbf{K_s} \tag{2.6}$$

where

$$\mathbf{G_{st}} = \begin{bmatrix} g_h & 0 & 0 \\ 0 & g_\alpha & 0 \\ 0 & 0 & g_\beta \end{bmatrix}$$

Viscous Damping

A one-term viscous damping model can also be used to characterize the structural damping forces:

$$\mathbf{C} = \begin{bmatrix} 2m_{hh}\zeta_h\omega_h & 0 & 0 \\ 0 & 2m_{\alpha\alpha}\zeta_\alpha\omega_\alpha & 0 \\ 0 & 0 & 2m_{\beta\beta}\zeta_\beta\omega_\beta \end{bmatrix} \tag{2.7}$$

where ζ is the measured damping ratio, ω is the uncoupled natural frequency, and m_{jj} $(j = h, \alpha, \beta)$ is the structural mass for each degree of freedom.

2.2 Generalized Forces

The principle of virtual work can now be applied to obtain expressions for the generalized forces, including nonconservative damping forces. The generalized forces can be determined from the following equation

$$Q_{q_i} = \frac{\partial \delta W}{\partial \delta q_i} \tag{2.8}$$

Assuming a viscous damping model first, the nonconservative damping contribution to the generalized force Q_{q_i} is

$$\begin{Bmatrix} Q_h \\ Q_\alpha \\ Q_\beta \end{Bmatrix} = - \begin{bmatrix} c_h & 0 & 0 \\ 0 & c_\alpha & 0 \\ 0 & 0 & c_\beta \end{bmatrix} \begin{Bmatrix} \dot{h} \\ \dot{\alpha} \\ \dot{\beta} \end{Bmatrix} \tag{2.9}$$

where $c = 2m\zeta\omega$.

Next, the externally applied forces due to the aerodynamics of the system need to be added to the generalized force vector. The generalized aerodynamic forces are due to P - the opposite of the lifting force, M_α - the pitching moment about the shear center of the tail, and H_β - the rudder moment about its hinge line. Including the aerodynamic forces in equation 2.9 results in a complete expression for the generalized forces

$$\begin{Bmatrix} Q_h \\ Q_\alpha \\ Q_\beta \end{Bmatrix} = - \begin{bmatrix} c_h & 0 & 0 \\ 0 & c_\alpha & 0 \\ 0 & 0 & c_\beta \end{bmatrix} \begin{Bmatrix} \dot{h} \\ \dot{\alpha} \\ \dot{\beta} \end{Bmatrix} + \begin{Bmatrix} P \\ M_\alpha \\ H_\beta \end{Bmatrix} \tag{2.10}$$

and it is now possible to use Theodorsen's method[20] to express the vector of aerodynamic forces and moments in a meaningful way.

2.2.1 Aerodynamic Contributions

Theodorsen's method for for calculating the aerodynamic forces on thin oscillating airfoils is derived from two-dimensional potential flow. He was able to make this simplification by regarding the "flutter problem on a wing of infinite aspect ratio, moving with small oscillatory amplitudes at constant velocity through an incompressible, non-viscous fluid[16]." Theodorsen split his solution into two parts: a non-circulatory flow that satifies the boundary conditions at the airfoil surface and a circulatory flow that enforces the Kutta condition at the trailing edge of the flap. The elementary flows are combined to develop the flow due to the disturbance of the airfoil, flow due to circulation on the airfoil, and flow due to vortices in the wake.

The specifics of Theodorsen's derivation are extremely detailed and well known, and will not be covered in this thesis. The reader is directed to *Theodorsen*[20], *Scanlan et al.*[16], or *Bisplinghoff et al.*[2] for a thorough review of the mathematical derivation of the aerodynamic forces. Theodorsen expresses the aerodynamic forces on the aeroelastic section as functions of the motion and geometry of the system:

$$\begin{aligned} P = &- \rho b^2 (U\pi\dot{\alpha} + \pi\ddot{h} - \pi ba\ddot{\alpha} - UT_4\dot{\beta} - T_1 b\ddot{\beta}) \\ &- 2\pi\rho UbC(k)\left\{U\alpha + \dot{h} + b\left(\frac{1}{2} - a\right)\dot{\alpha} + \frac{1}{\pi}T_{10}U\beta \right. \\ &\left. + b\frac{1}{2\pi}T_{11}\dot{\beta}\right\} \end{aligned} \tag{2.11}$$

$$
\begin{aligned}
M_\alpha = &-\rho b^2\Bigg\{\pi\left(\frac{1}{2}-a\right)Ub\dot{\alpha}+\pi b^2\left(\frac{1}{8}+a^2\right)\ddot{\alpha}\\
&+(T_4+T_{10})U^2\beta\\
&+\left(T_1-T_8-(c-a)T_4+\frac{1}{2}T_{11}\right)Ub\dot{\beta}\\
&-\left(T_7+(c-a)T_1\right)b^2\ddot{\beta}-a\pi b\ddot{h}\Bigg\}\\
&+2\rho Ub^2\pi\left(a+\frac{1}{2}\right)C(k)\Bigg\{U\alpha+\dot{h}+b\left(\frac{1}{2}-a\right)\dot{\alpha}\\
&+\frac{1}{\pi}T_{10}U\beta+b\frac{1}{2\pi}T_{11}\dot{\beta}\Bigg\}
\end{aligned}
\tag{2.12}
$$

$$
\begin{aligned}
H_\beta = &-\rho b^2\Bigg[\Bigg\{-2T_9-T_1+T_4\left(a-\frac{1}{2}\right)\Bigg\}Ub\dot{\alpha}+2T_{13}b^2\ddot{\alpha}\\
&+\frac{1}{\pi}U^2\beta(T_5-T_4T_{10})-\frac{1}{2\pi}Ub\dot{\beta}T_4T_{11}-\frac{1}{\pi}T_3b^2\ddot{\beta}\\
&-T_1b\ddot{h}\Bigg]-\rho Ub^2T_{12}C(k)\Bigg\{U\alpha+\dot{h}+b\left(\frac{1}{2}-a\right)\dot{\alpha}\\
&+\frac{1}{\pi}T_{10}U\beta+b\frac{1}{2\pi}T_{11}\dot{\beta}\Bigg\}
\end{aligned}
\tag{2.13}
$$

Equations 2.11 - 2.13 illustrate the complicated dependence of the aerodynamic forces and moments on the motion and configuration of the system. In the above equations, T_i, $i = 1, 2, ..., 14$, are the Theodorsen constants (or T-functions) which are determined from the geometry of the section, namely the location of the elastic axis and the hinge line. The above expressions are also dependent upon the Theodorsen Circulation Function, C(k), defined as follows:

$$
C(k)=\frac{\int_1^\infty \frac{x_0}{\sqrt{x_0^2-1}}e^{-ikx_0}dx_0}{\int_1^\infty \frac{x_0}{\sqrt{x_0^2-1}}e^{-ikx_0}dx_0+\int_1^\infty \frac{1}{\sqrt{x_0^2-1}}e^{-ikx_0}dx_0}
\tag{2.14}
$$

$C(k)$ is a function of the non-dimensional reduced frequency of oscillation, $k = \frac{\omega b}{U}$

(where b is the half-chord) and, by separating $C(k)$ into its real and imaginary parts, can be expressed in terms of Bessel functions of the first and second kind.

Since the forces for the aerodynamic forces and moments are restricted to simple harmonic motion, the derivatives of each state variable can be expressed in terms of the complex amplitude of the state variable itself such that equations 2.11 - 2.13 can be re-written as

$$\begin{Bmatrix} P \\ M_\alpha \\ H_\beta \end{Bmatrix} = \frac{1}{2}\rho_\infty U_\infty^2 \left[A(jk)\right] \begin{Bmatrix} h \\ \alpha \\ \beta \end{Bmatrix} \tag{2.15}$$

Now the equations of motion of the aeroelastic system are fully determined:

$$\mathbf{M_s}\ddot{\mathbf{q}} + \mathbf{K_s}\mathbf{q} = \frac{1}{2}\rho_\infty U_\infty^2 \mathbf{A(jk)}\mathbf{q} \tag{2.16}$$

where $\mathbf{q} = \{h, \alpha, \beta\}^T$ and structural damping can be included either via the viscous model ($\mathbf{C}\dot{\mathbf{q}}$) or the hysteretic model ($j\mathbf{G_{st}}\mathbf{K_s}\mathbf{q}$).

Chapter 3
EXPERIMENTAL MODEL

The aeroelasticity research group at Duke University, designed and built an experimental model of the aeroelastic section for use in the Duke University low speed wind tunnel[4]. A physical model, built to replicate that design has been designed and built at the University of Washington for flutter tests in the University of Washington's 3'x3' low speed wind tunnel; the model was designed and built by Francesca Paltera for her M.S.M.E. work at the University of Washington[14][11]. The University of Washington's model, inspired by the Duke University model, is designed to simulate the 3 D.O.F. aeroelastic section of Figure 1.1 in 2-D, incompressible flow. The experimental model, mounted to a rigid support for ground testing, is shown in Figure 3.1. This chapter outlines the design of the experimental model and the evaluation of the system parameters for input into the numerical simulations.

3.1 Design of the Model

The 2-D model uses a NACA 0012 airfoil for its profile and was built in two main sections: (1) a main tail body with a 0.381 m chord and 0.9017 m span; and a rudder section with a 0.127 m chord and a 0.9017 m span. The tail section is made of aluminum and has a circular spar beam that serves as the pitch axis of rotation; the beam is located at the quarter chord location from the leading edge of the tail. Ballast masses allow for variation of the tail's inertial properties. The rudder is attached to the tail along a hinge line and is made of carbon fiber composite material and has a similar circular spar beam.

The tail / rudder model is designed to be mounted vertically in the wind tunnel

Figure 3.1: The tail/rudder model mounted in the lab for ground testing.

using a support structure that allows both plunging and pitching motion; the rudder is allowed to have a rotational degree of freedom, relative to the main wing, about

its hinge line. The support structure is made of a pair of bi-cantilever beams made of steel leaf springs 29.85 x 7.62 x 0.158 cm. The free-ends of the leaf springs are joined by an aluminum support block and are allowed to move in the plunge degree of freedom; this support structure is designed to be mounted on the outside of the wind tunnel during a test as seen in Figure 3.2. The tail spar beam mounts into the upper and lower support blocks using a pair of bearings; a pair of steel wires are secured into the pitch D.O.F. spar beam at the top support block to act as the pitch springs (see Figure 3.3). A steel leaf spring is tightly secured in a slot at the top of the hinge line spar. The free end of the leaf spring is positioned between two support screws on the tail as seen in seen in Figure 3.3; the screws can be positioned securely to the leaf spring (no freeplay) or loosened to allow the free-end of the rudder leaf spring to move through a certain range before feeling resistance, and thereby introducing hinge freeplay into the model.

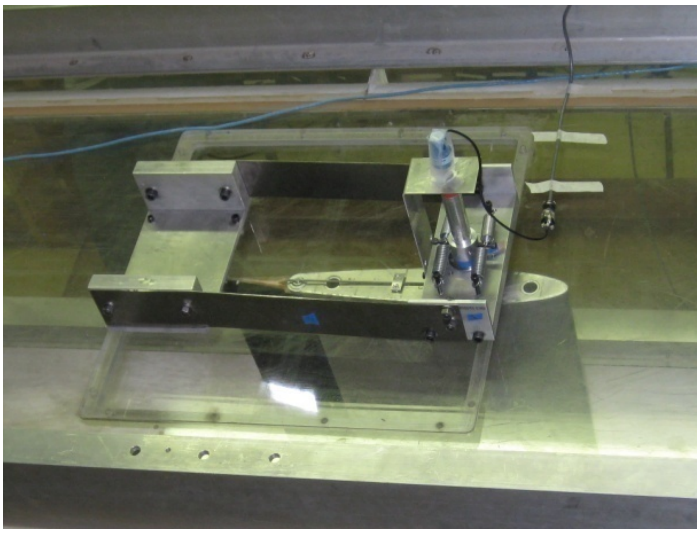

Figure 3.2: The tail/rudder model mounted in the wind tunnel with support blocks and structure mounted on the outside of the test section(Francesca Paltera, unpublished).

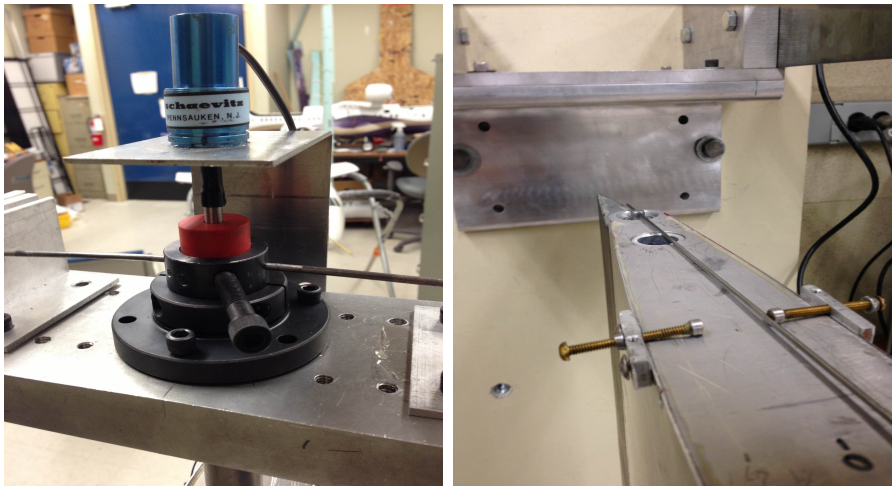

(a) Pitch D.O.F. springs and RVDT sensor

(b) Rudder D.O.F. leaf spring and freeplay support screws

Figure 3.3: Pitch and Flap DOF leaf spring set-ups and freeplay support mechanism in flap DOF

3.2 Measurement Sensors

The pitch and flap rotational motion are measured using rotational variable displacement transducers (RVDT). The pitch RVDT sensor is mounted at the top of the pitch axis and has a sensitivity of 125 $\frac{mV}{degree}$ and a range of 56.56°. The flap RVDT is mounted on the rudder, inside of the main tail section, and has a sensitivity of 29 $\frac{mV}{degree}$ and a range of 121.91°. The plunge motion is measured using a Polytec Laser Vibrometer that is able to record both velocity and displacement of the tail in plunge; the respective sensitivities are 8000 $\frac{mV}{\frac{m}{sec}}$ and 100 $\frac{mV}{mm}$. The respective ranges of the laser vibrometer, in velocity and displacement, are 1.25 $\frac{m}{sec}$ and 200 mm.

The voltages from these sensors is output to a Jaguar Spectral Dynamics system connected to a PC running SUSE Linux (10.0). The data is recorded and can then be displayed graphically.

3.3 Model Properties

Ground tests were performed while the model was mounted in the lab to determine the natural frequencies, stiffness, and damping characteristics of the system. One degree of freedom at a time was allowed to remain free in the structure, while the other two degrees-of-freedom were fixed and motion constrained. Force gauges were used to displace the structure, and as it was released, the time history was recorded by the Jaguar system. Time history plots for each degree of freedom, and the log decrement method was used to determine the damping ratios for the system.

The logarithmic decrement δ_{ld} is the natural logarithmic value of the ratio of two adjacent peak values of displacement in free decay vibration:

$$\delta_{ld} = \frac{1}{n} \ln \frac{x(t)}{x(t+nT)}$$

where T is the period and n is any integer of successive, positive peaks. It is used to find the damping ratio of an under-damped system in the time domain via:

$$\zeta = \frac{1}{\sqrt{1 + (\frac{2\pi}{\delta_{ld}})^2}}$$

The mass and CG location of each component of the system were measured and compared to the Unigraphics CAD model. The CAD model was then used to calculate the moments of inertia of the tail / rudder system and the rudder by itself and compared to moments of inertia determined from the uncoupled natural frequencies and measured spring values. The listing of nominal system parameters used for the linear and freeplay analysis is presented in Table 3.1.

Table 3.1: Nominal System Parameters of the Experimental Model

Geometry	
Half-chord, b	0.26 m
Span	0.915 m
Elastic axis, a, normalized by b	-0.454
Hinge line, c, normalized by b	0.527
Mass	
Mass of Tail	5.919 kg
Mass of Rudder	0.658 kg
Mass of Support Blocks	4.793 kg
Mass of Pitch RVDT Sensor	0.0692 kg
Mass of Pitch Springs	0.1155 kg
Inertia	
S_α	0.1384 $kg-m$
S_β	0.0434 $kg-m$
x_α	0.0809
x_β	0.0254
I_α	0.1362 $kg-m^2$
I_β	0.0019 $kg-m^2$
Stiffness	
K_h	4700 $\frac{N}{m}$
K_α	139 $\frac{N-m}{rad}$
K_β	4.3 $\frac{N-m}{rad}$
Damping	
ζ_h	0.0032
ζ_α	0.148
ζ_β	0.062

Chapter 4
THE VELOCITY SQUARED DAMPER

The quadratic damping (no hinge stiffness) case is of particular interest to aircraft designers as discussed earlier; because of this, it is very important to develop robust numerical simulation tools to study the nonlinear behavior of this system. A search for small commercial off-the-shelf dampers that would exhibit velocity squared behavior was unsuccessful, therefore a prototype damper was designed and built to exhibit the quadratic damping behavior of a failed actuator. The characteristics of the damper discussed in this chapter will be used in the numerical simulations presented in this thesis, and the damper itself will be used for future wind tunnel tests of the system. This chapter outlines the mathematical model governing the damper, the effect of the dampers on the structural dynamics of the system, and the tests to characterize the damping behavior.

4.1 Mathematical Model

The velocity squared behavior of the damper relies on hydraulic orifices allowing oil to flow, through the piston head, between the two champers of the damper cylinder. The acceleration of the fluid through the orifices in the piston head, leads to pressure differences, and therefore forces, that are proportional to the square of the piston head's relative velocity. The principle of the simple hydraulic actuator was based on the survey work done by *Bauchau et al.* on rotorcraft components[1], *Hou et al.*[9], and *Viersma*[23]; the schematic of the damper design is presented in Figure 4.1.

The derivation of the mathematical model requires a few assumptions: the speed of the piston is not too high, the fluid is incompressible, the orifice size is not too

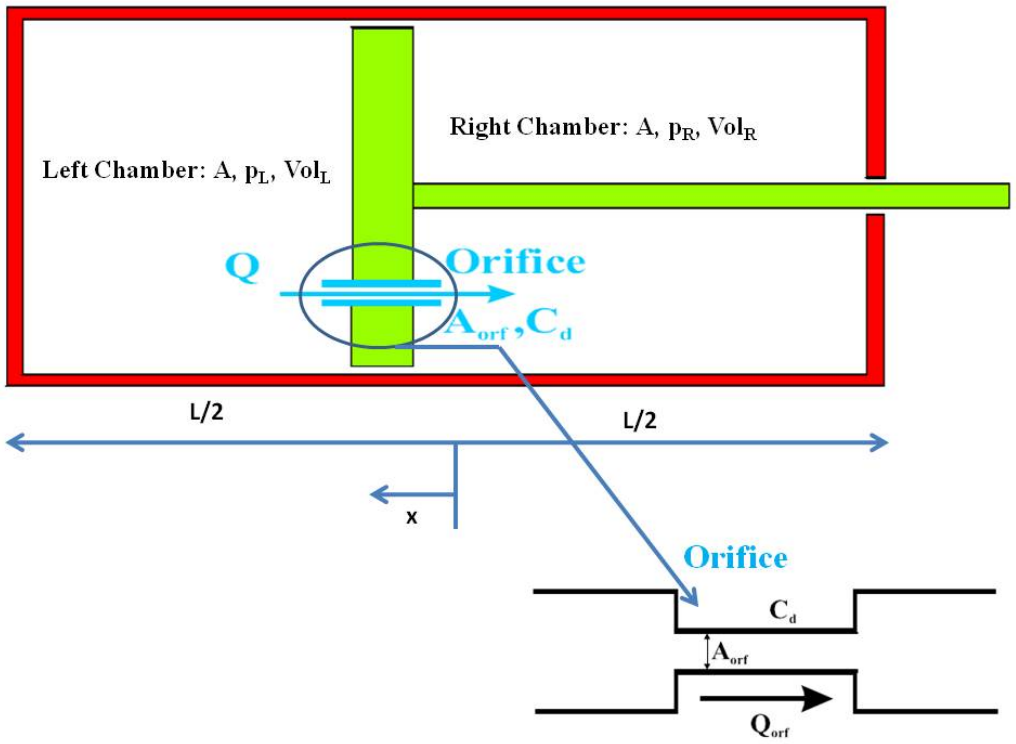

Figure 4.1: Basic Schematic of Velocity-Squared Damper[1].

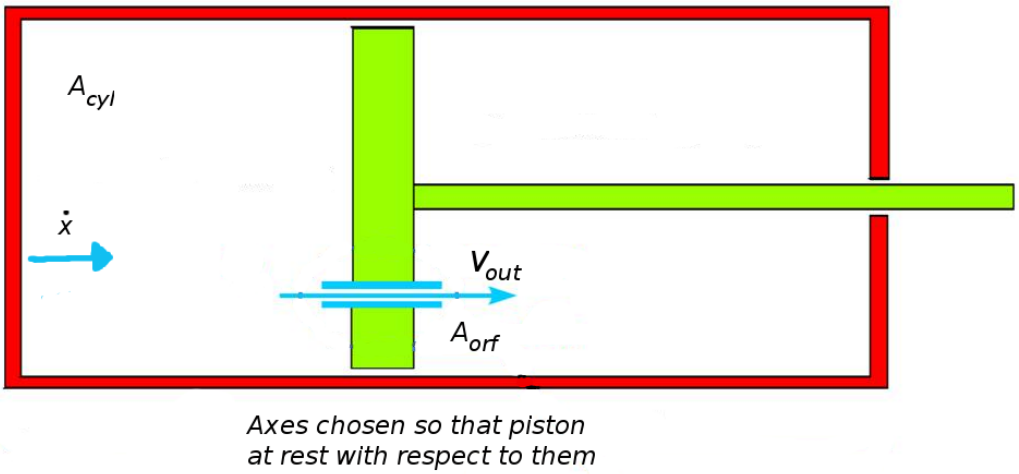

Figure 4.2: Relative Velocity Relations of Quadratic Damper[1].

small, the length of the cylinder L is much greater than the amplitude of piston motion, and orifices are designed so pressure is as uniform as possible on each side of the piston head.

The damper system is considered in a reference frame moving with the piston, as in Figure 4.2, where the piston head is moving to the left with velocity $v_p = \dot{x}$. The flow on the wall at the far left is then moving towards the piston with a velocity $\dot{x}$ and has a pressure p_L. Fluid flowing through the orifice into the right chamber is accelerated to velocity V_{out} and the pressure in the right chamber is defined as p_R. The speed of oil flowing out of the narrow orifice is determined by[23]:

$$V_{out} = C_d\sqrt{\frac{2\Delta p}{\rho}} \tag{4.1}$$

$$\Delta p = \frac{1}{2}\rho V_{out}^2 \frac{1}{C_d^2} \tag{4.2}$$

where C_d is the discharge coefficient of the orifice. For fully turbulent flow conditions, the theoretical C_d is 0.611[23], however, the discharge coefficient can be lower than the theoretical value depending on Reynold's number (Re) and orifice shape. Conservation laws require that the volume change per unit time due to the piston head moving to the left, equal the fluid volume flowing into the right chamber through the orifice, therefore:

$$A_p v_p = A_o V_{out} \tag{4.3}$$

$$V_{out} = \left(\frac{A_p}{A_o}\right) v_p = \frac{1}{\eta} v_p \tag{4.4}$$

where A_o is the cross-sectional area of the orifice, A_p is the cross-sectional area of the piston head, and η is defined as the ratio of orifice to piston head cross-sectional

areas. The expression for V_{out} can then be substituted into the Δp equation above resulting in:

$$\Delta p = 0.5\rho\frac{1}{C_d^2}\frac{1}{\eta^2}v_p^2 \tag{4.5}$$

and the force due to pressure differences on the piston head is determined by

$$F_{pressure} = A\Delta p = (A_p - A_o)\Delta p = (1-\eta)A_p\Delta p \tag{4.6}$$

$$F_{pressure} = \frac{1}{2}\rho\frac{1}{C_d^2}\frac{(1-\eta)}{\eta^2}A_p v_p^2 \tag{4.7}$$

The shear stress on the outside of the piston head, between the piston and the cylinder wall, are modeled as viscous effects and the force due to viscosity is given by:

$$F_{viscosity} = \pi D_p t\tau \tag{4.8}$$

where $\pi D_p t$ is the surface area of the circumference of the piston and

$$\tau = \mu\frac{\partial v}{\partial y} = \mu\frac{v_p}{d} \tag{4.9}$$

and μ is the viscosity of the fluid in the cylinder and d is the distance between the cylinder wall and the piston head circumference, then

$$F_{viscosity} = \pi D_p t\mu\frac{v_p}{d} \tag{4.10}$$

where D_p is the diameter of the piston head, t is the thickness of the piston head.

Finally, forces due to the piston and rod inertia must be considered as well

$$F_{inertial} = (2\pi f)^2\mathcal{A}m_{piston/rod} \tag{4.11}$$

where f is the frequency of oscillation in Hz, $\mathcal{A}$ is the amplitude of oscillation, and $m_{piston/rod}$ is the mass of the piston and rod.

The total force is then given by

$$F_{TOT} = F_{pressure} + F_{viscosity} + F_{inertial} \tag{4.12}$$

The $F_{inertial}$ term is accounted for as a contribution to the inertial matrix of the system. It has to be accounted for, however, when the damper is tested separately. The contributions of the dampers to the systems inertial matrix are discussed in the following section.

4.2 Damper Contributions to Inertial Matrix of the Equations of Motion

The motivation of this section is to characterize the effect of a velocity squared damper connected to the aeroelastic model. To determine the mass matrix contribution of the dampers to the mass matrix of the aeroelastic system, the equations of motion of the damper in terms of the system's D.O.F. $\{h, \alpha, \beta\}^T$ need to be derived. A schematic of the aeroelastic system with a damper attached is presented in Figure 4.3.

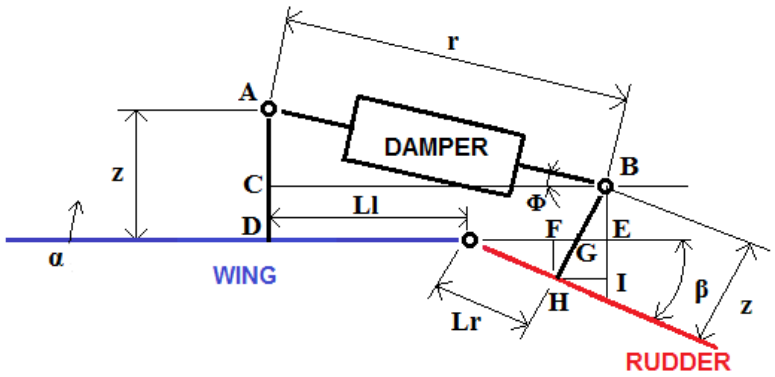

Figure 4.3: Schematic of the aeroelastic system with a damper attached.

The geometry of the system in Figure 4.3 leads to the following relations:

$$r^2 = (z - [z - L_r \tan\beta]\cos\beta)^2 + (L_l + L_r \cos\beta + z \sin\beta)^2 \tag{4.13}$$

$$\tan\phi = \frac{z - z\cos\beta + L_r \sin\beta}{L_l + L_r \cos\beta + z \sin\beta} \tag{4.14}$$

Assuming small angles, $\Delta\phi$ and $\Delta\beta$, about $\beta = 0$ then,

$$\left.\frac{\Delta\phi}{\Delta\beta}\right|_{\beta=0} = \left.\frac{\delta\phi}{\delta\beta}\right|_{\beta=0} = \frac{L_r}{L_l + L_r} \tag{4.15}$$

Then, the total angular motion of the cylinder is the sum of the wing rotation α and the angle $\phi(\beta)$ associated with the rudder surface:

$$\alpha + \phi(\beta) = \alpha + \frac{L_r}{L_l + L_r}\beta \tag{4.16}$$

Next, the linear motion of the center of gravity of the damper needs to be considered. A diagram of this motion is presented in Figure 4.4; only the cylinder and fluid contributions are considered here, the effect of the piston and rod are studied separately. For small angles, the total linear motion in the vertical translation DOF

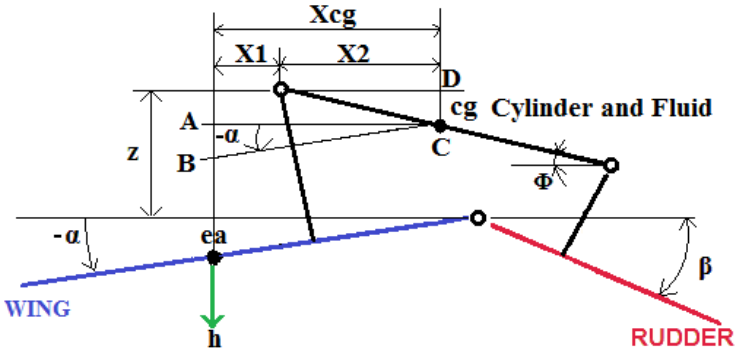

Figure 4.4: Linear motion of the damper cylinder and fluid.

of the center of gravity of the cylinder/fluid is

$$h + x_{cg}\alpha + x_2\phi = h + x_{cg}\alpha + x_2\frac{L_r}{L_l + L_r}\beta = \left\{1 \quad x_{cg} \quad x_2\tfrac{L_r}{L_l+L_r}\right\}\begin{Bmatrix} h \\ \alpha \\ \beta \end{Bmatrix} \tag{4.17}$$

so that taking the derivatives of the system states w.r.t. time, the velocity of the center of gravity of the cylinder is:

$$v_{cg} = \left\{1 \quad x_{cg} \quad x_2\tfrac{L_r}{L_l+L_r}\right\}\begin{Bmatrix} \dot{h} \\ \dot{\alpha} \\ \dot{\beta} \end{Bmatrix} \tag{4.18}$$

Then the kinetic energy of the linear motion can be expressed as

$$\begin{aligned} T =& \frac{1}{2}\left\{\dot{h} \quad \dot{\alpha} \quad \dot{\beta}\right\} m_{cyl}\begin{Bmatrix} 1 \\ x_{cg} \\ x_2\frac{L_r}{L_l+L_r} \end{Bmatrix}\left\{1 \quad x_{cg} \quad x_2\tfrac{L_r}{L_l+L_r}\right\}\begin{Bmatrix} \dot{h} \\ \dot{\alpha} \\ \dot{\beta} \end{Bmatrix} + ... \\ &+ \frac{1}{2}\left\{\dot{h} \quad \dot{\alpha} \quad \dot{\beta}\right\} I_{cyl}\begin{Bmatrix} 0 \\ 1 \\ \frac{L_r}{L_l+L_r} \end{Bmatrix}\left\{0 \quad 1 \quad \tfrac{L_r}{L_l+L_r}\right\}\begin{Bmatrix} \dot{h} \\ \dot{\alpha} \\ \dot{\beta} \end{Bmatrix} \end{aligned} \tag{4.19}$$

or more compactly,

$$T = \frac{1}{2}\left\{\dot{h} \quad \dot{\alpha} \quad \dot{\beta}\right\}\mathbf{M_{cyl}}\begin{Bmatrix} \dot{h} \\ \dot{\alpha} \\ \dot{\beta} \end{Bmatrix} \tag{4.20}$$

where $\mathbf{M_{cyl}}$ represents the mass matrix contribution for the cylinder and fluid of the

damper and is defined as:

$$\mathbf{M_{cyl}} = m_{cyl}\begin{bmatrix} 1 & x_{cg} & x_2\frac{L_r}{L_l+L_r} \\ x_{cg} & x_{cg}^2 & x_{cg}x_2\frac{L_r}{L_l+L_r} \\ x_2\frac{L_r}{L_l+L_r} & x_{cg}x_2\frac{L_r}{L_l+L_r} & \left(x_2\frac{L_r}{L_l+L_r}\right)^2 \end{bmatrix} + \ldots$$
$$+ I_{cyl}\begin{bmatrix} 0 & 0 & 0 \\ 0 & 1 & \frac{L_r}{L_l+L_r} \\ 0 & \frac{L_r}{L_l+L_r} & \left(\frac{L_r}{L_l+L_r}\right)^2 \end{bmatrix} \tag{4.21}$$

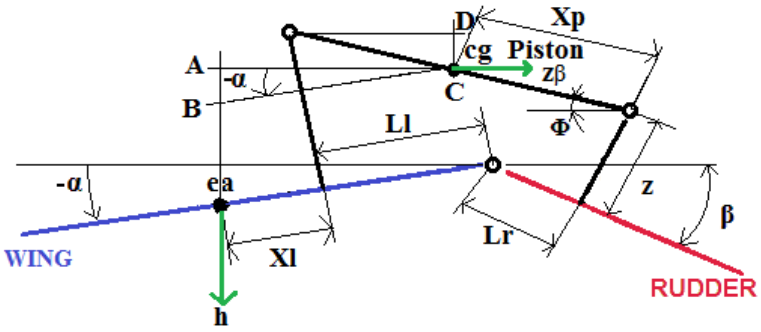

Figure 4.5: Schematic of the linear motion of the damper piston and rod.

The final step is to consider the motion of the piston and rod of the damper; a schematic of the linear motion of the piston center of gravity is presented in Figure 4.5. The linear motion of the center of gravity of the piston has two velocity components (for small rotations):

$$v_x = z\dot{\beta} \tag{4.22}$$

$$v_z = \dot{h} + \dot{\alpha}(x_l + L_l + L_r - x_p) + (L_l + L_r - x_p)\frac{L_r}{L_l + L_r}\dot{\beta} \tag{4.23}$$

Then, the kinetic energy of the linear motion of the piston and rod is given by

$$T = \frac{1}{2} m_p (v_x^2 + v_z^2) + \frac{1}{2} I_p \left(\dot{\alpha} + \frac{L_r}{L_l + L_r} \dot{\beta} \right)^2 \tag{4.24}$$

whereby substituting the expressions for v_x and v_z into the kinetic energy equation:

$$T = \frac{1}{2} \begin{Bmatrix} \dot{h} & \dot{\alpha} & \dot{\beta} \end{Bmatrix} \mathbf{M_p} \begin{Bmatrix} \dot{h} \\ \dot{\alpha} \\ \dot{\beta} \end{Bmatrix} \tag{4.25}$$

where $\mathbf{M_p}$ represents the mass matrix contribution for the piston and rod of the damper and is given by:

$$\mathbf{M_p} = m_p \begin{bmatrix} 1 & (x_l + L_l + L_r - x_p) & \frac{L_r(L_l+L_r-x_p)}{(L_l+L_r)} \\ (x_l + L_l + L_r - x_p) & (x_l + L_l + L_r - x_p)^2 & (x_l + L_l + L_r - x_p)\frac{L_r(L_l+L_r-x_p)}{(L_l+L_r)} \\ \frac{L_r(L_l+L_r-x_p)}{(L_l+L_r)} & (x_l + L_l + L_r - x_p)\frac{L_r(L_l+L_r-x_p)}{(L_l+L_r)} & \left[(x_l + L_l + L_r - x_p)\frac{L_r(L_l+L_r-x_p)}{(L_l+L_r)}\right]^2 + z^2 \end{bmatrix} + ...$$
$$+ I_p \begin{bmatrix} 0 & 0 & 0 \\ 0 & 1 & \frac{L_r}{L_l+L_r} \\ 0 & \frac{L_r}{L_l+L_r} & \left(\frac{L_r}{L_l+L_r}\right)^2 \end{bmatrix} \tag{4.26}$$

Then a matrix $\mathbf{M_{damp}}$ can be defined such that

$$\mathbf{M_{damp}} = 2\mathbf{M_{cyl}} + 2\mathbf{M_p} \tag{4.27}$$

where the cylinder and piston matrices are each accounted for twice since there are two dampers, with matching properties, attached to the system in a symmetric way.

4.3 Damper Design

The prototype damper is displayed in Figure 4.6 and described in *Paltera et al*[12][1]. The damper was fabricated out of aluminum and fitted with gasketed end-caps. The end-cap facing the rear of the model has a hole drilled out to fit the piston rod attachment to the rudder. Originally, the hole in the end cap was fitted with no seals to avoid excess friction, however in preliminary tests of the damper this resulted in an unacceptable amount of leakage of the damper fluid from the damper. To prevent leakage the opening was fitted with a spring-loaded PTFE shaft seal which did not add adverse friction to the seal and dynamic testing of the dampers, results of which are presented in the following section, resulted in damping behavior in agreement with theory. The piston design allows for interchangeable piston heads of differing materials as well as orifice shape and distribution. The piston is attached to the tail/rudder model with ball sockets on the main tail section and on the rudder section.

[1]Note an error in the damper's math model presented in Ref [12] due to a missing orifice discharge coefficient in the equations.

(a) The Prototype Damper

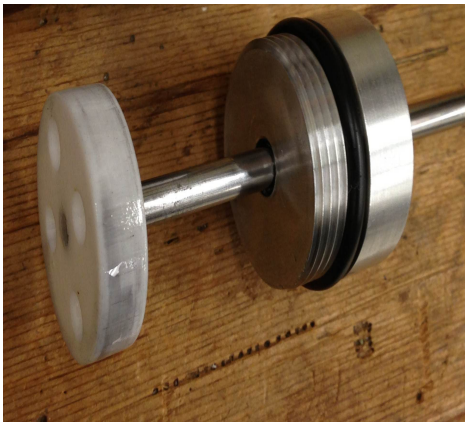

(b) Piston Head and Rod

Figure 4.6: (a) The damper, cylinder, piston/rod, and airfoil mount. (b) Piston Head with four orifices.

Table 4.1: Properties of the Velocity Squared Damper

Diameter of cylinder, D_c	0.03567 m
Diameter of piston, D_p	0.03377 m
Diameter of orifice, D_o	0.0043656 m
Number of orifices	4
Thickness of Piston, t	0.00952 m
Distance between cylinder and piston, d	0.00095 m
ρ	800 $\frac{kg}{m^3}$
μ	0.04 $Pa-s$
$m_{piston/rod}$	0.085 kg
$m_{cylinder/fluid}$	0.534 kg
Distance of CG from elastic axis, $x_{cg,cyl}$	0.1397 m
Distance between rudder mount and CG of cylinder/fluid, x_2	0.10414 m
Distance between rudder damper moment arm and hinge, L_R	0.0127 m
Distance between tail damper moment arm and hinge, L_L	0.282575 m
Distance between piston/rod CG to rod head, x_p	0.10668 m
Distance from elastic axis to attachment of damper, x_l	0.03556 m
Moment of inertia of cylinder about its CG, I_{cyl}	0.0001 $kg-m^2$
Moment of inertia of piston about its CG, I_p	0.00003 $kg-m^2$
Damper arm, z	0.0508 m

4.4 Damper Testing

The damping force of the dampers introduced in section 5.3 was experimentally measured in order to determine the C_{vsq} damping coefficient. Measurements are also compared to predictions obtained using the mathematical model presented in section 5.1. The damping force was analyzed at frequencies of 2 Hz, 3 Hz, 4 Hz, and 5 Hz; the amplitude of oscillation was varied to keep the velocity of the piston from getting too high. The testing matrix of frequencies and amplitudes is presented in Table 4.2.

Table 4.2: Damper Force Measurements: Test Matrix

$Frequency, f$	Amplitude $\mathcal{A}_p$
2 Hz	$\pm$ 26.3 mm
3 Hz	$\pm$ 17.5 mm
4 Hz	$\pm$ 13.1 mm
5 Hz	$\pm$ 10.5 mm

The tests were conducted in the University of Washington's AERB Design Lab with the tail/rudder model mounted to the wall and the plunge and pitch D.O.F. fixed; the dampers were attached to the model, acting in parallel, and filled with mineral oil. The motion of the rudder, and therefore the pistons, was driven by a linear actuator powered by an A.C. motor displayed in Figure 4.7(a). The RPM control of the motor allowed control of the test frequency while the crank radius could be varied, as seen in Figure 4.7(b), in order to control the amplitude of oscillation.

Force measurements were recorded by two PCB Quartz Force Sensors (Model: 208C01) mounted on the piston rod, between the cylinder and rudder connection; the sensors have a sensitivity of 112.41 $\frac{mV}{N}$ and a range of $\pm$ 44.48 N. One of the sensors, as mounted for the tests is displayed in Figure 4.7(c).

Sample time histories of the damper tests at the various frequencies are presented in Figure 4.8. Figure 4.9 compares the experimental 'force vs velocity' measurements to predictions obtained using equation 4.12. The cubic behavior expected is seen in

(a) Linear Actuator and Motor Set-up for Dynamic Tests of the Dampers Attached to the Tail/Rudder System

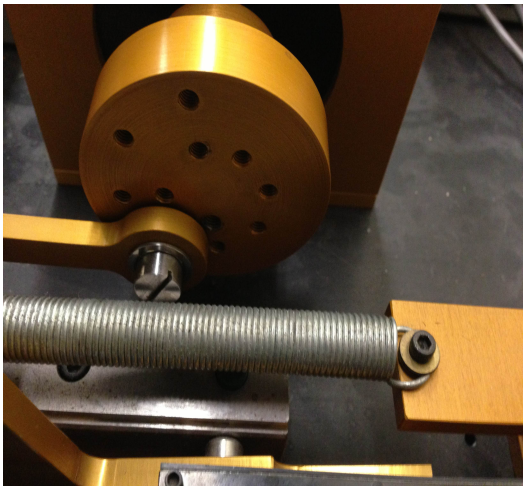

(b) Set-up of Crank Arm with Variable Radius

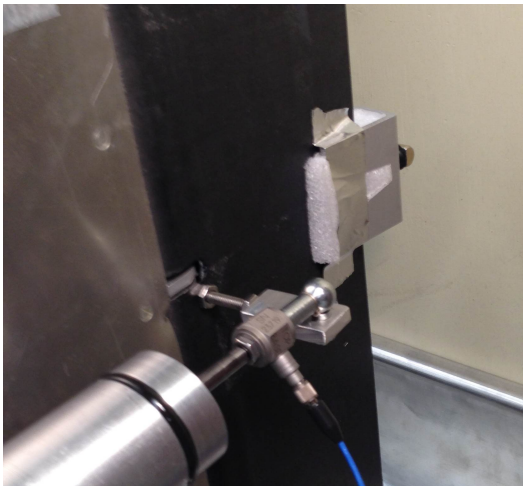

(c) Force Sensor for recording damping force from dynamic tests

Figure 4.7: Test Apparatus for Dynamic Tests of the VSQ Dampers

the experimental data. The linear 'force vs velocity squared' relationship is compared to prediction in Figure 4.10. The predicted value of the damping coefficient based on the theory developed in Section 4.1 is $C_{vsq,nom} = 0.805$. The experimental damping coefficient, determined from the linear fits of the experimental data give $C_{vsq,exp} =$

0.822 resulting in only a 2.1% difference between the predicted and experimental values, based on an assumed discharge coefficient of $C_d = 0.48$; therefore the design of the prototype damper has been validated and numerical simulation tools to analyze the linear, freeplay, and quadratic damping cases can now be developed.

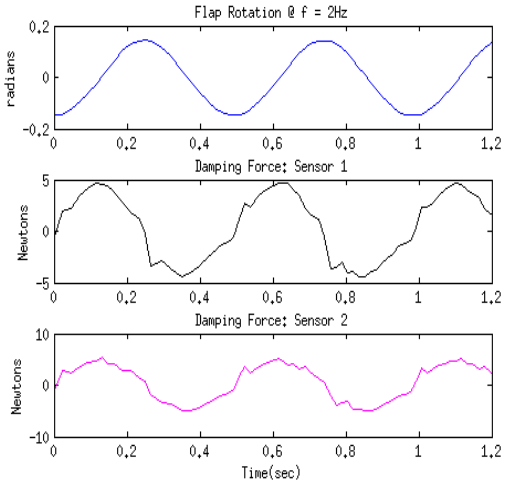

(a) f=2Hz, $\mathcal{A}_p = 26.3$ mm

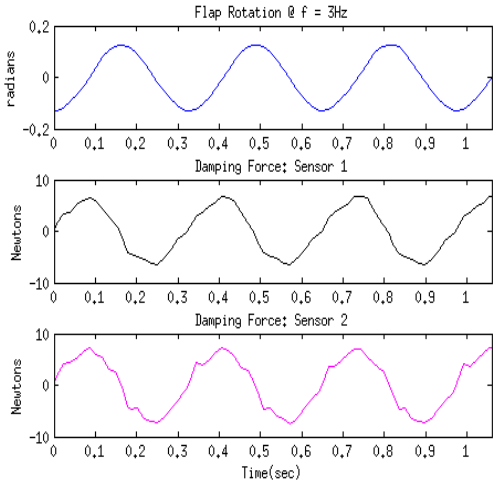

(b) f=3Hz, $\mathcal{A}_p = 17.5$ mm

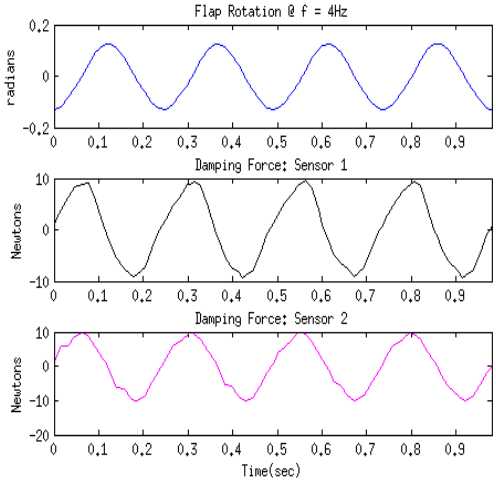

(c) f=4Hz, $\mathcal{A}_p = 13.1$ mm

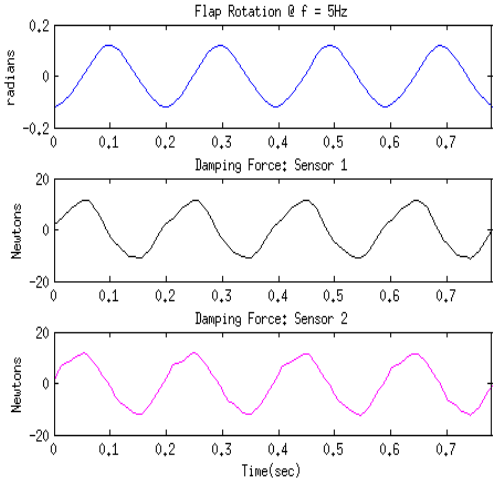

(d) f=5Hz, $\mathcal{A}_p = 10.5$ mm

Figure 4.8: Results of Flap Rotation and Damping Force Measurement Tests with Mineral Oil

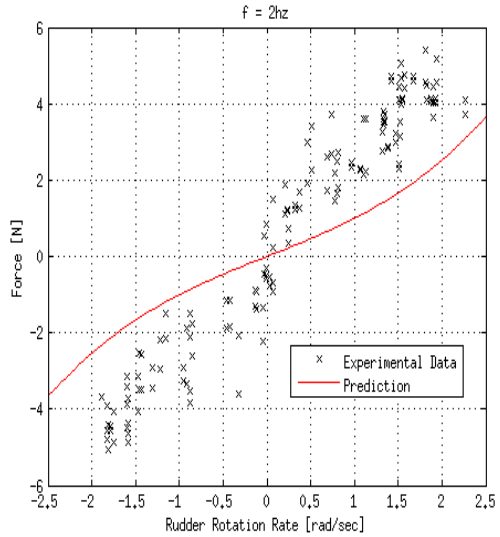

(a) f=2Hz, $\mathcal{A}_p$ = 26.3 mm

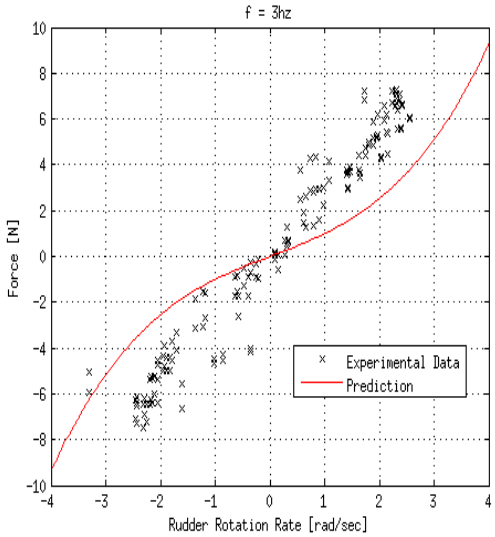

(b) f=3Hz, $\mathcal{A}_p$ = 17.5 mm

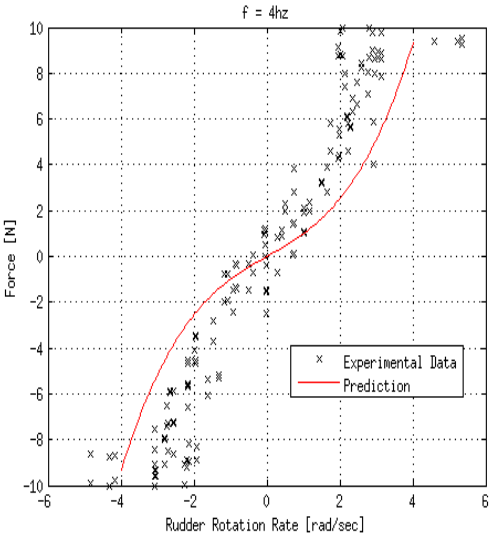

(c) f=4Hz, $\mathcal{A}_p$ = 13.1 mm

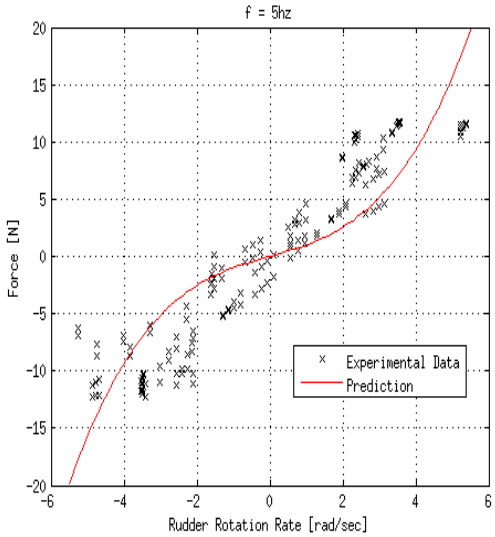

(d) f=5Hz, $\mathcal{A}_p$ = 10.5 mm

Figure 4.9: Experimental Force vs Rotation Rate Behavior compared to Predicted Behavior

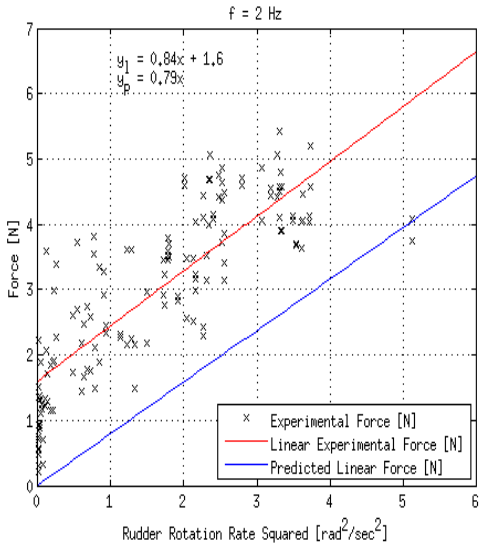

(a) f=2Hz, $\mathcal{A}_p$ = 26.3 mm

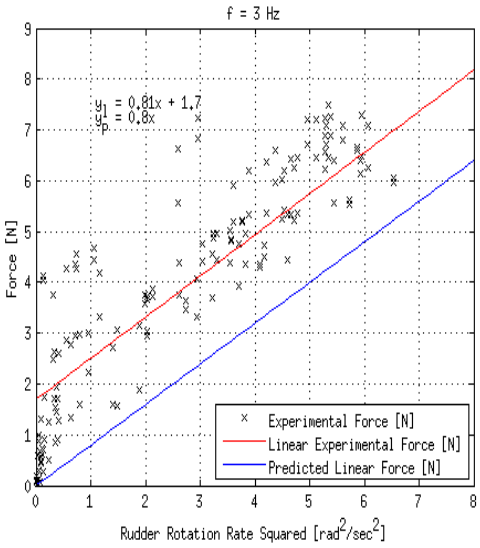

(b) f=3Hz, $\mathcal{A}_p$ = 17.5 mm

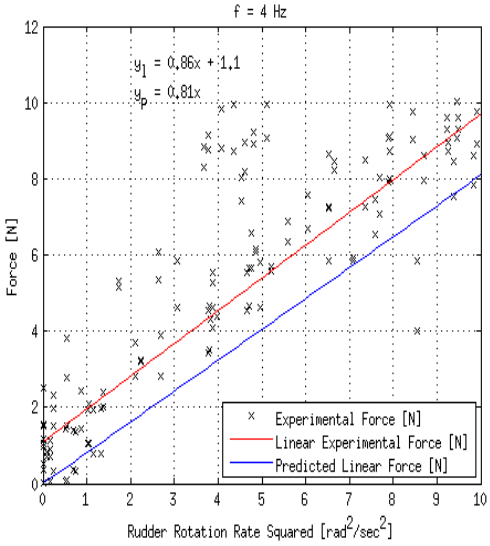

(c) f=4Hz, $\mathcal{A}_p$ = 13.1 mm

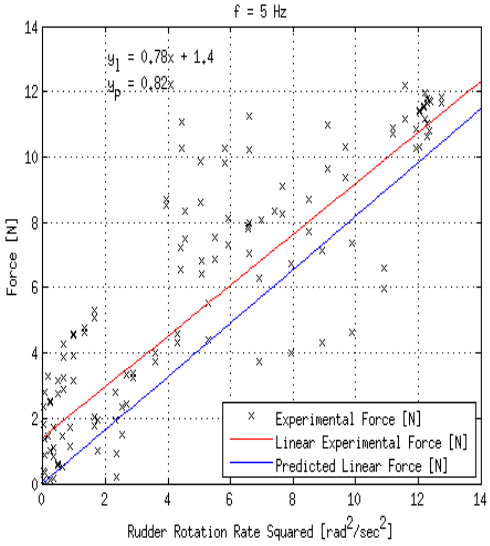

(d) f=5Hz, $\mathcal{A}_p$ = 10.5 mm

Figure 4.10: Experimental Force vs Rotation Rate Squared, Linear Behavior compared to Predicted Behavior

Chapter 5

NUMERICAL MODEL - FREQUENCY DOMAIN

Now that an understanding of the physical model and methods in which nonlinearities are introduced into the system has been established, it is possible to develop a set of numerical tools to efficiently and reliably predict the linear and nonlinear behavior of the aeroelastic section. Numerical solution techniques have been developed in both the frequency and time domains. Each method has some advantages and disadvantages compared to the other. However, by using both methodologies together a detailed prediction of the behavior of the system is obtained. This chapter presents the numerical model developed in the frequency domain and the next chapter details the development of the time domain model.

5.0.1 Equations of Motion for the Aeroelastic Section in the Frequency Domain

Because the hysteretic damping model in equation 2.6 is developed for simple harmonic motion, it can be easily integrated into equation 2.16, where aerodynamic forces are available for simple harmonic motion:

$$\mathbf{M_s}\ddot{\mathbf{q}} + j\mathbf{G_{st}}\mathbf{K_s}\mathbf{q} + \mathbf{K_s}\mathbf{q} = \frac{1}{2}\rho_\infty U_\infty^2 \mathbf{A}(\mathbf{jk})\mathbf{q} \tag{5.1}$$

Since the system is restricted to simple harmonic motion,

$$\mathbf{q} = \begin{Bmatrix} h \\ \alpha \\ \beta \end{Bmatrix} e^{j\omega t}, \dot{\mathbf{q}} = j\omega \begin{Bmatrix} h \\ \alpha \\ \beta \end{Bmatrix} e^{j\omega t}, \ddot{\mathbf{q}} = -\omega^2 \begin{Bmatrix} h \\ \alpha \\ \beta \end{Bmatrix} e^{j\omega t} \tag{5.2}$$

where the state variables are functions of $j\omega$. Equation 5.1 can be written in the

form:

$$[-\omega^2\mathbf{M_s} + j\mathbf{G_{st}}\mathbf{K_s} + \mathbf{K_s} - 0.5\rho_\infty U_\infty^2\mathbf{A(jk)}]\{q(j\omega)\} = \{0\} \tag{5.3}$$

Alternatively, equation 5.3 can be written as

$$[-\omega^2\mathbf{M_s} + \overline{\mathbf{K}} - 0.5\rho_\infty U_\infty^2\mathbf{A(jk)}]\{q(j\omega)\} = \{0\} \tag{5.4}$$

where

$$\overline{\mathbf{K}} = j\mathbf{G_{st}}\mathbf{K_s} + \mathbf{K_s} = [\mathbb{I} + j\mathbf{G_{st}}]\mathbf{K_s}. \tag{5.5}$$

and the symbol $\mathbb{I}$ denotes the identity matrix.

5.1 Linear Solution Methodology

The solution in the frequency domain is based on the V-g (or American) method of flutter analysis to determine the aeroelastic stability of the system. Since expressions for the aerodynamic forces are valid only for simple harmonic motion, the solution proceeds by forcing the system into simple harmonic motion after introducing *artificial* structural damping to the system. The structural damping construct required to force the system to oscillate in simple harmonic motion is g, and is added to the system in the following manner:

$$[-\omega^2\mathbf{M_s} + (1 + jg)\overline{\mathbf{K}} - 0.5\rho_\infty U_\infty^2\mathbf{A(jk)}]\{q(j\omega)\} = \{0\} \tag{5.6}$$

then dividing by ω^2 and using $k = \frac{\omega b}{U}$ yields

$$[-\mathbf{M_s} + \frac{(1 + jg)}{\omega^2}\overline{\mathbf{K}} - \frac{0.5\rho_\infty b^2}{k^2}\mathbf{A(jk)}]\{q(j\omega)\} = \{0\} \tag{5.7}$$

Combining the inertial and aerodynamic terms in equation 5.7 allows the system

to be presented in the form of a complex eigenvalue problem:

$$[\mathbf{R}(\mathbf{k}) - \lambda\mathbf{S}]\{q\} = \{0\} \tag{5.8}$$

where

$$\mathbf{R}(\mathbf{k}) = -\mathbf{M_s} - \frac{0.5\rho_\infty b^2}{k^2}\mathbf{A}(\mathbf{jk}) \tag{5.9}$$

$$\mathbf{S} = -\overline{\mathbf{K}} \tag{5.10}$$

$$\lambda = \frac{(1+jg)}{\omega^2} \tag{5.11}$$

The goal of the V-g method is to find the artificial damping required to force the system into simple harmonic motion (SHM) and the linear stability of the system is known in the following manner:

- If $g > 0$, damping added to force system to oscillate in SHM $\Rightarrow$ Unstable
- If $g < 0$, damping removed to force system to oscillate in SHM $\Rightarrow$ Stable
- If $g = 0$, system already oscillating in SHM $\Rightarrow$ Neutrally Stable

Then, after defining the atmospheric density ρ for a given test, the linear response is determined by looping over a set of reduced frequencies k that cover the range of interest for the problem; the intuitive desire would be to loop over flight speeds, however $U = 0$ corresponds to an infinite reduced frequency. For each reduced frequency, the matrices $\mathbf{R}(\mathbf{k})$ and $\mathbf{S}$ can be calculated and the eigenvalue problem 5.8 can be

solved. For each eigenvalue λ_i,

$$\omega_i = \sqrt{\frac{1}{Re(\lambda_i)}} \tag{5.12}$$

$$U_i = \frac{\omega_i b}{k} \tag{5.13}$$

$$g_i = \frac{Im(\lambda_i)}{Re(\lambda_i)} \tag{5.14}$$

After looping over all reduced frequencies, plots of artificial damping, 'g vs U' and frequency, 'ω vs U' can be constructed. On each plot there will be up to three branches corresponding to each D.O.F. The flutter speed, U_F, is the lowest velocity at which a g branch becomes positive; the corresponding ω branch at U_F is the flutter frequency, ω_F.

5.2 Nonlinear Solution Methodologies

5.2.1 The Describing Function Approach

The desire when dealing with a nonlinear system is to linearize it in some meaningful way, thus the describing function approach seeks to replace each nonlinear element with a linear describing function[19]. The class of describing functions that are applicable to this research are sinusoidal-input describing functions which are generally applied to periodic phenomena - a class of phenomena that includes LCO analysis. The sinusoidal-input describing functions assume that given a sinusoidal input, the only significant output of the nonlinear element of interest is a sinusoidal component at the input frequency. The linearization of the nonlinear terms is equivalent to determining the Fourier components of the nonlinearity and creating an equivalent linear system by only keeping the first order term(s).

The present goal is to develop numerical simulation tools, using the describing function approach, for nonlinear stability analysis of control surface flutter in an aeroelastic system with (1) freeplay about the control surface hinge line and, (2) with

zero hinge stiffness and quadratic damping, representing a failed actuator.

5.2.2 The Freeplay Case

With a structural freeplay region, as seen Figure 1.2, the relationship between the control surface rotation β and the restoring moment is expressed as:

$$H_\beta = \begin{cases} K_\beta(\beta - \delta) & \text{if } |\beta| \geq \delta, \beta > 0, \\ K_\beta(\beta + \delta) & \text{if } |\beta| \geq \delta, \beta < 0, \\ 0 & \text{otherwise} \end{cases} \tag{5.15}$$

where δ is the size of half of the total freeplay region. The size of the freeplay region can be varied with the adjustment of the leaf-spring support of the rudder as discussed previously in Chapter 3.

The describing function approach is a method for solving the nonlinear equation based on an assumed solution. Since the expected solutions are periodic oscillations, a fair assumption is that the flap rotation of the nonlinear system is sinusoidal oscillation such that

$$\beta = \beta_s \sin \omega t$$

Then the describing function approach for the freeplay case[25], applied to the piecewise restoring moment relationship, yields an equivalent rotational stiffness of the flap D.O.F. of the form

$$K_{\beta,eq} = F_\delta K_\beta \tag{5.16}$$

where F_δ is the describing function of the freeplay nonlinearity and is dependent on the ratio of freeplay gap to flap rotation amplitude. The describing function for freeplay is defined by:

$$F_\delta = \begin{cases} 0 & \text{if } -\delta < \beta_s < \delta, \\ \frac{1}{2}(\pi - 2t - \sin 2t) & \text{otherwise} \end{cases} \tag{5.17}$$

$$t = \sin^{-1}(\frac{\delta}{\beta_s})$$

Using equations 5.17 and 5.16, the relationship between the non-dimensional flap rotation and the equivalent stiffness is presented in Fig 5.1. As the flap amplitude of

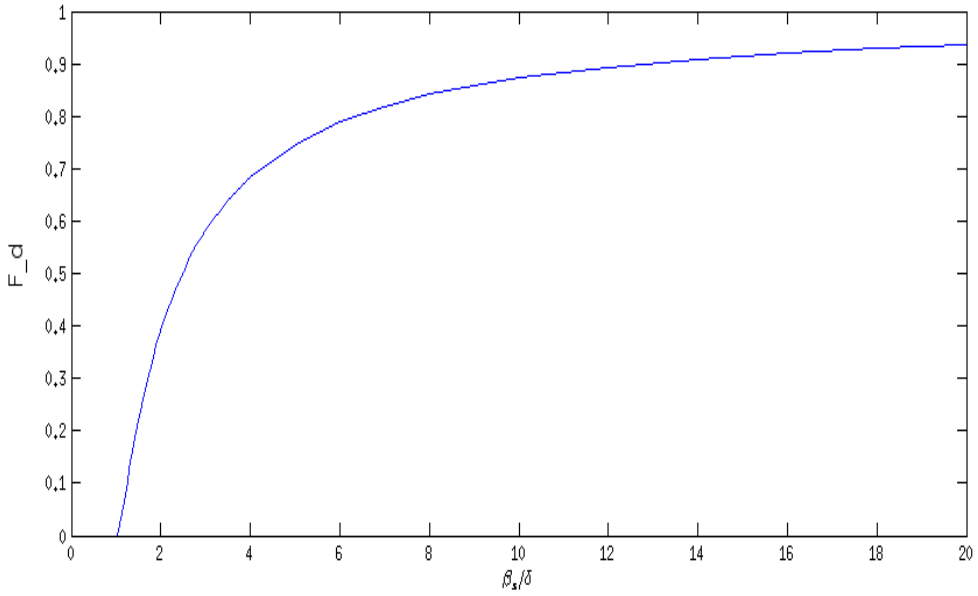

Figure 5.1: Ratio of equivalent stiffness $K_{\beta,eq}$ to nominal K_β vs non-dimensional flap rotation.

oscillation increases, $K_{\beta,eq}$ approaches the nominal value of K_β.

It is now possible to write equivalent linearized equations of motion for the freeplay scenario by replacing the H_β term with a $K_{\beta,eq}\beta$ dependency in the equations of motion. By examining equation 5.3, leaving the nominal structural stiffness matrix to determine the structural damping, the lone structural stiffness matrix can now be replaced by an equivalent structural stiffness matrix defined by

$$\mathbf{K_{DF}} = \begin{bmatrix} K_h & 0 & 0 \\ 0 & K_\alpha & 0 \\ 0 & 0 & K_{\beta,eq} \end{bmatrix} \tag{5.18}$$

so that equation 5.3 now takes the form

$$[-\omega^2(\mathbf{M_s} + 0.5\rho_\infty \frac{b^2}{k^2}\mathbf{A(jk)}) + j\mathbf{G_{st}K_s} + \mathbf{K_{DF}}]\{q(j\omega)\} = \{0\} \tag{5.19}$$

Equation 5.19 can be rearranged and recast as a generalized eigenvalue problem of the form:

$$[\overline{\mathbf{KK}} - \lambda \mathbf{M_e(k)}]\{q\} = \{0\} \tag{5.20}$$

where

$$\overline{\mathbf{KK}} = j\mathbf{G_{st}K_s} + \mathbf{K_{DF}} \tag{5.21a}$$

$$\mathbf{M_e} = \mathbf{M_s} + 0.5\rho_\infty \frac{b^2}{k^2}\mathbf{A(jk)} \tag{5.21b}$$

$$\lambda = \omega^2(1 - jg) \tag{5.21c}$$

Following the approach of the V-g method, simple harmonic solutions are sought, where the imaginary part of the eigenvalue, and thus the value of g, is zero.

For a given test, the atmospheric density ρ needs to be defined along with a vector of $\frac{\beta_s}{\delta}$. Below $\frac{\beta_s}{\delta} = 1$, there is no hinge restoring force, therefore the vector of $\frac{\beta_s}{\delta}$ has increasing values from 1 through a range of flap amplitudes of interest for the given problem. For each value of $\frac{\beta_s}{\delta}$, the describing function F_δ can be found and a vector of $K_{\beta,eq}$ values defined. The simulation involves two loops. The first loop over $K_{\beta,eq}$ determines the matrix $\overline{\mathbf{KK}}$. The inner loop is over reduced frequencies k as in Section 5.1. For each value of k, the matrix $\mathbf{M_e(k)}$ can be calculated and the

eigenvalue problem is fully defined. For each eigenvalue,

$$\omega_i = \sqrt{Re(\lambda_i)} \tag{5.22a}$$

$$U_i = \frac{\omega_i b}{k} \tag{5.22b}$$

$$g_i = -\frac{Im(\lambda_i)}{Re(\lambda_i)} \tag{5.22c}$$

For the linear system, U_F and ω_F corresponded to the lowest velocity at which a g branch goes positive. In the nonlinear case, there can be multiple crossings of the $g = 0$ axis, corresponding to different limit cycles. By tracking and storing the values U and ω for each crossing, a plot of non-dimensional flap amplitude of rotation, '$\frac{\beta_s}{\delta}$ vs. U' is generated.

5.2.3 The Quadratic Damping Case

The paper by Gordon[6] analyzes the effect of two different nonlinear terms: (1) quadratic damping representing a failed actuator, and (2) a Coulomb friction damping moment acting in parallel with the structural restoring moment including freeplay. In this research only the quadratic damping case is investigated.

The application of the describing function method, in the case of quadratic damping, again seeks to create an equivalent linear system by determining the Fourier coefficients (N_i) of the response of the nonlinear system and keeping only the first order terms. In the case of the hinge nonlinearity it is again assumed that $\beta = \beta_s \sin \omega t$ and that

$$F(\beta, s\beta) = N_0 + N_1\beta + \frac{N_2}{\omega}s\beta \tag{5.23}$$

Applying the describing function technique for the quadratic damping scenario, Gordon [6] presents that $N_0 = N_1 = 0$, and

$$N_2 = \frac{8(2z)C_{vsq}\beta_s}{3\pi}\omega^2 \tag{5.24}$$

which leads to an expression for the hinge moment with flap amplitude of β_s of

$$H_\beta = \frac{8(2z)C_{vsq}\beta_s}{3\pi}\omega^2 j\beta \tag{5.25}$$

This is the describing function representation of the quadratic damping nonlinearity. Equation 5.25 can now be substituted into equation 5.3 to yield the equivalent linearized equations of motion. The dependency of equation 5.25 on $\omega^2\beta$ indicates that it will affect the $(3,3)$ term of the structural inertia matrix, $\mathbf{M_s}$. Writing the equations of motion for the linearized system with a quadratic damping nonlinearity and yields:

$$[-\omega^2\mathbf{M_{C_{vsq}}} + \overline{\mathbf{K_0}} - 0.5\rho_\infty U_\infty^2\mathbf{A(jk)}]\{q\} = \{0\} \tag{5.26}$$

where

$$\mathbf{M_{C_{vsq}}} = \mathbf{M_{TOT}} - \begin{bmatrix} 0 & 0 & 0 \\ 0 & 0 & 0 \\ 0 & 0 & -\frac{8C_{vsq}\beta_s}{3\pi}j \end{bmatrix} \tag{5.27}$$

$$\mathbf{M_{TOT}} = \mathbf{M_s} + \mathbf{M_{damp}} \tag{5.28}$$

$$\overline{\mathbf{K_0}} = j\mathbf{G_{st}}\mathbf{K_s} + \begin{bmatrix} K_h & 0 & 0 \\ 0 & K_\alpha & 0 \\ 0 & 0 & 0 \end{bmatrix} \tag{5.29}$$

$\mathbf{M_{damp}}$ is a matrix accounting for the contributions of the quadratic dampers to the inertial matrix of the system; the matrix $\mathbf{M_{damp}}$ was defined in equation 4.27. The $\overline{\mathbf{K_0}}$ matrix is calculated the same way as $\overline{\mathbf{K}}$, except the $(3,3)$ term of $\mathbf{K_s}$ has been set to zero since when the actuator fails, resulting in the quadratic damping nonlinearity, the hinge stiffness goes to zero; the structural damping is still calculated using the nominal $\mathbf{K_s}$ matrix. The value of C_{vsq} is the damping coefficient of the quadratic damping force. It was determined experimentally from dynamic tests of the dampers

in Chapter 4.

Equation 5.26 can now be re-written in the typical form of an eigenvalue problem

$$[\mathbf{S} - \lambda \mathbf{R}(\mathbf{jk})]\{q\} = \{0\} \tag{5.30}$$

where

$$\mathbf{S} = \overline{\mathbf{K_0}} \tag{5.31}$$

$$\mathbf{R}(\mathbf{jk}) = \mathbf{M_{C_{vsq}}} + 0.5\rho_\infty \frac{b^2}{k^2}\mathbf{A}(\mathbf{jk}) \tag{5.32}$$

In the previous cases, the definition of the eigenvalue was based on physical interpretation, however, in this case with $K_\beta = 0$, the question arises what the artificial damping addition to the equations means. Before, the jg multiplication of the stiffness matrix meant the addition of structural damping to force the system into simple harmonic motion, but this physical intuition fails when multiplying a zero element. If a purely mathematical perspective is taken as opposed to a physical one, then the artificial damping term is merely a means of analyzing complex frequencies from the V-g solution. While, eigenvalues for most values of k are complex, a simple harmonic motion solution will have a purely real eigenvalue, $\lambda = \omega^2$, so if a generic form of a complex eigenvalue, λ, is adopted, the imaginary part of λ can be tracked to find SHM points, in a manner similar to tracking g in the standard V-g formulation. Therefore, the λ in equation 5.30 is defined as

$$\lambda = Re(\lambda) + jIm(\lambda) \tag{5.33}$$

The numerical simulation now proceeds similarly to the freeplay case. Rather than $\frac{\beta_s}{\delta}$ values, only a vector β_s values increasing from zero through a flap amplitude of interest. Again two loops are required to fully define the eigenvalue problem at each

β_s and k combination. Then for each eigenvalue

$$\omega_i = \sqrt{Re(\lambda_i)} \tag{5.34}$$

$$U_i = \frac{\omega_i b}{k} \tag{5.35}$$

$$Im(\lambda)_i = Im(\lambda_i) \tag{5.36}$$

and plots of 'β vs U' can be generated.

5.2.4 Limit Cycle Stability

A brief discussion on what it means for a limit cycle to be stable or not is prudent at this point. A limit cycle is "an isolated closed trajectory; neighbouring trajectories are not closed and they either spiral towards or away from the limit cycle"[17]. If a limit cycle is stable, then the neighbouring trajectories will decay into the limit cycle amplitude. If a limit cycle is unstable, however, the neighbouring trajectories will diverge from the limit cycle amplitude.

A simple, physically intuitive method has been utilized in the simulations for this system to determine the stability of predicted limit cycles.

For each nonlinear scenario, freeplay and quadratic damping, the system is first solved with the nominal structural damping values. Once LCO predictions are obtained for the nominal values, the simulations are run twice more, once with a decrease in the structural damping values from nominal and then with an increase in the values from nominal. It is expected that if the structural damping in the system in decreased, then the amplitude of predicted LCOs will increase and if the structural damping in the system is increased then the LCO amplitudes will decrease; this expected behavior indicates a stable limit cycle. However, if for a certain LCO, an increase in structural damping results in an increase in the amplitude and a decrease in structural damping results in a decrease in the amplitude, then the limit cycle

is found to be unstable. The paper by *Gordon*[6] addresses the topic of limit cycle stability in a more mathematical way.

Chapter 6
NUMERICAL MODEL - TIME DOMAIN

One disadvantage of the frequency domain methodologies discussed in Chapter 5 is the assumption that motion of the system is simple harmonic; this assumption disallows the possibility of convergent, divergent, or non-periodic motion and the only type of nonlinear behavior that can be predicted in the frequency domain is LCO. Therefore, a linear time invariant (LTI) state-space model of the equations of motion has been developed using Roger's[15] approximation of the unsteady aerodynamics. The system of equations can then be numerically integrated in time in an efficient manner and account for all types of motion: convergent, divergent, non-periodic, and simple harmonic. The system responses in the time-domain can be analyzed in tandem with LCO predictions in the frequency domain to obtain a complete understanding of the expected behavior of the aeroelastic model.

Since the concept of hysteretic (structural) damping is only valid for simple harmonic motions, the hysteretic model is discarded and the structural damping present in the system is instead characterized by the one-term viscous damping model of equation 2.7 such that the basic equations of motion of the system in the time domain are represented by

$$[-\omega^2\mathbf{M_s} + j\omega\mathbf{C} + \mathbf{K_s} - 0.5\rho_\infty U_\infty^2\mathbf{A}(\mathbf{jk})]\{q(j\omega)\} = \{0\} \tag{6.1}$$

Next, as the numerical model is moved from the frequency domain to the time domain, care must be taken to be sure contributions to the equations of motion are transferred appropriately. Since the expressions for the aerodynamic forces and

moments derived in Chapter 2 are valid only for simple harmonic motion, they must be represented via an approximation that also allows for non-simple harmonic motions.

6.0.5 Aerodynamic Contributions in the Time Domain

Aerodynamic forces and moments are converted to the time domain following Roger's Approximation[15]. With the relation $k = \frac{\omega b}{U}$ the $\mathbf{A(jk)}$ matrix in equation 6.1 can be expressed directly in terms of ω as $\mathbf{A(j}\omega\mathbf{)}$. Roger's idea was to find an expression for the $\mathbf{A(j}\omega\mathbf{)}$ matrix, as a function of $j\omega$, that would be a known rational function Fourier transform. Then, via analytic continuation, since the transform is valid along the $j\omega$ axis (in the complex domain), it would also be valid to the left and right of the imaginary axis for $s = \sigma + j\omega$. The Fourier transform, therefore leads to a corresponding Laplace transform that would allow accounting for all motions. Roger approximated the aerodynamic force matrix as a function of frequency along the $j\omega$ axis via the following equation:

$$\mathbf{A(j}\omega\mathbf{)} = \mathbf{P_0} + j\omega\mathbf{P_1} - \omega^2\mathbf{P_2} + \sum_{n=1}^{l} \frac{j\omega}{j\omega + \beta_n}\mathbf{P_{n+2}} \tag{6.2}$$

where the $\mathbf{P}$ matrices are are fitted to tabulated data, $\mathbf{A(jk_0)}$, $\mathbf{A(jk_1)}$,...,$\mathbf{A(jk_N)}$, obtained in the frequency domain such that the tabulated reduced frequencies (k_0,k_1,...,k_N) cover the range of interest for the problem. The β terms are called the aerodynamic poles (or aerodynamic lag roots) and the number of aerodynamic poles used in a typical analysis is usually $l = 4$. Equation 6.2 can then be extended from the $j\omega$ axis to the complex plane, becoming a function of the Laplace variable as follows:

$$\mathbf{A(s)} = \mathbf{P_0} + s\mathbf{P_1} + s^2\mathbf{P_2} + \sum_{n=1}^{4} \frac{s}{s + \beta_n}\mathbf{P_{n+2}} \tag{6.3}$$

While the aerodynamic matrices ($\mathbf{A(j}\omega\mathbf{)}$,$\mathbf{A(s)}$) are generally complex valued, the aerodynamic poles (β_n) and the $\mathbf{P}$ matrices are real. The aerodynamic lag roots are typ-

ically pre-set and the **P** matrices need to be found from a fit of the tabulated data. To do this, equation 6.2, can be converted to a dependency on jk since $j\omega = jk\frac{U}{b}$:

$$\mathbf{A(jk)} \approx \overline{\mathbf{P_0}} + jk\overline{\mathbf{P_1}} - k^2\overline{\mathbf{P_2}} + \sum_{n=1}^{4} \frac{jk}{jk + \overline{\beta_n}} \overline{\mathbf{P_{n+2}}} \tag{6.4}$$

where

$$\overline{\mathbf{P_0}} = \mathbf{P_0} \tag{6.5a}$$

$$\overline{\mathbf{P_1}} = \mathbf{P_1}\frac{U}{b} \tag{6.5b}$$

$$\overline{\mathbf{P_2}} = \mathbf{P_2}\left(\frac{U}{b}\right)^2 \tag{6.5c}$$

$$\overline{\mathbf{P_{n+2}}} = \mathbf{P_{n+2}} \tag{6.5d}$$

$$\overline{\beta_n} = \beta_n\frac{b}{U} \tag{6.5e}$$

Then, the m, n^{th} element of the Roger approximation is

$$A_{m,n}(jk) \approx \overline{P_{0}}_{m,n} + jk\overline{P_{1}}_{m,n} - k^2\overline{P_{2}}_{m,n} + \sum_{n=1}^{4} \frac{k^2 + jk\overline{\beta_n}}{k^2 + \overline{\beta_n}^2} \overline{P_{n+2}}_{m,n} \tag{6.6}$$

where the fraction in the summation has now been split into is real and imaginary parts. To guarantee a perfect match between the approximation and the tabulated data at $k_0 = 0$, the steady state solution, then the approximation is exactly

$$A_{m,n}(jk = 0) = \overline{P_{0}}_{m,n} \tag{6.7}$$

such that

$$\overline{\mathbf{P_0}} = \mathbf{A(k = 0)} \tag{6.8}$$

For the case of four aerodynamic lag roots, there are then six unknowns of the Roger approximation remaining, $\overline{P_{1}}_{m,n}$, $\overline{P_{2}}_{m,n}$, $\overline{P_{3}}_{m,n}$, $\overline{P_{4}}_{m,n}$, $\overline{P_{5}}_{m,n}$, and $\overline{P_{6}}_{m,n}$. The

approximation is evaluated at each of the tabulated frequencies, so that at $k = k_1$:

$$-k_1^2\overline{P_2}_{m,n} + \frac{k_1^2}{k_1^2+\overline{\beta_1}^2}\overline{P_3}_{m,n} + \frac{k_1^2}{k_1^2+\overline{\beta_2}^2}\overline{P_4}_{m,n} + \frac{k_1^2}{k_1^2+\overline{\beta_3}^2}\overline{P_5}_{m,n} + ... + \frac{k_1^2}{k_1^2+\overline{\beta_4}^2}\overline{P_6}_{m,n} \approx Re(A_{m,n}(jk_1)) - A_{m,n}(k_0 = 0) \tag{6.9}$$

$$k_1\overline{P_1}_{m,n} + \frac{k_1\overline{\beta_1}}{k_1^2+\overline{\beta_1}^2}\overline{P_3}_{m,n} + \frac{k_1\overline{\beta_2}}{k_1^2+\overline{\beta_2}^2}\overline{P_4}_{m,n} + \frac{k_1\overline{\beta_3}}{k_1^2+\overline{\beta_3}^2}\overline{P_5}_{m,n} + ... + \frac{k_1\overline{\beta_4}}{k_1^2+\overline{\beta_4}^2}\overline{P_6}_{m,n} \approx Im(A_{m,n}(jk_1) \tag{6.10}$$

and likewise for each $k = k_1, ..., k_N$. These equations of the approximation can be written in matrix form as follows:

$$\begin{bmatrix} 0 & -k_1^2 & \frac{k_1^2}{k_1^2+\overline{\beta_1}^2} & \frac{k_1^2}{k_1^2+\overline{\beta_2}^2} & \frac{k_1^2}{k_1^2+\overline{\beta_3}^2} & \frac{k_1^2}{k_1^2+\overline{\beta_4}^2} \\ k_1 & 0 & \frac{k_1\overline{\beta_1}}{k_1^2+\overline{\beta_1}^2} & \frac{k_1\overline{\beta_2}}{k_1^2+\overline{\beta_2}^2} & \frac{k_1\overline{\beta_3}}{k_1^2+\overline{\beta_3}^2} & \frac{k_1\overline{\beta_4}}{k_1^2+\overline{\beta_4}^2} \\ \vdots & \vdots & \vdots & \vdots & \vdots & \vdots \\ 0 & -k_N^2 & \frac{k_N^2}{k_N^2+\overline{\beta_1}^2} & \frac{k_N^2}{k_N^2+\overline{\beta_2}^2} & \frac{k_N^2}{k_N^2+\overline{\beta_3}^2} & \frac{k_N^2}{k_N^2+\overline{\beta_4}^2} \\ k_N & 0 & \frac{k_N\overline{\beta_1}}{k_N^2+\overline{\beta_1}^2} & \frac{k_N\overline{\beta_2}}{k_N^2+\overline{\beta_2}^2} & \frac{k_N\overline{\beta_3}}{k_N^2+\overline{\beta_3}^2} & \frac{k_N\overline{\beta_4}}{k_N^2+\overline{\beta_4}^2} \end{bmatrix} \begin{Bmatrix} \overline{P_1}_{m,n} \\ \overline{P_2}_{m,n} \\ \overline{P_3}_{m,n} \\ \overline{P_4}_{m,n} \\ \overline{P_5}_{m,n} \\ \overline{P_6}_{m,n} \end{Bmatrix} \approx ... \tag{6.11}$$

$$\approx \begin{Bmatrix} Re(A_{m,n}(jk_1)) - A_{m,n}(k_0 = 0) \\ Im(A_{m,n}(jk_1)) \\ \vdots \\ Re(A_{m,n}(jk_N)) - A_{m,n}(k_0 = 0) \\ Im(A_{m,n}(jk_N)) \end{Bmatrix}$$

or, by re-naming the matrices, as

$$\mathbf{Lp} = \mathbf{R} \tag{6.12}$$

the matrix equation can be solved in a least squares manner via

$$\mathbf{L}^T\mathbf{L}\mathbf{p} = \mathbf{L}^T\mathbf{R} \tag{6.13}$$

The solution of equation 6.13 provides the m, n^{th} element of the $\overline{\mathbf{P_i}}$ $(i = 1 \rightarrow 4)$ matrices for the Roger Approximation of the m, n^{th} element of the aerodynamic matrix. Figure 6.1 presents a sample of the least square fitting results, between the approximated aerodynamic matrix and the tabulated data.

Now, with a given velocity U and density ρ, the $\mathbf{P_i}$ matrices can be found from the $\overline{\mathbf{P_i}}$ matrices and the β_i aerodynamic lag roots from the $\overline{\beta_i}$ lag roots:

$$\mathbf{P_0} = \overline{\mathbf{P_0}} \tag{6.14a}$$

$$\mathbf{P_1} = \overline{\mathbf{P_1}}\frac{b}{U} \tag{6.14b}$$

$$\mathbf{P_2} = \overline{\mathbf{P_2}}\left(\frac{b}{U}\right)^2 \tag{6.14c}$$

$$\mathbf{P_{n+2}} = \overline{\mathbf{P_{n+2}}} \tag{6.14d}$$

$$\beta_n = \overline{\beta_n}\frac{U}{b} \tag{6.14e}$$

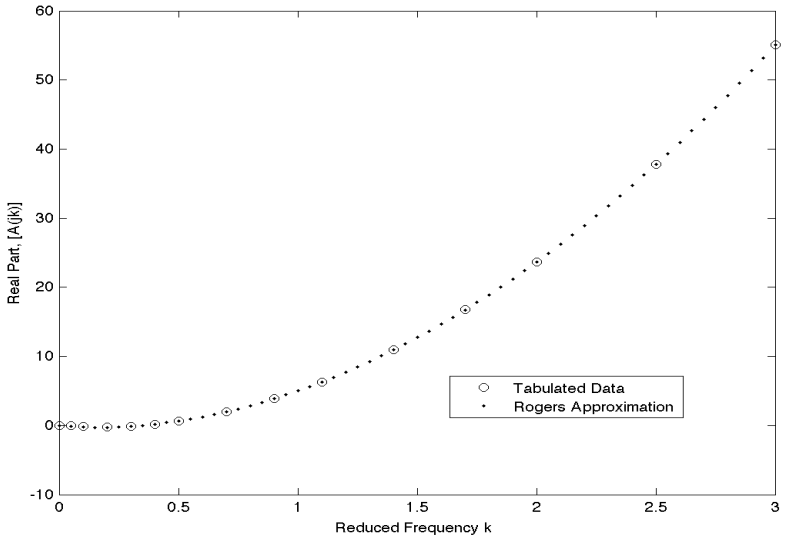

(a) $Re(\mathbf{A}_{(1,1)})$

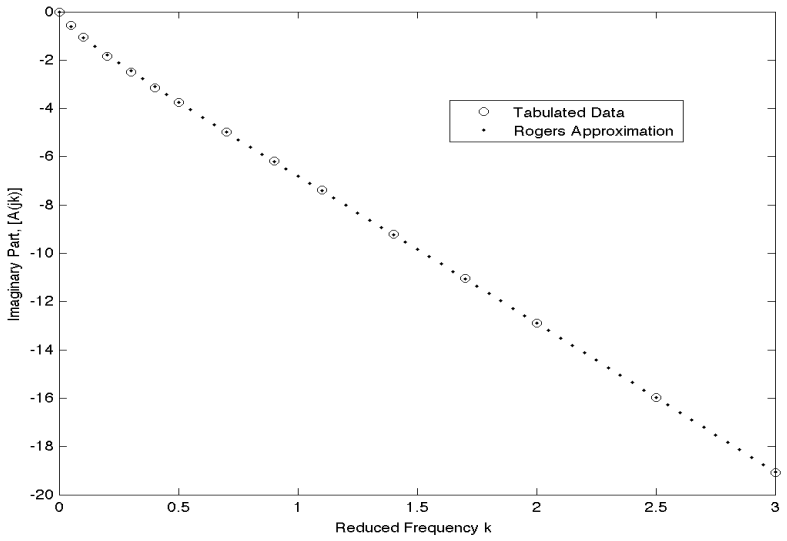

(b) $Im(\mathbf{A}_{(1,1)})$

Figure 6.1: Sample of the term-by-term fitting of the Roger Approximation Aerodynamic Matrix to Tabulated Data: The (1,1) term is presented, split into Real and Imaginary parts

6.0.6 The LTI State Space Equations of Motion

Now, using the Roger Approximation for the aerodynamic matrix, all terms of equation 6.1 are known as functions of frequency ω:

$$\left(-\omega^2 \mathbf{M_s} + j\omega \mathbf{C} + \mathbf{K_s} - 0.5\rho_\infty U_\infty^2 \left[\mathbf{P_0} + j\omega \mathbf{P_1} - \omega^2 \mathbf{P_2} + \sum_{n=1}^{4} \frac{j\omega}{j\omega + \beta_n} \mathbf{P_{n+2}} \right] \right) \{q(j\omega)\} = \{0\} \tag{6.15}$$

Transforming equation 6.15 into a dependency on the Laplace variable s and combining structural mass, stiffness, and damping terms with aerodynamic mass, stiffness, and damping terms yields:

$$\left(s^2 \overline{\overline{\mathbf{M}}} + s\overline{\overline{\mathbf{C}}} + \overline{\overline{\mathbf{K}}} - 0.5\rho_\infty U_\infty^2 \sum_{n=1}^{4} \frac{s}{s + \beta_n} \mathbf{P_{n+2}} \right) \{q(s)\} = \{0\} \tag{6.16}$$

where

$$\overline{\overline{\mathbf{M}}} = \mathbf{M_s} - 0.5\rho_\infty U_\infty^2 \mathbf{P_2} \tag{6.17a}$$

$$\overline{\overline{\mathbf{K}}} = \mathbf{K} - 0.5\rho_\infty U_\infty^2 \mathbf{P_0} \tag{6.17b}$$

$$\overline{\overline{\mathbf{C}}} = \mathbf{C} - 0.5\rho_\infty U_\infty^2 \mathbf{P_1} \tag{6.17c}$$

Equation 6.16 can be reduced to a set of first order equations by defining six new state vectors: two of the new states are made of structural states ($\{x_1\}$,$\{x_2\}$), the remaining states are aerodynamic states due to the aerodynamic lag terms in the

Roger Approximation; therefore, the new state vectors are:

$$\begin{aligned}
\{x_1\} &= \{q\} \\
\{x_2\} &= s\{q\} \Rightarrow s\{x_1\} = \{x_2\} \\
\{r_1\} &= \frac{s}{s+\beta_1}\{q\} \Rightarrow s\{r_1\} = -\beta_1\{r_1\} + \{x_2\} \\
\{r_2\} &= \frac{s}{s+\beta_2}\{q\} \Rightarrow s\{r_2\} = -\beta_2\{r_2\} + \{x_2\} \\
\{r_3\} &= \frac{s}{s+\beta_3}\{q\} \Rightarrow s\{r_3\} = -\beta_3\{r_3\} + \{x_2\} \\
\{r_4\} &= \frac{s}{s+\beta_4}\{q\} \Rightarrow s\{r_4\} = -\beta_4\{r_4\} + \{x_2\}
\end{aligned} \tag{6.18}$$

Five first-order equations for the state variables have now been defined, the sixth equation for $s\{x_2\}$ is:

$$\begin{aligned}
s\{x_2\} = &- \overline{\overline{\mathbf{M}}}^{-1}\overline{\overline{\mathbf{K}}}\{x_1\} - \overline{\overline{\mathbf{M}}}^{-1}\overline{\overline{\mathbf{C}}}\{x_2\} + 0.5\rho_\infty U_\infty^2 \overline{\overline{\mathbf{M}}}^{-1}\mathbf{P_3}\{r_1\} + ... \\
&+ 0.5\rho_\infty U_\infty^2 \overline{\overline{\mathbf{M}}}^{-1}\mathbf{P_4}\{r_2\} + 0.5\rho_\infty U_\infty^2 \overline{\overline{\mathbf{M}}}^{-1}\mathbf{P_5}\{r_3\} + 0.5\rho_\infty U_\infty^2 \overline{\overline{\mathbf{M}}}^{-1}\mathbf{P_6}\{r_4\}
\end{aligned} \tag{6.19}$$

The first-order equations above can now be put into matrix form as:

$$s\begin{Bmatrix}\{x_1\}\\ \{x_2\}\\ \{r_1\}\\ \{r_2\}\\ \{r_3\}\\ \{r_4\}\end{Bmatrix} = \begin{bmatrix} \mathbf{0} & \mathbb{I} & \mathbf{0} & \mathbf{0} & \mathbf{0} & \mathbf{0} \\ -\overline{\overline{\mathbf{M}}}^{-1}\overline{\overline{\mathbf{K}}} & -\overline{\overline{\mathbf{M}}}^{-1}\overline{\overline{\mathbf{C}}} & \frac{1}{2}\rho_\infty U_\infty^2 \overline{\overline{\mathbf{M}}}^{-1}\mathbf{P_3} & \frac{1}{2}\rho_\infty U_\infty^2 \overline{\overline{\mathbf{M}}}^{-1}\mathbf{P_4} & \frac{1}{2}\rho_\infty U_\infty^2 \overline{\overline{\mathbf{M}}}^{-1}\mathbf{P_5} & \frac{1}{2}\rho_\infty U_\infty^2 \overline{\overline{\mathbf{M}}}^{-1}\mathbf{P_6} \\ \mathbf{0} & \mathbb{I} & -\beta_1\mathbb{I} & \mathbf{0} & \mathbf{0} & \mathbf{0} \\ \mathbf{0} & \mathbb{I} & \mathbf{0} & -\beta_2\mathbb{I} & \mathbf{0} & \mathbf{0} \\ \mathbf{0} & \mathbb{I} & \mathbf{0} & \mathbf{0} & -\beta_3\mathbb{I} & \mathbf{0} \\ \mathbf{0} & \mathbb{I} & \mathbf{0} & \mathbf{0} & \mathbf{0} & -\beta_4\mathbb{I} \end{bmatrix} \begin{Bmatrix}\{x_1\}\\ \{x_2\}\\ \{r_1\}\\ \{r_2\}\\ \{r_3\}\\ \{r_4\}\end{Bmatrix} \tag{6.20}$$

where $\mathbb{I}$ is a $3x3$ unit matrix and $\mathbf{0}$ is a $3x3$ null matrix.

Equation 6.20 is a state-space representation of the equations of motion of the aeroelastic system, and can be written more compactly as

$$\dot{\mathbf{x}} = \mathbf{A_p}\mathbf{x} \tag{6.21}$$

where

$$\mathbf{x} = \begin{Bmatrix} \{x_1\} \\ \{x_2\} \\ \{r_1\} \\ \{r_2\} \\ \{r_3\} \\ \{r_4\} \end{Bmatrix} \tag{6.22}$$

is the state vector and the system matrix $\mathbf{A_p}$ is the $18x18$ matrix in equation 6.20 and the subscript p representing "plant", and has been adopted from aeroservoelastic notation.

6.1 Linear Solution Methodology

Since unsteady aerodynamic forces/moments are only available for simple harmonic motion, only the flutter point on the g vs. U and ω vs. U plots developed using the V-g methods has physical significance and data on damping or frequencies of the system below the flutter point are not available. The LTI formulation of the problem, however, is able to account for all motions: convergent, divergent, non-periodic, and simple harmonic. Time domain results, therefore, can easily be used in conjunction with flight test or wind tunnel data.

To evaluate the stability of the system using the state-space model, the analysis can be carried out in such a way that it simulates a flight (or wind tunnel) test. At a given atmospheric density ρ (fixed throughout the test), simulated flight speed is

incremented from an initial speed U_{start} given by

$$U_{start} = \frac{\omega_{min} b}{k_N} \tag{6.23}$$

where ω_{min} is the highest structural frequency of the system and k_N is the highest reduced frequency of the tabulated set. The linear flutter speed of the system is evaluated using a root-locus technique. Using predefined $\overline{\beta}_i$ $(i = 1 \rightarrow 4)$ values and a vector of tabulated reduced frequencies and looping over flight speeds, the $\mathbf{P}$ matrices can be determined from the $\overline{\mathbf{P}}$ matrices and the β values from the $\overline{\beta}$ values. At each flight speed determining the $\overline{\overline{\mathbf{M}}}$, $\overline{\overline{\mathbf{K}}}$, and $\overline{\overline{\mathbf{C}}}$ matrices allows the plant matrix to be fully defined. At each flight speed the corresponding complete set of eigenvalues of $\mathbf{A_p}$ are found and stored and a root-locus plot for the system can be generated by plotting the eigenvalues on the complex plane. Branches of the root-locus plot correspond to motion of an eigenvalue due to increasing speed; when one of the branches crosses the $j\omega$ axis, stability is lost and the corresponding velocity U is the flutter speed.

6.2 Nonlinear Solution Methodologies

6.2.1 The Freeplay Case

In order to incorporate the freeplay nonlinearity into the state-space representation, a vector representing the relationship between the control rotation β and the restoring moment must be included in equation 6.16 such that

$$\left(s^2\mathbf{M_s} + s\mathbf{C} + \mathbf{K} - 0.5\rho_\infty U_\infty^2 \left[\mathbf{P_0} + s\mathbf{P_1} + s^2\mathbf{P_2} + \sum_{n=1}^{4} \frac{s}{s+\beta_n} \mathbf{P_{n+2}} \right] \right) \{q(s)\} = -\{\mathbf{f}_\beta\} \tag{6.24}$$

where the β entry of the stiffness matrix $\mathbf{K_s}$ is set to zero since the nonlinear vector $\mathbf{f}_\beta$ dictates the nonlinear restoring force and

$$\mathbf{f}_\beta = \begin{Bmatrix} 0 \\ 0 \\ H_\beta \end{Bmatrix} \tag{6.25}$$

and H_β, given by equation 5.15 for the freeplay case, is

$$H_\beta = \begin{cases} K_\beta(\beta - \delta) & \text{if } |\beta| \geq \delta, \beta > 0, \\ K_\beta(\beta + \delta) & \text{if } |\beta| \geq \delta, \beta < 0, \\ 0 & \text{otherwise} \end{cases} \tag{6.26}$$

then using the previously defined $\overline{\overline{\mathbf{M}}}$, $\overline{\overline{\mathbf{K}}}$(with $\mathbf{K_s}(3,3) = 0$), and $\overline{\overline{\mathbf{C}}}$ matrices:

$$\left(s^2\overline{\overline{\mathbf{M}}} + s\overline{\overline{\mathbf{C}}} + \overline{\overline{\mathbf{K}}} - 0.5\rho_\infty U_\infty^2 \sum_{n=1}^{4} \frac{s}{s+\beta_n} \mathbf{P_{n+2}} \right) \{q(s)\} = -\{\mathbf{f}_\beta\} \tag{6.27}$$

which can again be reduced to a set of first order equations as defined above, however, the first order equation for $s\{x_2\}$ must be redefined to take $\mathbf{f}_\beta$ into account. Then,

$$\begin{aligned} s\{x_2\} = &- \overline{\overline{\mathbf{M}}}^{-1}\overline{\overline{\mathbf{K}}}\{x_1\} - \overline{\overline{\mathbf{M}}}^{-1}\overline{\overline{\mathbf{C}}}\{x_2\} + 0.5\rho_\infty U_\infty^2 \overline{\overline{\mathbf{M}}}^{-1}\mathbf{P_3}\{r_1\} + ... \\ &+ 0.5\rho_\infty U_\infty^2 \overline{\overline{\mathbf{M}}}^{-1}\mathbf{P_4}\{r_2\} + 0.5\rho_\infty U_\infty^2 \overline{\overline{\mathbf{M}}}^{-1}\mathbf{P_5}\{r_3\} + 0.5\rho_\infty U_\infty^2 \overline{\overline{\mathbf{M}}}^{-1}\mathbf{P_6}\{r_4\} - ... \\ &- \overline{\overline{\mathbf{M}}}^{-1}\{\mathbf{f}_\beta\} \end{aligned} \tag{6.28}$$

As before, the six first-order equations can be represented in matrix form and presented in a state-space representation as:

$$\dot{\mathbf{x}} = \mathbf{A_p x} + \mathbf{B} \tag{6.29}$$

where $\mathbf{A_p}$ is the same as defined in equation 6.20 and the vector $\mathbf{B}$ is given by

$$\mathbf{B} = \begin{Bmatrix} \{0\}_{3x1} \\ -\overline{\overline{\mathbf{M}}}^{-1}\{\mathbf{f}_\beta\} \\ \{0\}_{3x1} \\ \{0\}_{3x1} \\ \{0\}_{3x1} \\ \{0\}_{3x1} \end{Bmatrix}_{18x1} \tag{6.30}$$

Using the state-space representation of the nonlinear system with freeplay given by equation 6.29, the response of the system can be determined using standard numerical time-integration techniques. The simulation progresses over flight speeds from U_{start} to a value expected to be above the flutter speed. At each flight speed, the plant matrix can be determined and response of the system is analyzed using standard Runge-Kutta numerical integration techniques (MATLAB's built in *ode45* is used for convenience). In the simulation, the rudder position β is tracked and a corresponding $\mathbf{B}$ vector found. In the case of LCO, once the response has reached a steady-state, the mean amplitude response of h, α, and β can be found and normalized to the size of the freeplay gap

$$\begin{aligned} h_{norm} &= \frac{h}{b\delta} \\ \alpha_{norm} &= \frac{\alpha}{\delta} \\ \beta_{norm} &= \frac{\beta}{\delta} \end{aligned} \tag{6.31}$$

The normalized values are stored, and plotted vs flight speed U.

Henon's Method

One issue with the above implementation is that there is no guarantee that the value of β at any of the time-steps will fall exactly at the value of δ, the "edge" of the freeplay zone, and therefore not fully capture the corners of the piecewise restoring

force relationship. Failure to capture this point accurately can result in growing round-off errors as the integration proceeds[5]. In order to ensure that the switching-point between linear sub-domains is accurately captured, Henon's method[8] can be incorporated into the numerical integration algorithm.

The trick of the Henon's method is to switch the independent and dependent variables of the numerical integration. In this case, the state variable β is switched from a dependent variable to an independent variable. In doing so, time becomes a dependent variable, and a switch of the integration scheme will yield the time at which the system reaches a certain β value. Henon's method has been incorporated into the simulation in the following manner. Within, the Runge-Kutta time integration:

- If a change is detected between linear sub-domains between two time steps:

    1. Go back to the previous time-step
    2. Switch the independent and dependent variables of the system as guided by Henon's method[8]
    3. Integrate over one space step from β_{before} (the last value of β from the time integration before the switch occured) to $\beta_{switch} = \delta$, with initial conditions based on the values of all state variables just before the switch. The integration stops at exactly $\beta = \delta$ and the result of this integration is the time at which the system reaches the piecewise switching point as well as the remaining state variables of the system.
    4. With the state values from the Henon integration known, return to the time integration algorithm and use the Henon state values as the initial conditions to resume the time integration.
    5. Continue time integration algorithm until another change in linear sub-domains is detected.

6.2.2 The Quadratic Damping Case

In the case of quadratic damping, the damping force acting about the the control surface hinge line is given by

$$F_D = C_{vsq}\dot{\beta}^2 sgn(\dot{\beta}) \tag{6.32}$$

which results in a moment about the hinge line, due to the contribution of two dampers of

$$H_{\beta,D} = 2zF_D \tag{6.33}$$

where

$$sgn(\dot{\beta}) = \begin{cases} +1 & \text{if } \dot{\beta} > 0, \\ -1 & \text{if } \dot{\beta} < 0 \end{cases} \tag{6.34}$$

and the equation representing the nonlinear system, equation 6.24, can be modified to account for the damping nonlinearity instead of freeplay:

$$\left(s^2\mathbf{M_s} + s\mathbf{C} + \mathbf{K} - 0.5\rho_\infty U_\infty^2 \left[\mathbf{P_0} + s\mathbf{P_1} + s^2\mathbf{P_2} + \sum_{n=1}^{l} \frac{s}{s+\beta_n}\mathbf{P_{n+2}}\right]\right)\{q(s)\} = -\{\mathbf{f_{damp}}\} \tag{6.35}$$

where

$$\mathbf{f_{damp}} = \begin{Bmatrix} 0 \\ 0 \\ H_{\beta,D} \end{Bmatrix} \tag{6.36}$$

and the β entry of the stiffness matrix $\mathbf{K_s}$ is set to zero to account for the loss of stiffness about the control surface hinge line. Following the procedure to reduce the system to first-order equations, an equivalent form of equation 6.29 can be obtained such that:

$$\dot{\mathbf{x}} = \mathbf{A_p}\mathbf{x} + \mathbf{D} \tag{6.37}$$

where $\mathbf{A_p}$ is given in equation 6.20 and

$$\mathbf{D} = \begin{Bmatrix} \{0\}_{3x1} \\ -\overline{\overline{\mathbf{M}}}^{-1}\{\mathbf{f_{damp}}\} \\ \{0\}_{3x1} \\ \{0\}_{3x1} \\ \{0\}_{3x1} \\ \{0\}_{3x1} \end{Bmatrix}_{18x1} \tag{6.38}$$

For the quadratic damping case, the inertial contributions of the dampers must be taken into account, so $\overline{\overline{\mathbf{M}}}$, when considering the quadratic damping scenario, is given by:

$$\overline{\overline{\mathbf{M}}} = \mathbf{M_{TOT}} - 0.5\rho_\infty U_\infty^2 \mathbf{P_2} \tag{6.39}$$

where $\mathbf{M_{TOT}}$ is given by equation 5.28.

The system response is determined using standard Runge-Kutta time integration. At each time-step, the rotational velocity of the rudder, $\dot{\beta}$ is tracked and the corresponding $\mathbf{D}$, calculated. When LCO occurs, mean amplitudes of the h, α, and β responses can be determined once the system reaches a steady-state, and then $\frac{h}{b}$, α, and β can be plotted vs flight speed U. Responses in the time-domain can vary depending on the initial conditions of the system, therefore simulations are run using multiple initial conditions to understand the possible changes in the system behavior.

For each of the cases of interest: linear, freeplay, and quadratic damping, plotting the time-domain responses alongside the frequency domain/describing function results, provides a complete numerical analysis of the system to understand the possible behavior of the system in any simulated flight regime up to the flutter velocity. Since wind tunnel data is not available to validate the numerical models with, the reliability of the code will be validated by running simulations for the Duke system parameters and comparing results to the proven data for that system.

Chapter 7
VALIDATION OF THE NUMERICAL MODELS

The desire when developing numerical tools to analyze a system is to validate the numerical simulations with experimental data before venturing into unexplored territory. Since, experimental wind tunnel data for the physical UW model is not currently available, the numerical models developed in the previous chapters must be validated in another way. The numerical tools allow for the parameters of any aeroelastic model of similar design to be used as inputs. Therefore, the numerical models can be used to analyze the Duke system for nonlinearities of interest and by comparing those results to numerical and experimental data obtained by the Duke research group, the numerical models developed in Chapter 5 and 6 for the linear and freeplay cases can be validated. Gordon's paper on the nonlinear damping case[6] will be used to validate the quadratic damping simulations. The system parameters of the Duke model used as inputs into the numerical model are taken from *Conner et al*[4].

7.1 Linear Flutter

First, the linear flutter speed was analyzed using the standard V-g and Root Locus methods presented earlier. Figure 7.1 illustrates the tracking of artificial damping branches, with the flutter velocity located where a branch becomes positive; also, there is a frequency coalescence of two of the DOF near the flutter speed. Figure 7.2 demonstrates the motion of eigenvalues due to increasing velocity and the stability of the system when viewed on the complex plane. The simulated numerical flutter speed was determined to be $U_F = 23.94\frac{m}{s}$ using the V-g methodology and $U_F = 23.92\frac{m}{s}$

using the root-locus LTI formulation. Flutter frequencies, determined from the V-g and Root-Locus methods were $\omega_F = 6.025Hz$ and $\omega_F = 6.013Hz$, respectively. Agreement between the two numerical methods is very high, but more importantly, both results are very close to the Duke numerical and experimental results: (1) $U_F = 23.9\frac{m}{s}/\omega_F = 6.112Hz$ (numerical) and (2) $U_F = 20.6\frac{m}{s}/\omega_F = 5.47Hz$ (experimental).

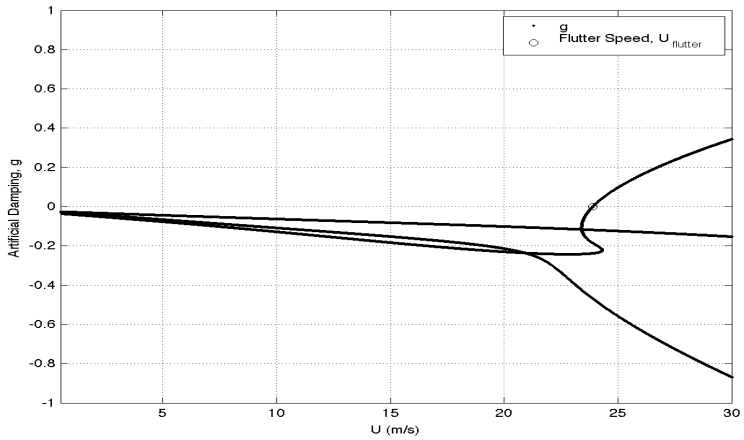

(a) Artificial Damping vs Velocity

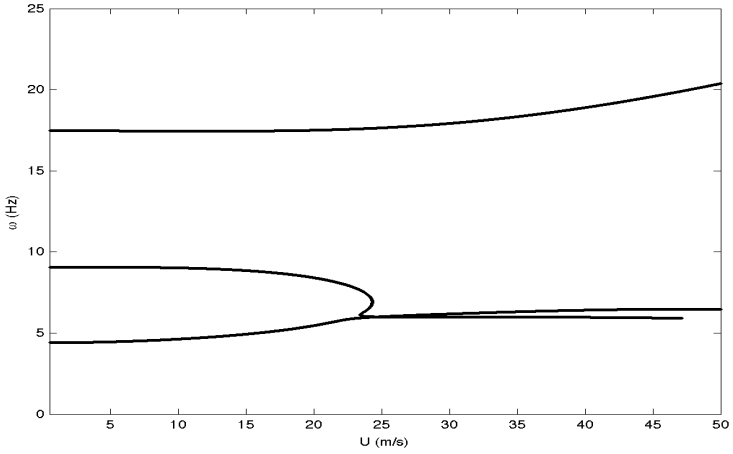

(b) Frequency vs Velocity

Figure 7.1: V-g flutter results for the Duke System of (a) 'g vs U': Crossing of the $g = 0$ axis at 23.94 $\frac{m}{s}$,and (b)'ω vs U': $\omega_F = 6.025$ Hz

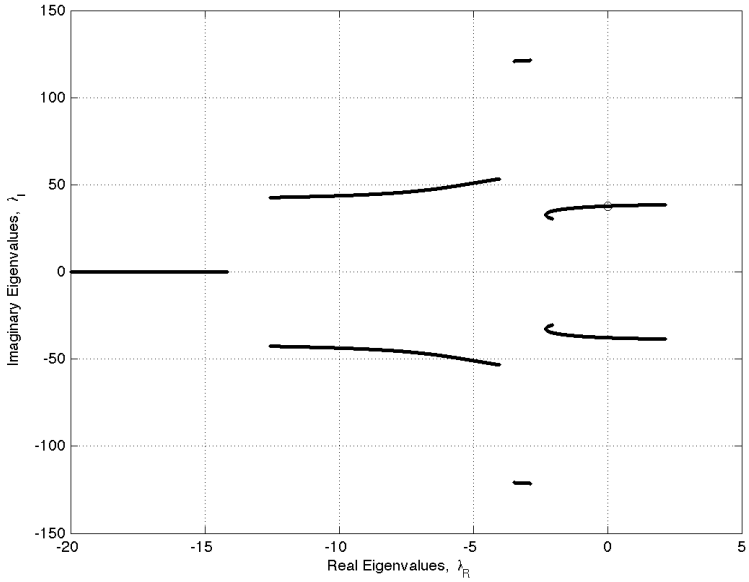

(a) Root Locus of Linear Duke System

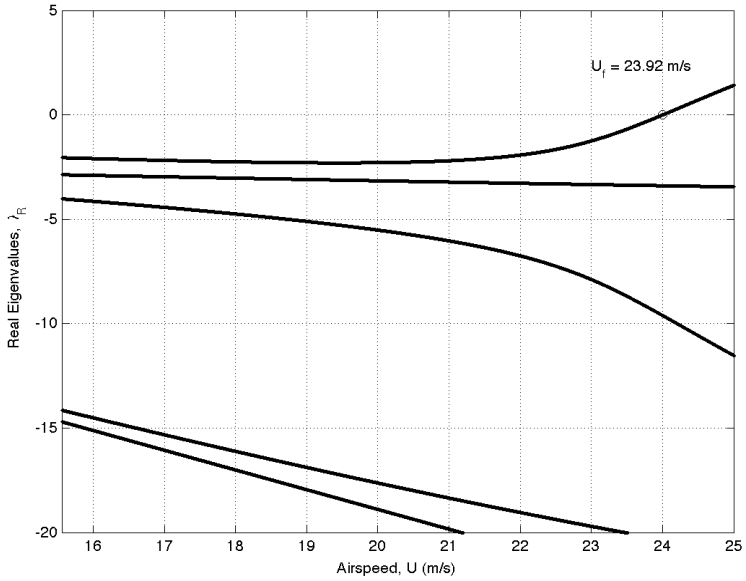

(b) Re(λ) vs U

Figure 7.2: Root Locus flutter analysis of the Duke system. (a) Root Locus plot of eigenvalue motion due to simulated velocity. (b) $U_F = 23.92\ \frac{m}{s}$

7.2 Freeplay Nonlinearity

Numerical simulations were run for a nominal freeplay gap of 4.24° ($\delta = \pm 2.12°$) and initial conditions of $h(0) = 0.02$, $\alpha(0) = 0$, and $\beta(0) = 0$ in the time domain. Figures 7.3(Flap Response), 7.4(Plunge Response), and 7.5(Plunge Response) compare predicted responses obtained using the describing function and direct time integration to results published by the Duke research group[4][18]. Limit cycle amplitudes and changes in system behavior, namely discrete jumps between limit cycles, compare extremely well. Between approximately $1.2U_{F,0}$ and $1.7U_{F,0}$($U_{F,0} = 7.01\frac{m}{sec}$ is the linear flutter speed corresponding to zero hinge stiffness), the direct time integration results appear to lose periodicity, particularly in the flap and plunge DOF, matching the observations obtained by *Conner et al*[4]. More importantly, the predicted system flap DOF response amplitudes match very well between the describing function and time integration models developed in this thesis. The steady-state frequency of the predicted LCOs also agrees with the data presented by the Duke team, as seen in Figure 7.6.

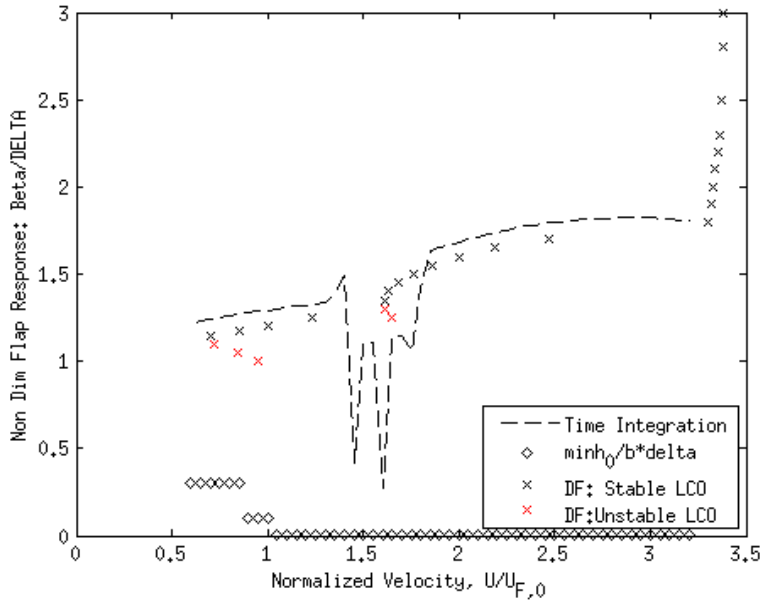

(a) Noble's Simulation Results

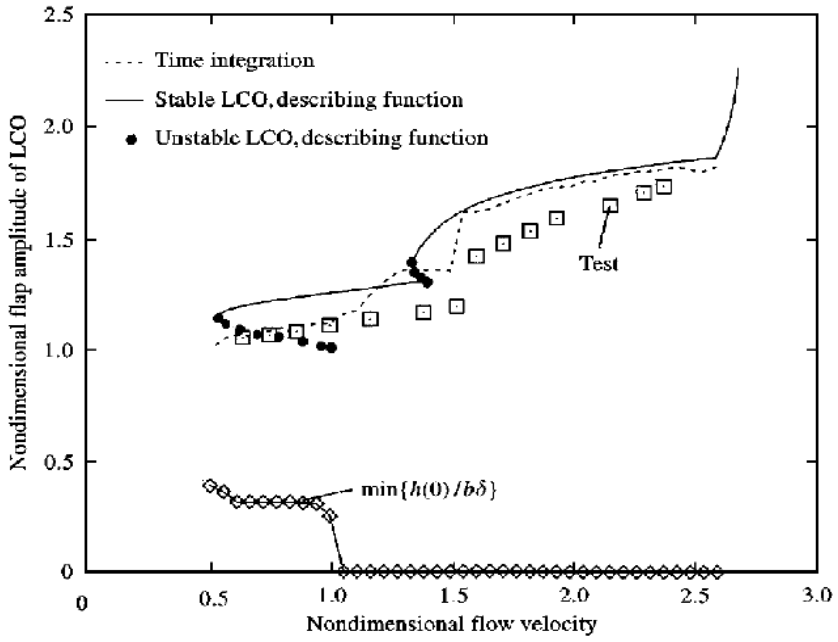

(b) Tang Results[18]

Figure 7.3: Non-dimensional flap amplitude response for the Duke System with Freeplay; minimum initial condition required for LCO vs Velocity: (a) Simulations performed using code developed at UW. (b) Tang Results

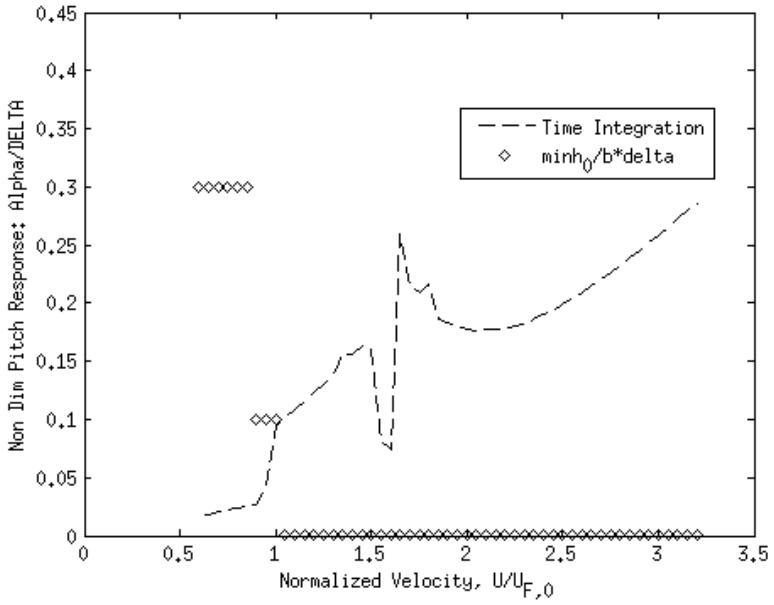

(a) Noble's Simulation Results

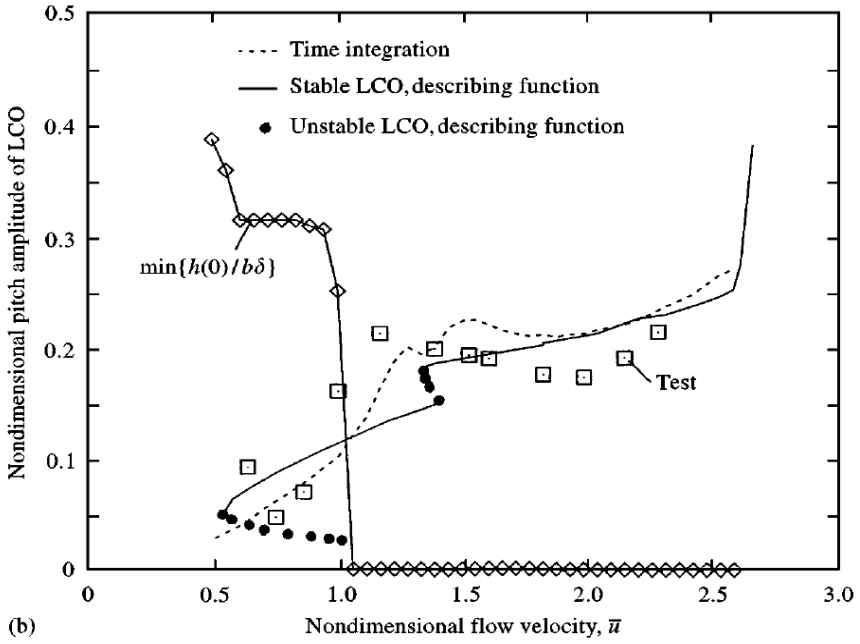

(b) Tang Results[18]

Figure 7.4: Non-dimensional pitch amplitude response for the Duke System with Freeplay; minimum initial condition required for LCO vs Velocity: (a) Simulations performed using code developed at UW. (b) Tang Results

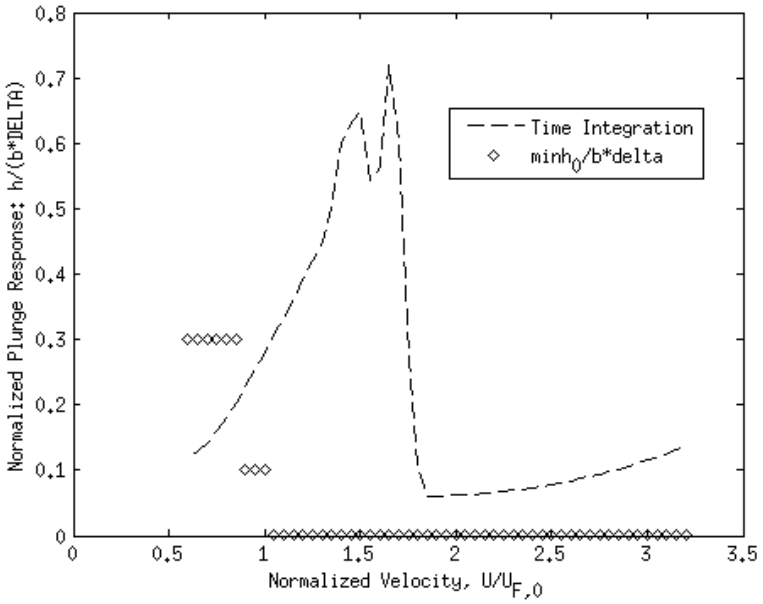

(a) Noble's Simulation Results

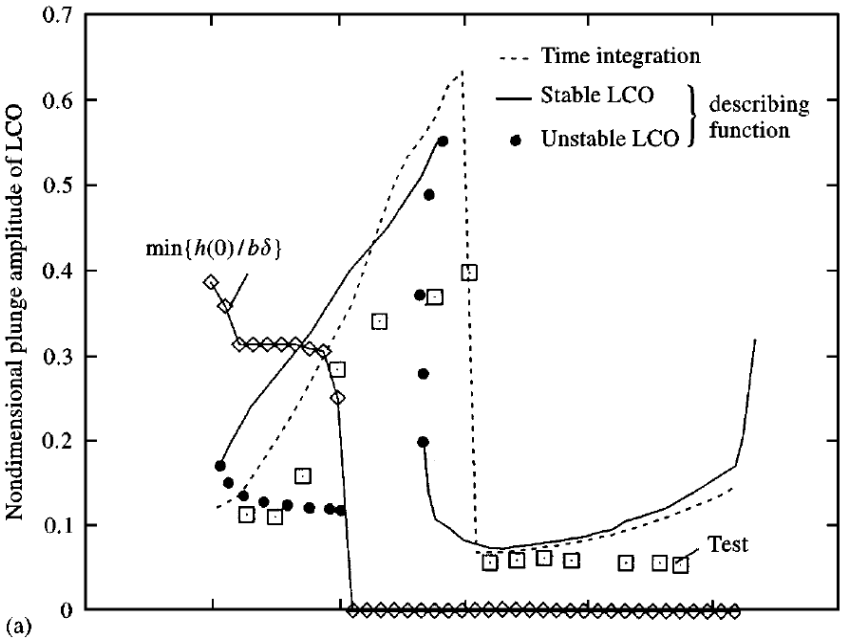

(b) Tang Results[18]

Figure 7.5: Non-dimensional plunge amplitude response for Duke System with Freeplay; minimum initial condition required for LCO vs Velocity: (a) Simulations performed using code developed at UW. (b) Tang Results

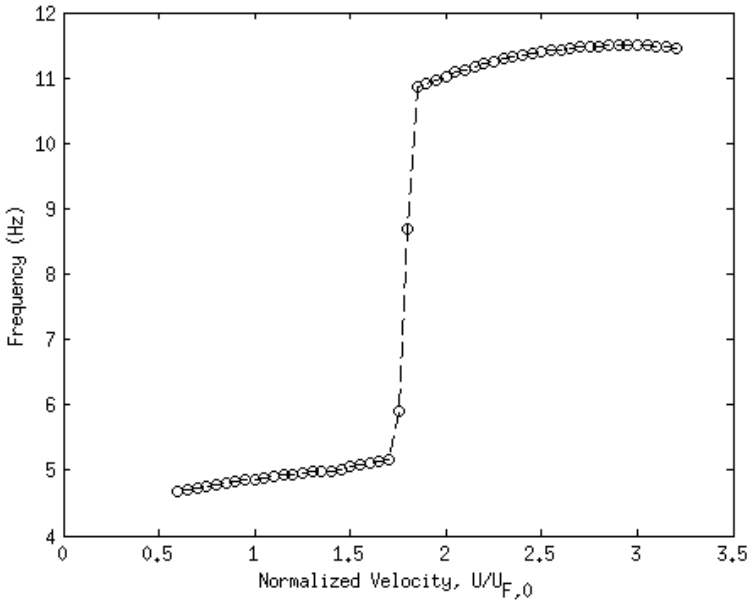

(a) Noble's Simulation Results

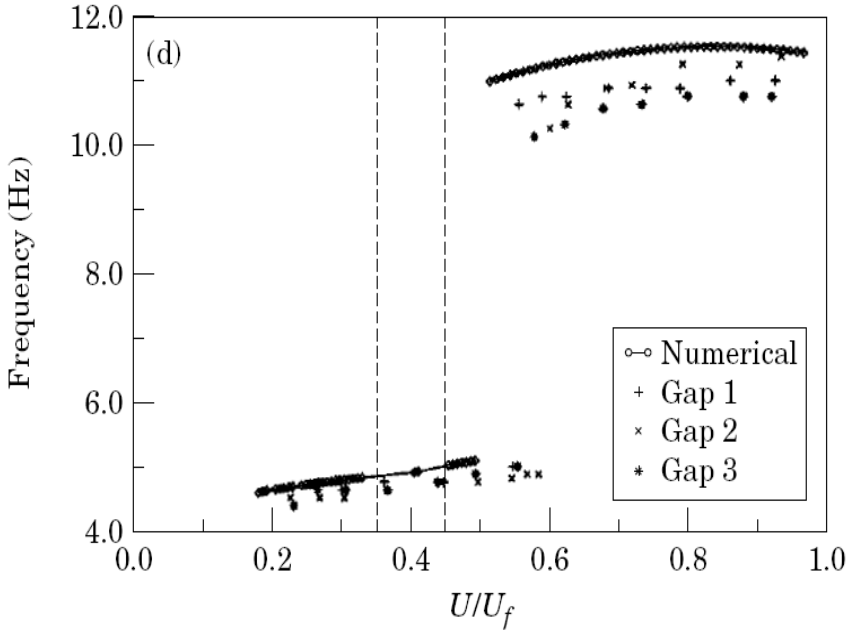

(b) Conner Results[4]

Figure 7.6: Steady-State Frequency of Predicted Limit Cycles vs Velocity: (a) Simulations performed using code developed at UW. (b) Conner Results (Note that Conner normalized velocities with respect to the linear flutter speed $U = 23.9\frac{m}{sec}$ and not $U_{F,0} = 7.01\frac{m}{sec}$.)

7.3 Quadratic Damping Nonlinearity

Results for the quadratic damping models are validated against results published by Gordon[6]. The model was run for two different initial conditions in the time domain, both with an initial displacement in the plunge DOF and zero components in the pitch and flap DOF. The first initial condition was $h(0) = 0.0508m$, $\alpha(0) = 0$, and $\beta(0) = 0$, while the second initial condition was $h(0) = 5.08 \times 10^{-5}m$, $\alpha(0) = 0$, and $\beta(0) = 0$. The results of the numerical simulations, along with data extracted from Gordon's results, are presented in Figure 7.7. Both initial conditions result in the same LCO amplitude, however, Gordon's results predict a drop into a lower amplitude LCO around $17\frac{m}{sec}$ which is not predicted by either the time domain or describing function results. The describing function results do predict the existence of a lower amplitude limit-cycle between $17 \leq U \leq 23\frac{m}{sec}$, however the results of these simulations indicate that it is an unstable limit-cycle. Below $U = 17\frac{m}{sec}$, the agreement between the numerical simulations and Gordon's predictions is excellent; agreement between limit-cycle frequencies determined by the numerical simulations and Gordon's predictions is very good through all flight regimes.

For each of the case studies of interest, linear, freeplay, and quadratic damping, the agreement between the describing function results, time domain results, and published data for the Duke system has been shown to be excellent. Also, flap amplitudes predicted by the describing function compare extremely well with amplitudes obtained using direct time integration. Based on this validation with accepted data, the numerical models are assumed to be accurate with high confidence and numerical analysis of the University of Washington (UW) experimental model can now be presented.

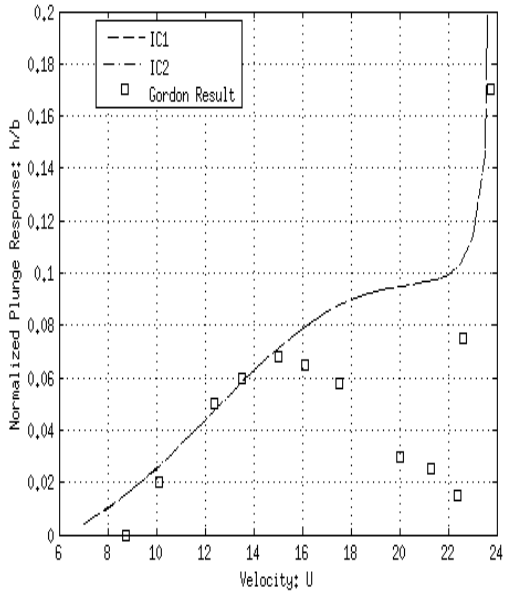

(a) Non-dimensional Plunge vs Velocity

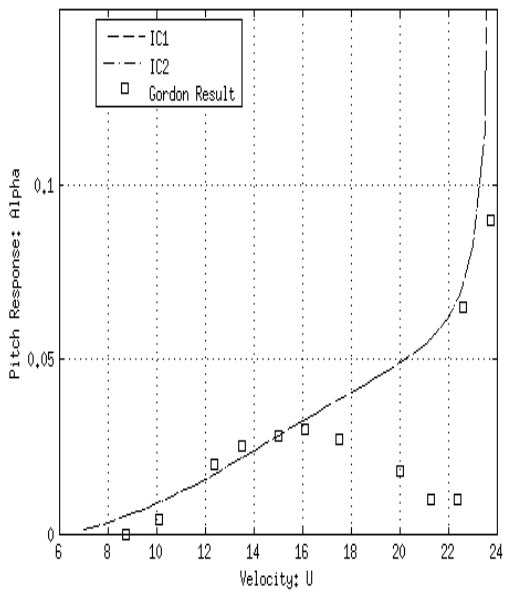

(b) Pitch Rotation vs Velocity

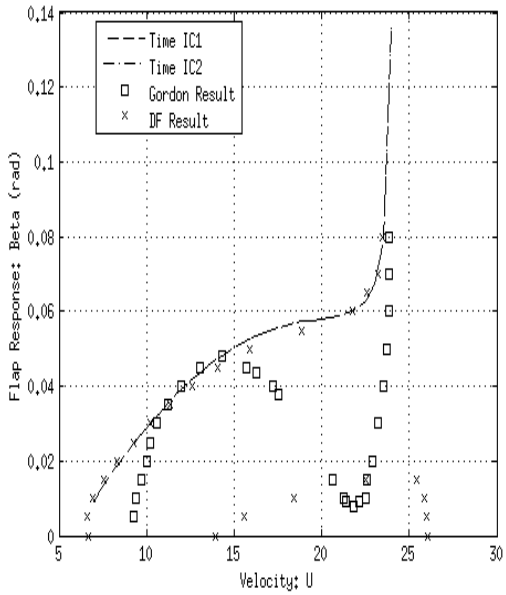

(c) Flap Rotation vs Velocity

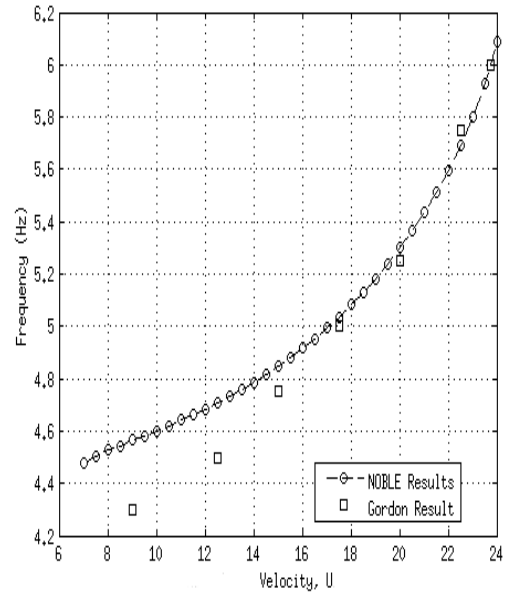

(d) Limit-Cycle Frequency vs Velocity

Figure 7.7: LCO amplitudes of the Duke System with Quadratic Damping. Results compared to Gordon[6].

Chapter 8

NUMERICAL RESULTS AND DISCUSSION

8.1 Linear Flutter

The linear flutter response of the University of Washington experimental model was determined for two different configurations. The first was a configuration with no dampers attached, which will be referred to as the nominal system from here on. The other configuration was analyzed with the dampers attached to the structure but not operating on the rudder, which will be referred to as the modified system. The goal is to have an idea of how the inertia of the dampers affects the linear flutter speed of the system before analyzing the nonlinear case. The nominal system is used for freeplay analysis, while the modified system is used for analysis of the quadratic damping nonlinearity.

The coupled natural frequencies of both the nominal and modified systems were determined by solving the eigenvalue problem $(\mathbf{K_s} - \omega^2 \mathbf{M_s})\Phi = 0$. The results are presented in Table 8.1.

Table 8.1: Coupled Natural Frequencies of Nominal and Modified Configurations

	Nominal Config.	Modified Config.
ω_h	3.17 Hz	2.95 Hz
ω_α	4.54 Hz	4.35 Hz
ω_β	15.7 Hz	11.72 Hz

The linear flutter response of the nominal system, displayed in Figure 8.1(a), shows the linear flutter speed to be $U_F^{nom} = 27.57\frac{m}{sec}$ and the frequency $\omega_F^{nom} = 9.72Hz$. The linear flutter speed of the modified system was determined to be $U_F^{mod} = 29.27\frac{m}{sec}$ with

a frequency $\omega_F^{mod} = 7.95Hz$ as presented in Figure 8.1(b).

A study was conducted on the effect of hinge leaf-spring stiffness on the flutter velocity, the results of which are presented in Figure 8.2 for the nominal system and Figure 8.3 for the modified system. The hinge stiffness was varied from 0 to 4.3 $\frac{N-m}{rad}$, where 4.3 is the actual value of the hinge spring stiffness. The flutter velocity of the nominal system at zero hinge stiffness is $U_{F,0}^{nom} = 4.86\frac{m}{sec}$ and remains relatively constant until $K_\beta \approx 1.29\frac{N-m}{rad}$ where there is a jump in the flutter velocity up to $15.5\frac{m}{sec}$. For $K_\beta > 1.29$, the flutter velocity gradually increases to the linear flutter speed. Not surprisingly, similar behavior is observed in the modified system. The zero stiffness flutter speed of the modified system is determined to be $U_{F,0}^{mod} = 6.36\frac{m}{sec}$.

In Figures 8.2(b) and 8.3(b), there is an expected jump in the flutter frequency corresponding to the jump in flutter velocity due to a possible change in the critical flutter mechanism. The flutter frequency at low stiffness values is a low frequency, near the plunge natural frequency, but at $K_\beta \approx 1.29\frac{N-m}{rad}$ the flutter frequency jumps to a high frequency that approaches the linear flutter frequency.

The effect of uncertainty in the structural damping approximation is also of interest in the linear regime. A study was conducted to determine flutter speeds and frequencies for a range of variation in the g_{st} values from the nominal values ($g_{st,h} = 0.0064$, $g_{st,\alpha} = 0.296$, $g_{st,\beta} = 0.124$). Figure 8.4 shows the effect of uncertainty in the g_{st} value for uncertainty up to $\pm 30\%$ on the nominal and modified configurations. For higher than expected values of g_{st}, the flutter velocity increases while the frequency decreases and the inverse is true for lower than expected values of g_{st}. The variation in speeds and frequencies is not too high ($< 1\frac{m}{sec}$ variation), indicating that the behavior of the system will not vary too much if the structural damping values are not exact.

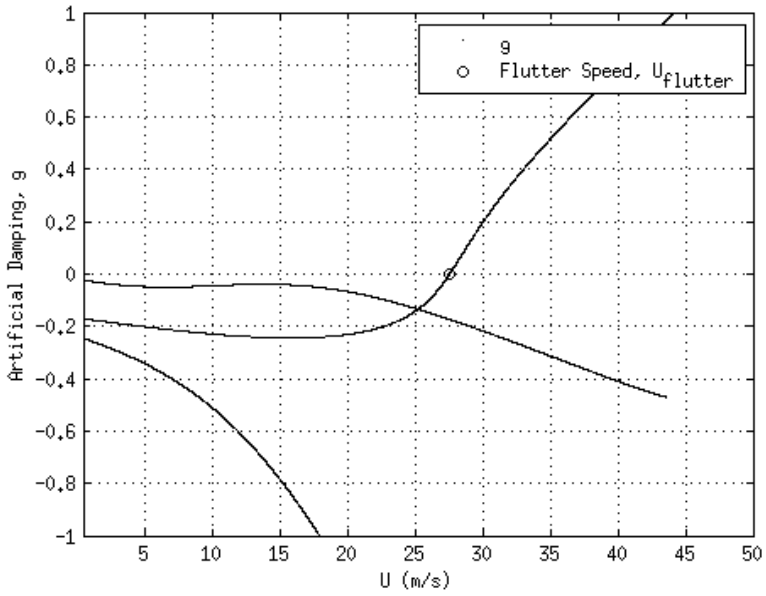

(a)

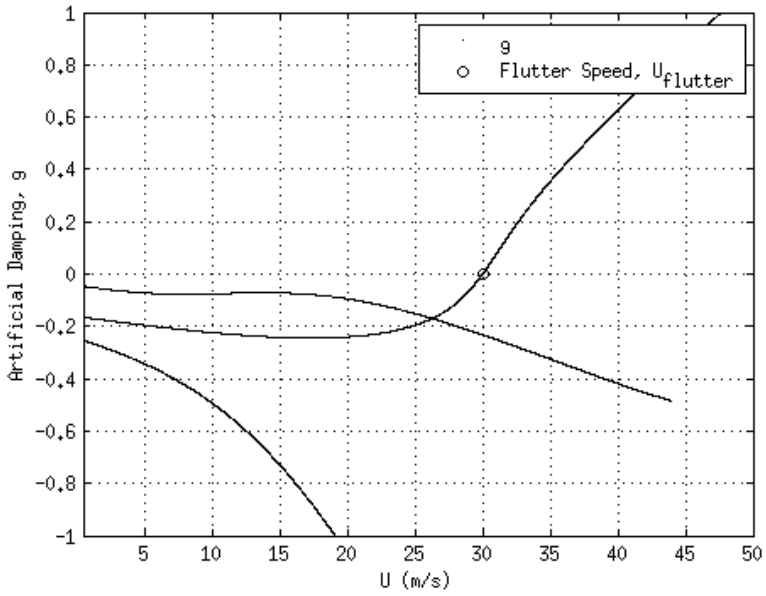

(b)

Figure 8.1: Linear Flutter Analysis of the UW systems. (a) Nominal Configuration (b) Modified Configuration

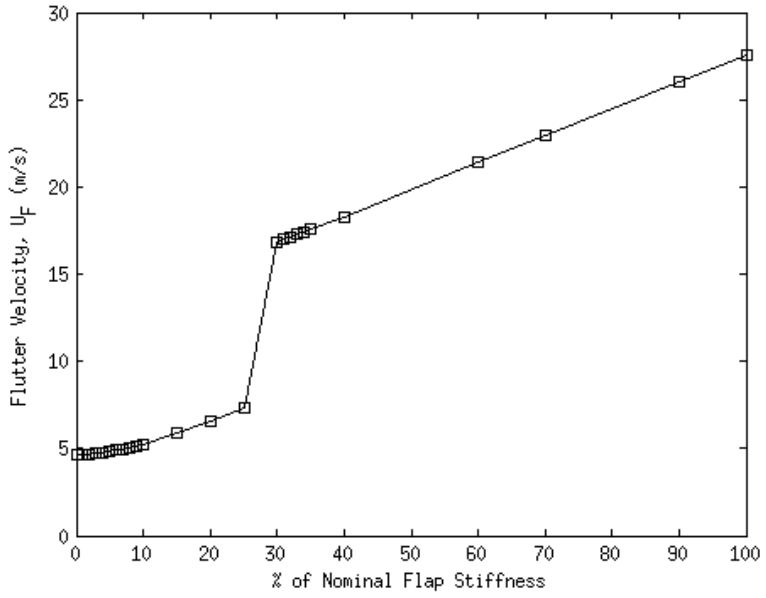

(a)

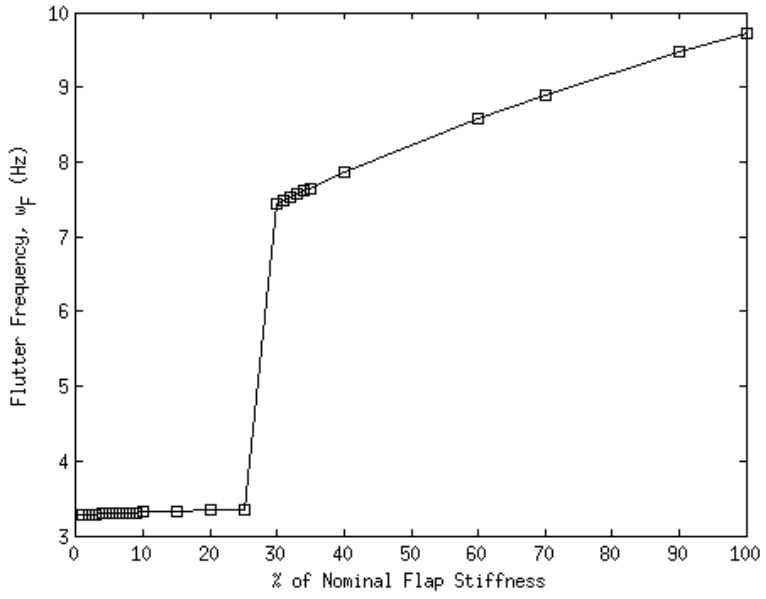

(b)

Figure 8.2: Effect of Flap Stiffness Variation on Linear Flutter Response of Nominal System (a) Flutter velocity vs flap stiffness (b) Flutter frequency vs flap stiffness

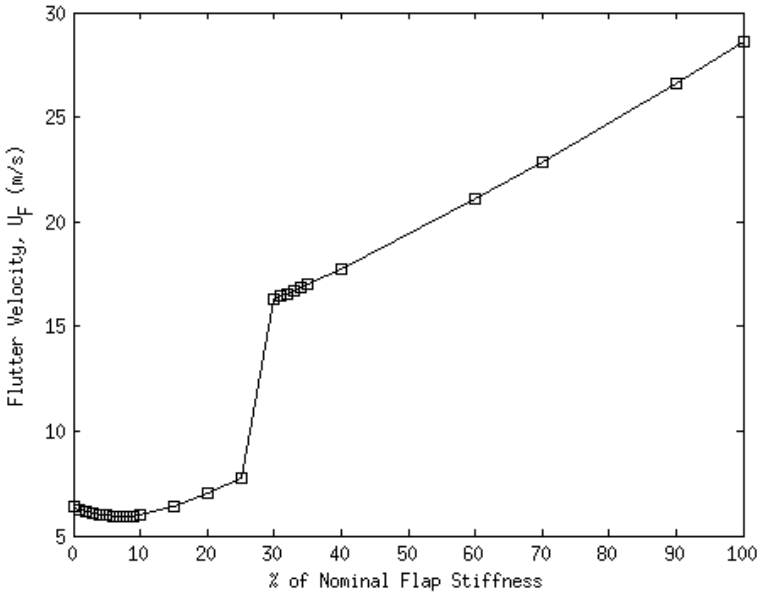

(a)

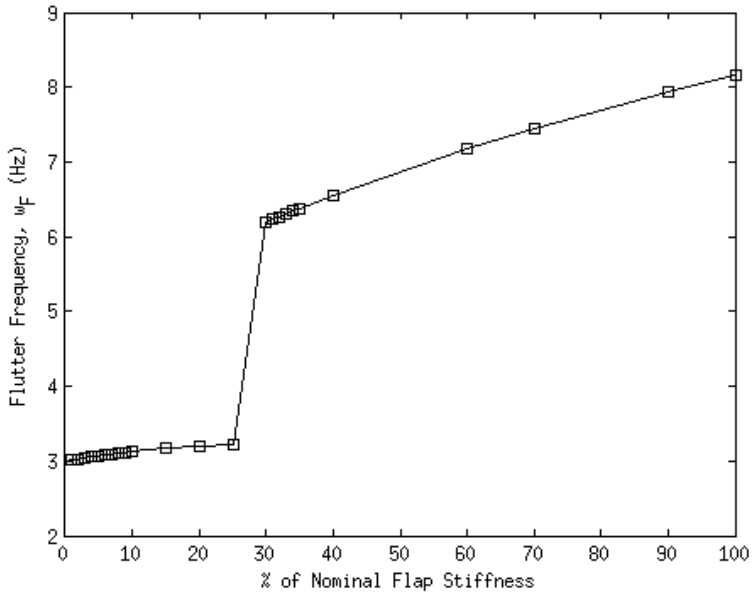

(b)

Figure 8.3: Effect of Flap Stiffness Variation on Linear Flutter Response of Modified System (a) Flutter velocity vs flap stiffness (b) Flutter frequency vs flap stiffness

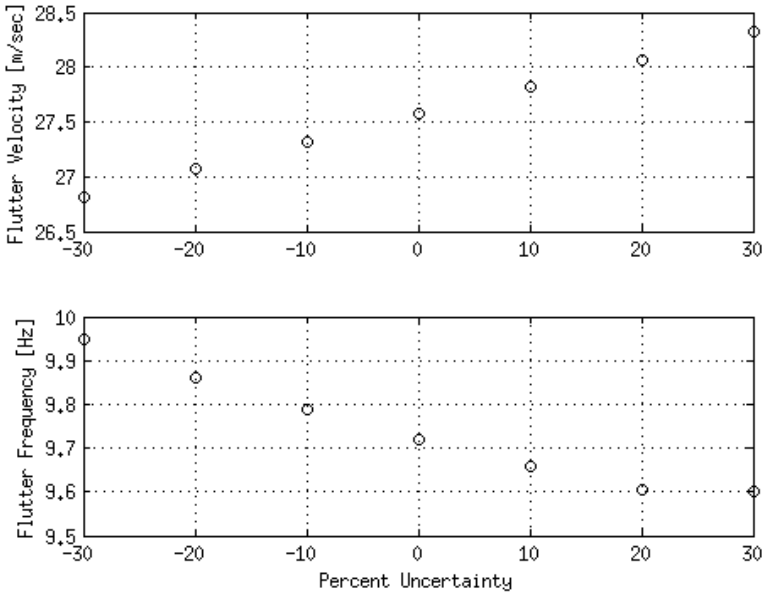

(a)

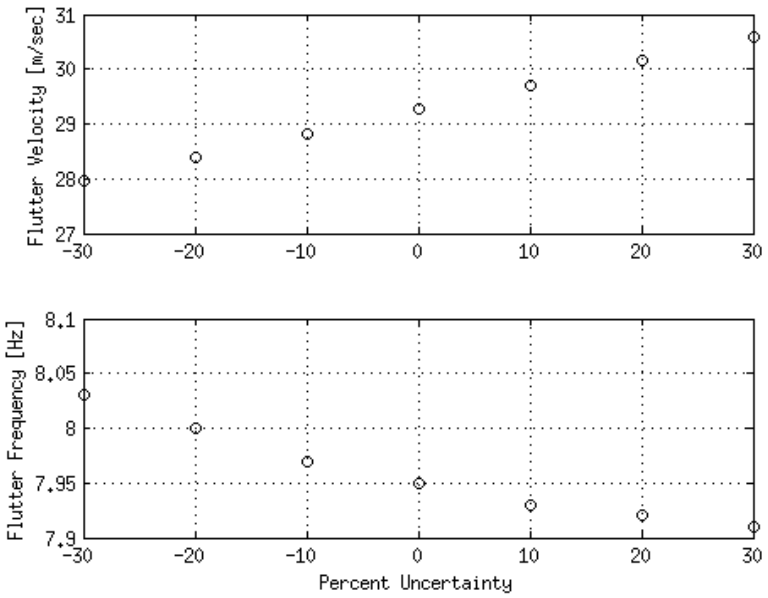

(b)

Figure 8.4: Effect of $g_s t$ Variation on Linear Flutter Response of Nominal System (a) Nominal System (b) Modified System

8.2 Freeplay Nonlinearity

For the freeplay nonlinearity, all simulations were run for a gap of total size 4.24° ($\delta = \pm 2.12°$). As mentioned earlier, *Conner et al*[4] showed that all responses scale in proportion to δ, so multiple freeplay gap sizes do not need to be analyzed. The results presented are based upon nonlinear numerical time simulations as described previously in Chapter 6 and additionally, in the flap degree of freedom, upon the describing function approach. The numerical responses are normalized by the angular gap size δ and the velocities are normalized by the zero-stiffness flutter speed $U_{F,0}^{nom}$ determined in the previous section.

Time domain responses were obtained using the parameters for the nominal system, given in Chapter 3, for simulated velocities $0 \leq U \leq U_F^{nom} = 27.57 \frac{m}{sec}$. Unsteady aerodynamics were transfered to the time-domain using the Roger approximation with four aerodynamic lag roots ($\overline{\beta} = 0.05, 0.35, 0.875, 1.7$). The time history responses were computed for two different initial conditions in order to study the effect of initial conditions on the system. The first initial condition, IC1, had a large plunge component and zero pitch and rudder contributions ($h(0) = 0.3$, $\alpha(0) = 0$, and $\beta(0) = 0$), while the second initial condition, IC2, had a reduced plunge component and again zero pitch and rudder contributions ($h(0) = 0.003$, $\alpha(0) = 0$, and $\beta(0) = 0$).

Figure 8.5 presents the describing function analysis of the rudder DOF motion along with a study into the effect of the variation of g_{st} on the rudder response to determine limit-cycle stability. In Figure 8.5(b), the transition from unstable to stable LCO can be seen. Below $\frac{\beta}{\delta} = 1.15$, an increase in structural damping has resulted in an increase in amplitude, while a decrease in structural damping has resulted in a decrease in amplitude corresponding to an unstable LCO, as discussed in Chapter 5, whereas above $\frac{\beta}{\delta} = 1.15$, the opposite is true, and the LCO is stable. Figure 8.5(c) presents an entirely unstable LCO.

Figure 8.6 presents results obtained for the response of the system using IC1 in the

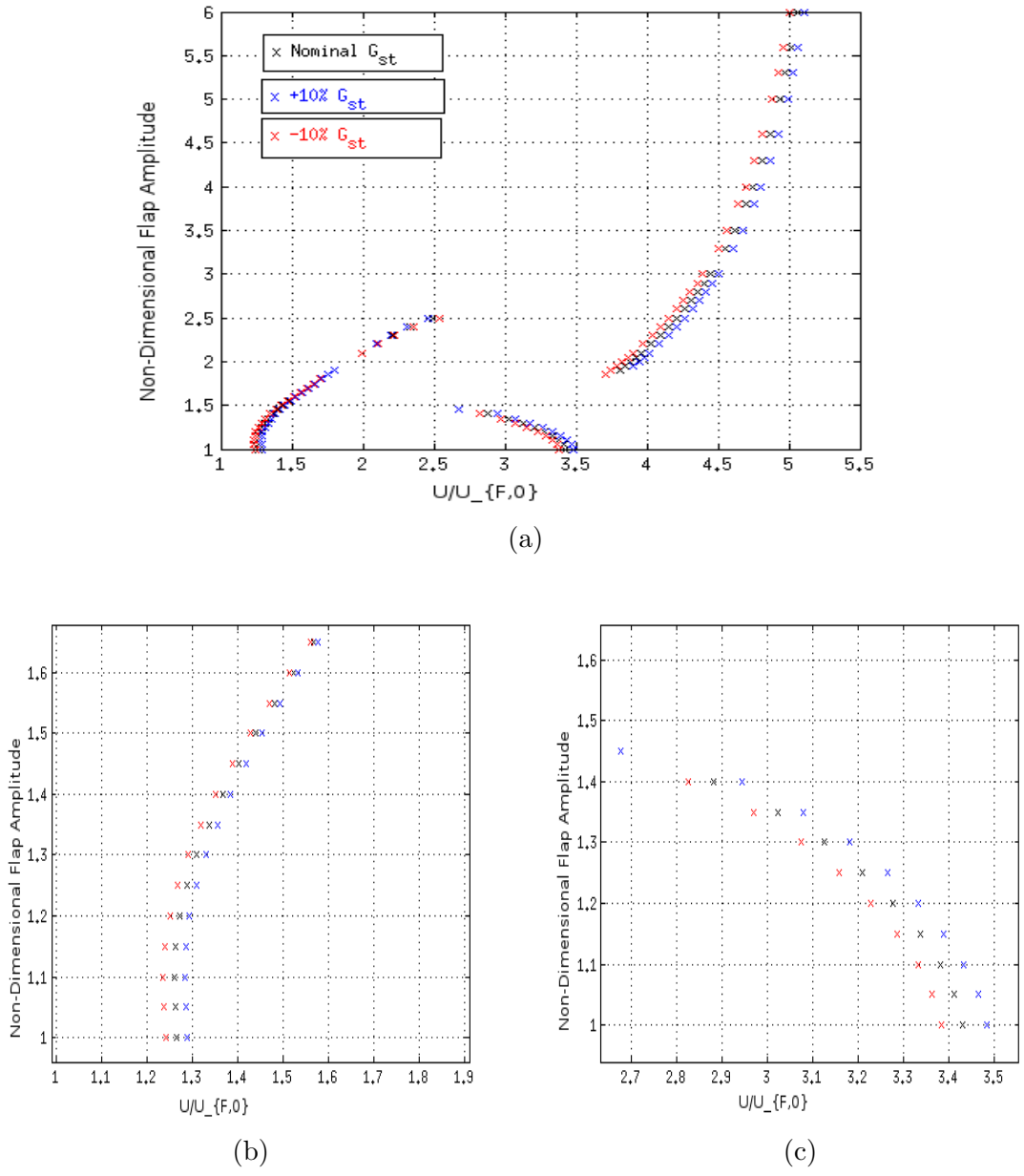

Figure 8.5: Describing Function Determination of Freeplay Limit Cycle Stability from variation of structural damping (black- nominal, red - 10% decrease, blue - 10% increase). (a) Overall Flap Response, (b) Transition from unstable to stable LCO at approx $\frac{\beta}{\delta} = 1.15$, (c) Unstable LCO

time domain and describing function results in the rudder degree of freedom. Figures 8.6(a), 8.6(b), and 8.6(c) present the nonlinear response amplitudes in each DOF, and Figure 8.6(d) presents the steady-state LCO frequency vs velocity. There are three regions of differing behavior in the system response below the flutter boundary. Below $U \approx U_{F,0}^{nom}$, the system is entirely stable; any initial disturbance decays to zero. At approximately $U = U_{F,0}^{nom}$, the response in each of the DOF jumps to a stable low-amplitude limit cycle with a low frequency around $3.5Hz$. The rudder response slowly increases in amplitude until about $U = 2.75U_{F,0}^{nom}$ at which point the amplitude gradually decreases until $3.5U_{F,0}^{nom}$ when it abruptly jumps to a lower amplitude, high frequency limit-cycle at $7Hz$. The plunge response also gradually increases in amplitude until $U = 3.0U_{F,0}^{nom}$, however the transition between limit-cycles is much more abrupt, as the high amplitude limit cycle becomes unstable and it quickly jumps to a stable low-amplitude, high-frequency limit cycle. The pitch response settles into a low-amplitude, low-frequency limit cycle around $U = U_{F,0}^{nom}$ where it remains until approximately $3.5U_{F,0}^{nom}$, when the low-frequency limit cycle becomes unstable and it jumps to a stable, slightly higher-amplitude, high-frequency limit-cycle.

At approximately $3.5U_{F,0}^{nom}$, each of the responses of the system move from the low-frequency limit cycle to the high-frequency limit cycle. This jump is characterized by discrete drops in the plunge and rudder amplitudes, but an increase in the pitch amplitude. Beyond $U = 3.5U_{F,0}^{nom}$, each of the response amplitudes quickly increase as the flutter boundary is approached.

Figure 8.7 shows examples of the numerical time histories in each DOF for the low- and high-frequency limit-cycles. The time series are presented for an arbitrary 1 sec sample that is taken after the system has reached steady state.

Figure 8.8 presents results obtained in the time-domain for the system subjected to IC2. Figures 8.8(a), 8.8(b), and 8.8(c) present the nonlinear response amplitudes in each DOF, and Figure 8.8(d) presents the LCO frequency vs velocity. The ampli-

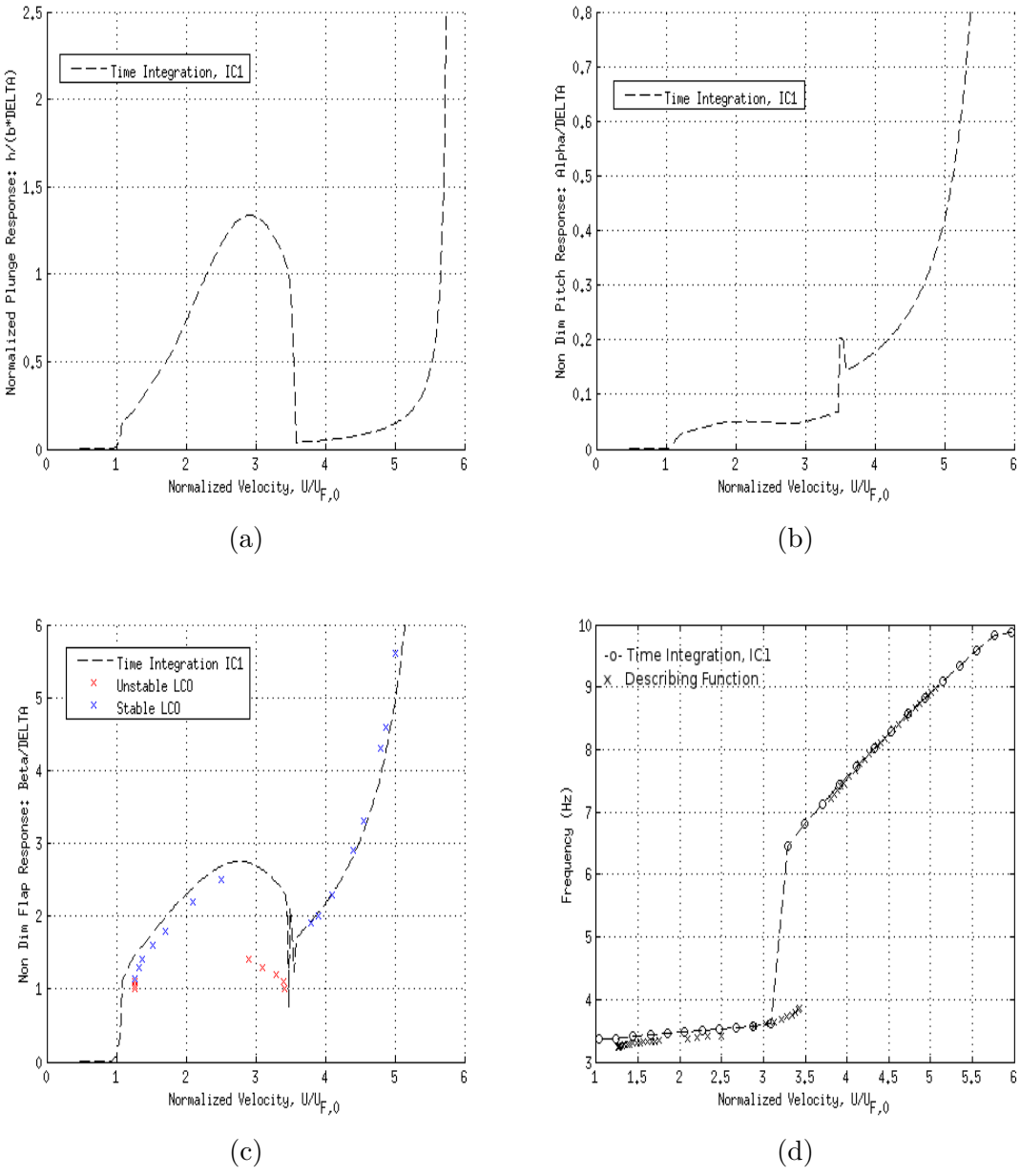

Figure 8.6: Normalized UW System Freeplay Amplitude Response for (a) plunge, (b) pitch, and (c) rudder with DF LCO; (d) Limit-Cycle Frequency vs Normalized Velocity obtained using IC1.

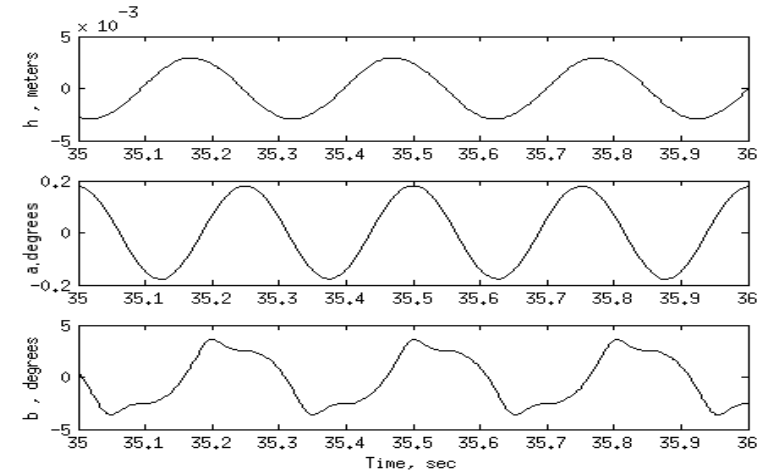

(a)

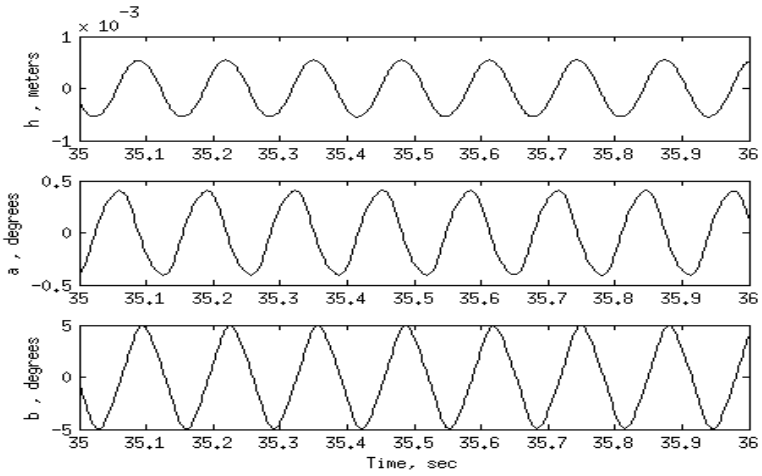

(b)

Figure 8.7: Numerical time-histories for the plunge, pitch, and rudder DOF. (a) Low-frequency LCO, $U = 1.44U_{F,0}^{nom}$, (b) High-frequency LCO, $U = 4.12U_{F,0}^{nom}$

tude responses of each DOF and the LCO frequency responses are the same as those presented in Figure 8.6 except between 15.5 and 17 $\frac{m}{sec}$. With the lower initial condition, the plunge and rudder responses drop into the lower amplitude, high-frequency LCO and the pitch jumps into the higher amplitude, high-frequency LCO at a lower velocity than with IC1. The nonlinear flutter speed is roughly 3% lower than the

linear flutter boundary of the nominal system, based on these simulations.

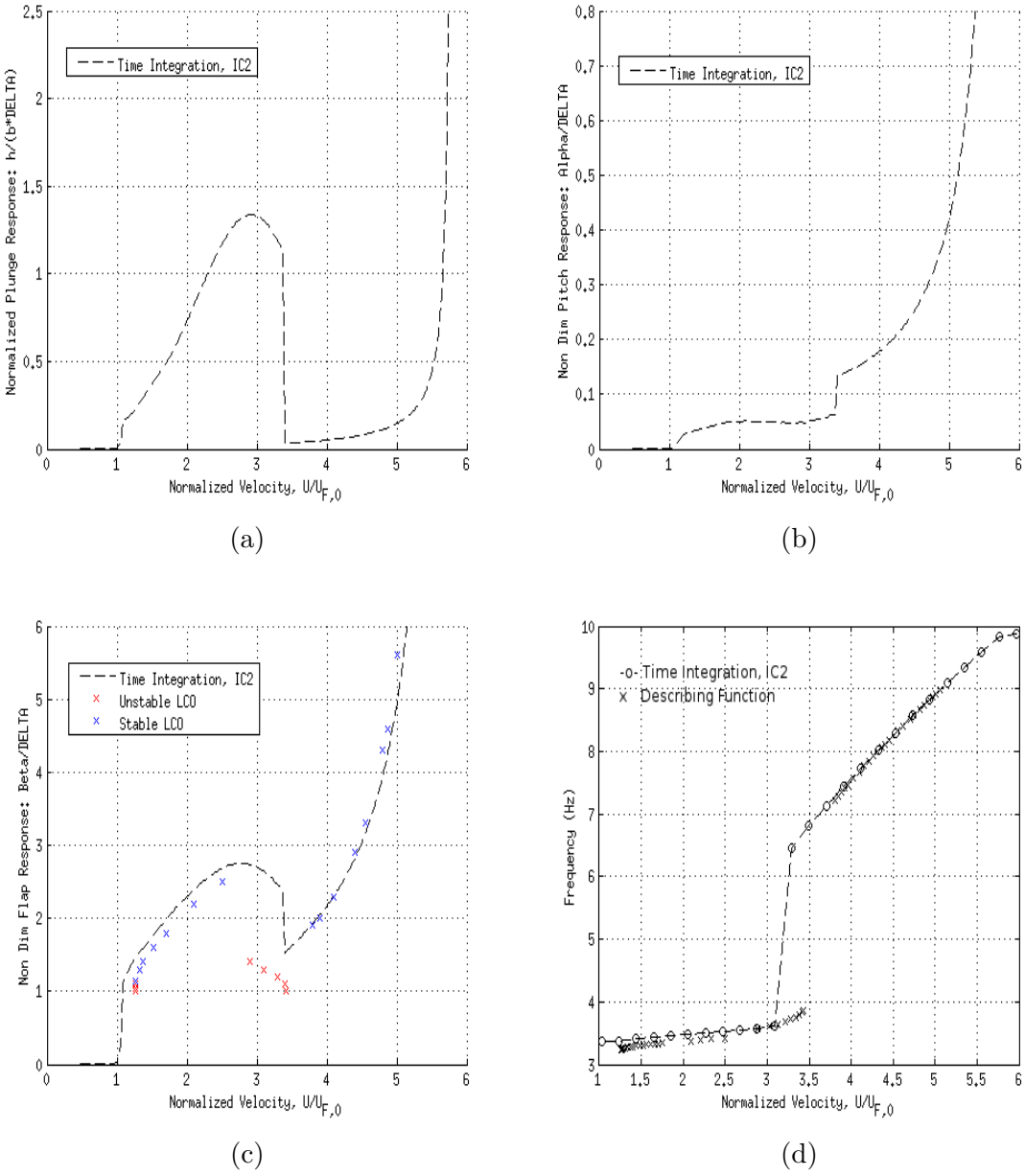

Figure 8.8: Normalized UW System Freeplay Amplitude Response for (a) plunge, (b) pitch, and (c) rudder with DF LCO; (d) Limit-Cycle Frequency vs Normalized Velocity obtained using IC2.

Note that Describing Function LCO results are presented here only for the rudder rotation amplitudes while amplitudes in all degrees of freedom (plunge, pitch, and rudder rotation) are presented that are based on time domain simulations. In studying nonlinear systems, time domain simulations would capture the behavior more accurately than describing function methods because of their capacity to capture motion at all frequencies (within what numerical time integration schemes would cover). Yet, because of the sensitivity to initial conditions used, time domain simulations may miss important limit cycles. The utilization of a describing function simulation, carried out in parallel to the time domain simulation, would increase confidence in the capability of the combined simulation effort to capture all LCOs. Studying just the rudder degree of freedom LCO behavior based on the describing function method is sufficient for that.

8.3 Quadratic Damping Nonlinearity

The effects of the quadratic damping nonlinearity were studied on the modified system for simulated velocities $0 \leq U \leq 28\frac{m}{sec}$ in the time domain. Unsteady aerodynamics were converted using the same Roger approximation and aerodynamic lag roots as presented in the previous section. The effect of initial conditions was again of interest so the system was analyzed at two initial conditions: IC1 was defined as $h(0) = 0.1$, $\alpha(0) = 0$, and $\beta(0) = 0$, and IC2 defined as $h(0) = 0.0001$, $\alpha(0) = 0$, and $\beta(0) = 0$; both with zero pitch and rudder components. Results of describing function analysis in the rudder degree of freedom are presented and compared to time-domain results.

Figure 8.9 shows the effects of variation in the structural damping model on the describing function analysis of the rudder response. This method of variation allows the stability of limit-cycles in the response to be determined. The system settles into a limit-cycle at $U = U_{F,0}^{mod}$ and amplitude increases until $U = 2.75U_{F,0}^{mod}$ where the limit-cycle becomes unstable and the response drops into a stable low-amplitude limit-cycle where it remains until flutter.

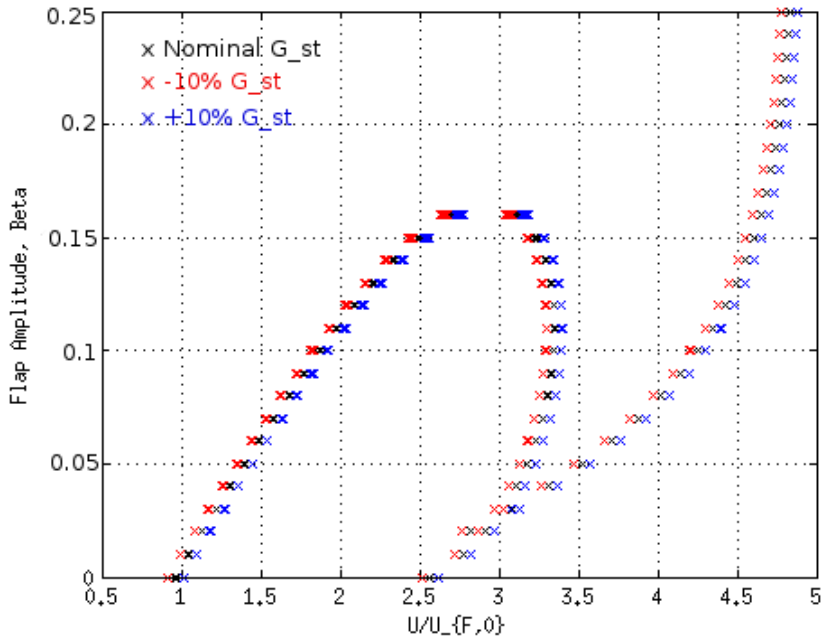

Figure 8.9: Describing Function Determination of Quadratic Damping Limit Cycle Stability from variation of structural damping (black- nominal, red - 10% decrease, blue - 10% increase).

Figure 8.10 presents results obtained for the response of the system subjected to IC1 in the time domain and describing function results in the rudder degree of freedom. Figures 8.10(a), 8.10(b), and 8.10(c) present the nonlinear response amplitudes in each DOF, and Figure 8.10(d) presents the LCO frequency vs velocity. Below $U \approx 0.8 * U_{F,0}^{mod}$, the system is entirely stable and any initial disturbance decays to zero. Beyond $U = U_{F,0}^{mod}$, the response in each of the DOF gradually increases in amplitude as the system enters a stable low-frequency limit-cycle around $3.5Hz$. The amplitude response of each DOF continually increase in amplitude until about $U = 3U_{F,0}^{mod}$ at which point the low-frequency limit-cycle loses stability and the system is attracted to a stable high-frequency limit-cycle around $5.5Hz$. The peak amplitude of the LCO, in the rudder DOF, near $U = 2.75U_{F,0}^{mod}$ differs slightly between the time domain

prediction and the describing function result. However, this difference is less than a tenth-of-a-degree and on the order of the RVDT sensor's sensitivity, so the two predictions are still in agreement.

As the system enters the high-frequency limit-cycle, the rudder rotation rate increases, therefore increasing the restoring force exerted by the quadratic dampers, which forces the amplitude response of each DOF to drop significantly as the system enters the high-frequency LCO. After dropping into the low-amplitude, high-frequency limit-cycle, the amplitudes quickly increase again as the flutter boundary is approached. The effect of the quadratic dampers decreases the flutter boundary by approximately 10% from the linear flutter speed, a much larger effect than the freeplay nonlinearity caused on the system.

Figure 8.11 presents results obtained in the time-domain for the system subjected to IC2. Figures 8.11(a), 8.11(b), and 8.11(c) present the nonlinear response amplitudes in each DOF, and Figure 8.11(d) presents the LCO frequency vs velocity. The amplitude responses of each DOF and the LCO frequency responses are the same as those presented in Figure 8.10 except that the low-frequency limit-cycle becomes unsteady at a lower flow speed, as was the case with the freeplay nonlinearity. With the lower plunge initial condition, all three responses drop into the lower amplitude, high-frequency LCO at a lower velocity than when subjected to IC1. It is interesting to note that both nonlinearities, freeplay and quadratic damping, do not display LCO behavior below approximately their respective $U_{F,0}$ values, suggesting the minimum velocity for LCO to occur in the presence of any nonlinearity is the zero-stiffness linear flutter velocity of that system.

Figure 8.12 shows examples of the numerical time histories in each DOF for the low- and high-frequency limit-cycles. Again, the time series are presented for an arbitrary 1 sec sample that is taken well after the system has reached steady state.

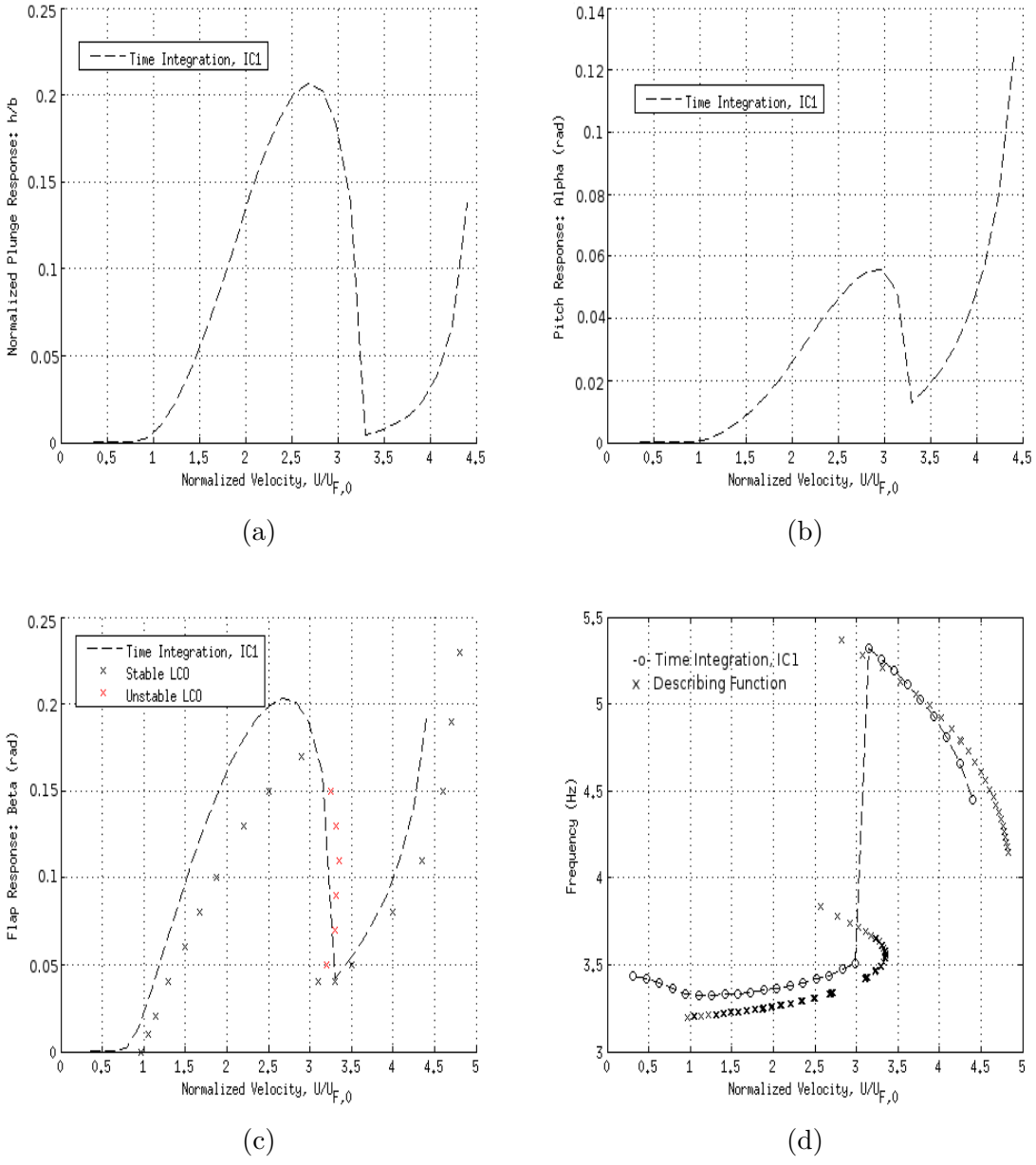

Figure 8.10: Normalized UW System Quadratic Damping Amplitude Response for (a) plunge, (b) pitch, and (c) rudder with DF LCO; (d) Limit-Cycle Frequency vs Normalized Velocity obtained using IC1.

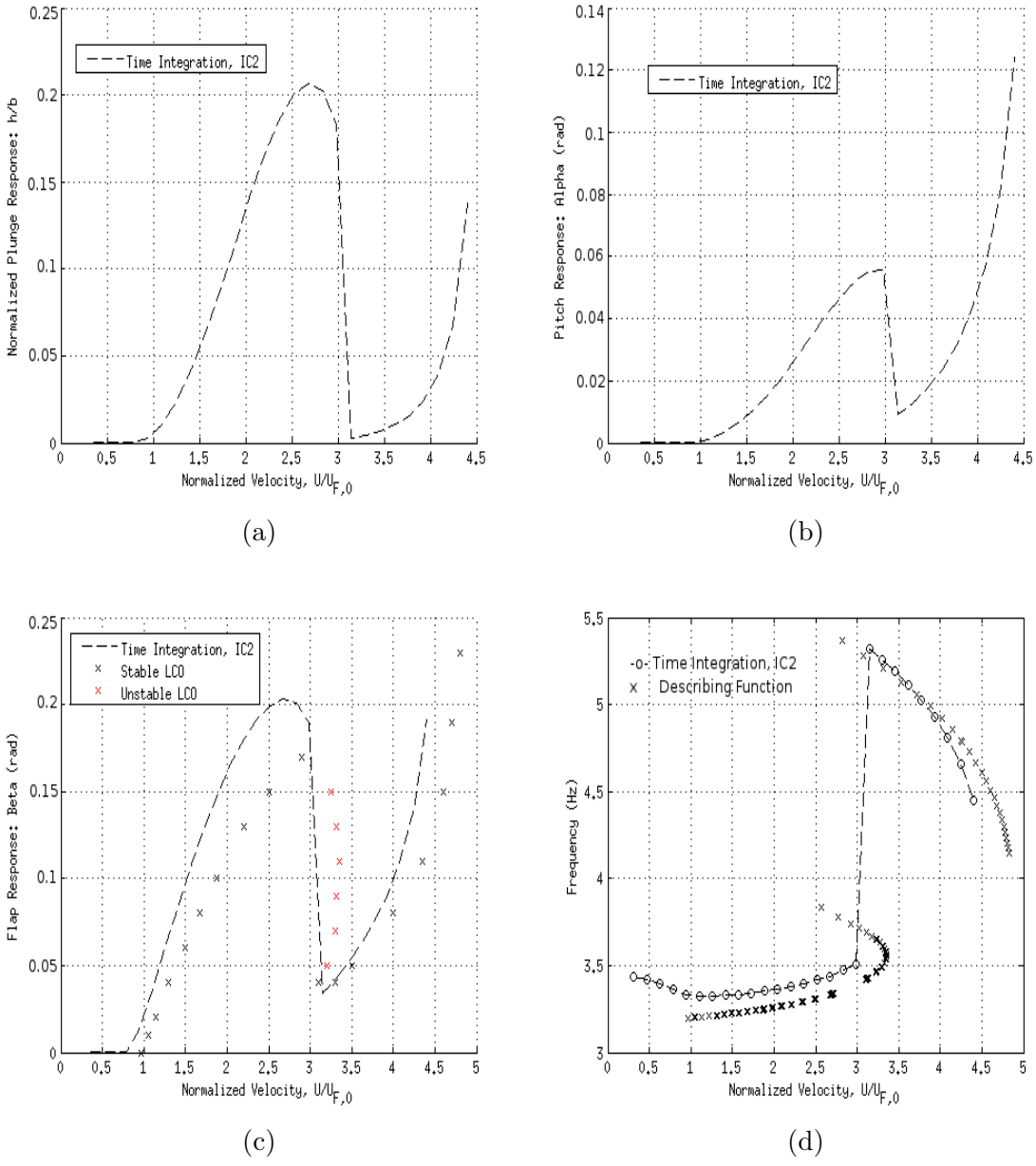

Figure 8.11: Normalized UW System Quadratic Damping Amplitude Response for (a) plunge, (b) pitch, and (c) rudder with DF LCO; (d) Limit-Cycle Frequency vs Normalized Velocity obtained using IC2.

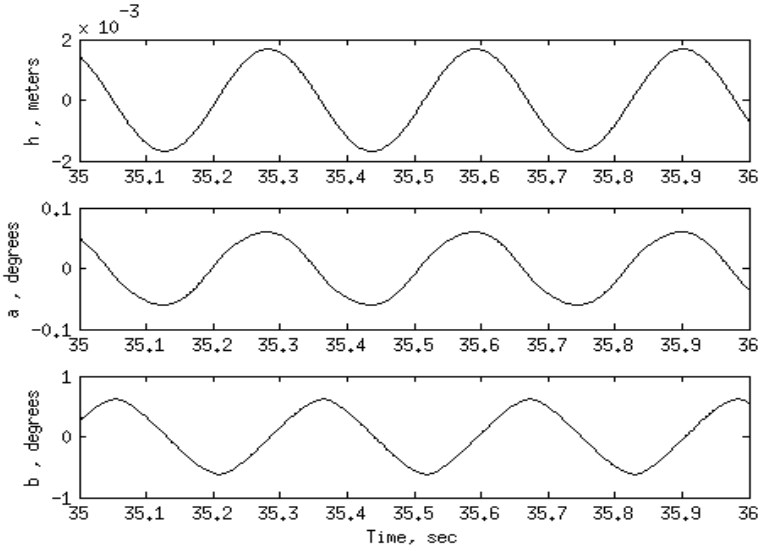

(a)

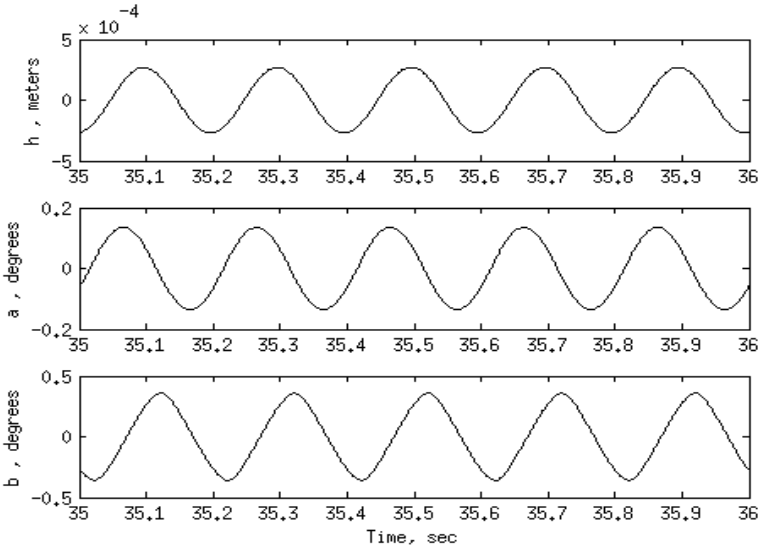

(b)

Figure 8.12: Numerical time-histories for the plunge, pitch, and rudder DOF. (a) Low-frequency LCO, $U = 1.57U_{F,0}^{mod}$, (b) High-frequency LCO, $U = 3.61U_{F,0}^{mod}$

Chapter 9
CONCLUSIONS

This thesis has presented the development and results of numerical analyses for linear and nonlinear stability of a typical 3 DOF aeroelastic tail/rudder section. An experimental model was developed and structurally characterized through ground testing for analysis. Prototype nonlinear dampers were designed, tested, and verified with the mathematical model in order to simulate a failed control surface actuator, acting in the damping mode only. The linear behavior of the system was numerically characterized in order to have an understanding of the basic flutter mechanisms and effects of structural damping on the system.

Results presented for nonlinear analysis sought to determine the effect of control surface nonlinearities on the aeroelastic behavior of the system. Nonlinear terms that were investigated included stiffness freeplay about the control surface hinge line and quadratic damping, representing a failed actuator. Although the nonlinearities investigated here act on the control surface, the development of the numerical models can allow nonlinearities in any DOF and the aeroelastic section can also be modified to include more DOF, such as a trim tab.

The limit-cycle response amplitudes and frequencies of the system were determined using direct integration of the equations of motion using Roger's approximation for unsteady aerodynamics and compared to steady-state frequency and rudder response predictions determined from the describing function technique. The describing function approach was able to predict both stable and unstable limit cycles, with stability being determined from variation in the structural damping model of the system. The system was shown to exhibit a variety of limit-cycle behavior below the linear flutter

boundary and the time-domain and describing function results predicted the same behavior. The nonlinear systems were determined to have a lower flutter threshold than the linear system which was expected of introducing nonlinearities into a complex aeroelastic system. It is the author's hope that the numerical modeling techniques developed in this thesis serve as valuable predictions in future wind tunnel testing of the experimental UW system and will be useful in furthering the understanding of nonlinear effects on aeroelastic systems.

9.1 Future Work

There are several improvements that could be made to the work presented here. As it stands, the models provide detailed predictions of the system's response, but there are ways to make the models more robust and expand the research into new areas. These suggestions include both numerical and experimental investigations and are presented below.

- Incorporate ability to predict plunge and pitch response amplitudes in the frequency domain into the code. As mentioned earlier this was not pursued in this study, although correlation between describing function and time domain results, for flap amplitudes and steady-state LCO frequency, indicates that it is safe to assume the describing function responses would be similar to those obtained in the time domain.

- Wind Tunnel Testing: The numerical predictions provided in this work should be used as a framework to develop an experimental test plan of the UW flutter model. Comparing experimental results to the numerical simulations presented in this thesis would fully validate the simulation capabilities and allow the code to be developed further to handle more complex analyses. Alternatively, test results may highlight missing effects in the simulations and would, then, lead to modeling improvements.

- Active Control: Now that a thorough understanding of the behavior of the system under different nonlinearities has been obtained, it is desirable to investigate the ability to suppress the pre-flutter limit-cycle oscillations through the use of active controls and reduce the effects of nonlinearities on the system.

- 3D Numerical Simulations: The numerical models should be expanded to analyze 3-D configurations and aerodynamics. This can support wind tunnel testing of large aeroelastic models in the University of Washington Kirsten Wind Tunnel for academic and industry research.

BIBLIOGRAPHY

[1] O.A. Bauchau and H. Liu. On the modelling of hydraulic components in rotorcraft systems. *Journal of the American Helicopter Society*, 51(2):175–184, April 2006.

[2] Raymond L. Bisplinghoff, Holt Ashley, and Robert L. Halfman. *Aeroelasticity*. Addison-Wesley Publishing Company, Inc., 1955.

[3] R.L. Clark, E.H. Dowell, and K.D. Frampton. Control of a three-degree-of-freedom airfoil with limit-cycle behavior. *Journal of Aircraft*, 37(3):533–536, May 2000.

[4] M.D. Conner, D.M. Tang, E.H. Dowell, and L.N. Virgin. Nonlinear behavior of a typical airfoil section with control surface freeplay: A numerical and experimental study. *Journal of Fluids and Structures*, 11(1):89–109, January 1997.

[5] M.D. Conner, L.N. Virgin, , and E.H. Dowell. Accurate numerical integration of state-space models for aeroelastic systems with free play. *AIAA Journal*, 34(10):2202–2205, October 1996.

[6] J.T. Gordon. Nonlinear damping effects on control surface flutter of a typical section airfoil. In *International Forum on Aeroelasticity and Structural Dynamics*, Seattle, WA, USA, June 2009.

[7] J.T. Gordon, E.E. Meyer, and R.L. Minogue. Nonlinear stability analysis of control surface flutter with freeplay effects. *Journal of Aircraft*, 45(6):1904–1916, December 2008.

[8] M. Henon. On the numerical computation of poincare maps. *Physica D: Nonlinear Phenomena*, 5(2-3):412–414, September 1982.

[9] C. Hou, D. Hsu, Y. Lee, H. Chen, and J. Lee. Shear-thinning effects in annular-orifice viscous fluid dampers. *Journal of the Chinese Institute of Engineers*, 30(2):275–287, 2007.

[10] L. Liu and E.H. Dowell. Harmonic balance approach for an airfoil with a freeplay control surface. *AIAA Journal*, 43(4):802–815, April 2005.

[11] F. Paltera, M. Tuttle, and E. Livne. Flutter response to damage of composite aircraft control surfaces. In *Procedings of the 2009 SEM Annual Conference*, Albuquerque, New Mexico USA, June 2009. SEM.

[12] F. Paltera, M. Tuttle, and E. Livne. Wind tunnel model development for aeroelastic tests of wing/control-surface systems with hinge stiffness loss and with a velocity-squared damper. In *FAA Joint Advanced Materials and Structures Center of Excellence, 2010 Technical Review Meeting*, Seattle, Washington USA, May 2010. AMTAS.

[13] F. Paltera, M.E. Tuttle, and W. Kuykendall. A composite airfoil section used to study aeroelastic effects. In *11th International Congress and Exhibition on Experimental and Applied Mechanics 2008*, Orlando, Florida USA, June 2008. SEM.

[14] Francesca Paltera. Flutter response to damage of composite aircraft control surfaces. Master's thesis, University of Washington, 2008.

[15] K.L. Roger. Airplane math modelling methods for active control design. In *Structural aspects of active controls, Agard Conference Proceedings*, pages 4.1 – 4.11, April 1977.

[16] Robert H. Scanlan and Robert Rosenbaum. *Introduction to the Study of Aircraft Vibration and Flutter*. The Macmillan Company, 1951.

[17] Steven H. Strogatz. *Nonlinear Dynamics and Chaos*. Perseus Books Publishing, LLC., 1994.

[18] D. Tang, E.H. Dowell, and L.N. Virgin. Limit cycle behavior of an airfoil with a control surface. *Journal of Fluids and Structures*, 12(7):839–858, October 1998.

[19] James H. Taylor. *Electrical Engineering Encyclopedia, Describing Functions*, pages 77–98. John Wiley & Sons, Inc., 2001.

[20] T. Theodorsen. General theory of aerodynamic instability and the mechanism of flutter. *NACA Report No. 496*, 1935.

[21] T. Theodorsen and I.E. Garrick. Flutter calculations in three degrees of freedom. *NACA Report No. 741*, 1942.

[22] S.T. Trickey, L.N. Virgin, and E.H. Dowell. The stability of limit-cycle oscillations in a nonlinear aeroelastic system. *Proceedings of the Royal Society of London A: Mathematical, Physical, and Engineering Sciences*, 458(2025), 2002.

[23] T.J. Viersma. *Analysis, Synthesis, and Design of Hydraulic Servosystems and Pipelines*. Elsevier Publishing Company, 1980.

[24] J.S. Vipperman, R.L. Clark, M.D. Conner, and E.H. Dowell. Experimental active control of a typical section using a trailing-edge flap. *Journal of Aircraft*, 35(2):224–229, March 1998.

[25] D.D. Šiljak. *Nonlinear Systems*. John Wiley & Sons, Inc., 1969.

Appendix A

NOMENCLATURE

Variables:

a	Non-dimensional distance from airfoil mid-chord to elastic axis, w.r.t the semi-chord
b	Semi-chord
c	Non-dimensional distance from airfoil mid-chord to control surface (rudder) hinge line, w.r.t the semi-chord
$c_{h,\alpha,\beta}$	Plunge, pitch, and rudder viscous damping coefficients
$\mathbf{C}$	Viscous Damping Matrix
$C(k)$	Theodorsen circulation function
g	Structural damping coefficient
$\mathbf{G_{st}}$	Structural Damping Matrix
h	Plunge displacement
I_α, I_β	Moments of inertia of tail-rudder about a and of rudder about c
k	Reduced frequency, $\frac{\omega b}{U}$
K_α, K_β	Torsional stiffness of tail about a and of rudder about c
K_h	Stiffness of tail in deflection
$K_{\beta,eq}$	Equivalent Rudder Stiffness as determined by Describing Function for freeplay case
L	Aerodynamic lift
M_α, H_β	Aerodynamic moment of tail-rudder and of rudder
M	Total mass of tail-rudder and support blocks
P	Negative of Aerodynamic Lift ($P = -L$)

$\mathbf{P_i}$	Roger Approximation Matrices
Q_{q_i}	Generalized Forces of Lagrangian Dynamics
S_α, S_β	Static moments of tail-rudder about a and of rudder about c
T_i	i^{th} Theodorsen constant (see Appendix B)
U	Velocity
x_α	Center of gravity of the tail/rudder from a, normalized by b
x_β	Center of gravity of rudder from c, normalized by b

Greek Symbols:

α	Pitch angle about the elastic axis
β	Rudder (flap) angle about the hinge line
β_n	Aerodynamic Lag Roots (Roger Approximation)
δ	Angular size of the freeplay region
η	Ratio of Orifice to Piston Areas ($\frac{A_o}{A_p}$)
λ	Eigenvalue
ρ	Density of air
ζ	Damping ratio
ω	Frequency ($\frac{rad}{sec}$)

Appendix B

THEODORSEN'S CONSTANTS

The Theodorsen constants as functions of non-dimensional hinge location, c, and non-dimensional elastic axis location, a.[20]

$$T_1 = -\frac{1}{3}\sqrt{1-c^2}(2+c^2) + c\cos^{-1}c$$

$$T_2 = c(1-c^2) - \sqrt{1-c^2}(1+c^2)\cos^{-1}c + c(\cos^{-1}c)^2$$

$$T_3 = -(\frac{1}{8}+c^2)(\cos^{-1}c)^2 + \frac{1}{4}c\sqrt{1-c^2}\cos^{-1}c(7+2c^2) - \frac{1}{8}(1-c^2)(5c^2+4)$$

$$T_4 = -\cos^{-1}c + c\sqrt{1-c^2}$$

$$T_5 = -(1-c^2) - (\cos^{-1}c)^2 + 2c\sqrt{1-c^2}\cos^{-1}c$$

$$T_6 = T_2$$

$$T_7 = -(\frac{1}{8}+c^2)\cos^{-1}c + \frac{1}{8}c\sqrt{1-c^2}(7+2c^2)$$

$$T_8 = -\frac{1}{3}\sqrt{1-c^2}(2c^2+1) + c\cos^{-1}c$$

$$T_9 = \frac{1}{2}\left[\frac{1}{3}(\sqrt{1-c^2})^3 + aT_4\right]$$

$$T_{10} = \sqrt{1-c^2} + \cos^{-1}c$$

$$T_{11} = \cos^{-1}c(1-2c) + \sqrt{1-c^2}(2-c)$$

$$T_{12} = \sqrt{1-c^2}(2+c) - \cos^{-1}c(2c+1)$$

$$T_{13} = \frac{1}{2}[-T_7 - (c-a)T_1]$$

$$T_{14} = \frac{1}{16} + \frac{1}{2}ac$$